LAND SURFACE NET RADIATION MODELLING

ISADORA REZENDE DE OLIVEIRA SILVA
February, 2019

SUPERVISORS:
Dr. Ir. C. van der Tol
Ir. G.N. Parodi
Dr. H. Pelgrum (external supervisor)

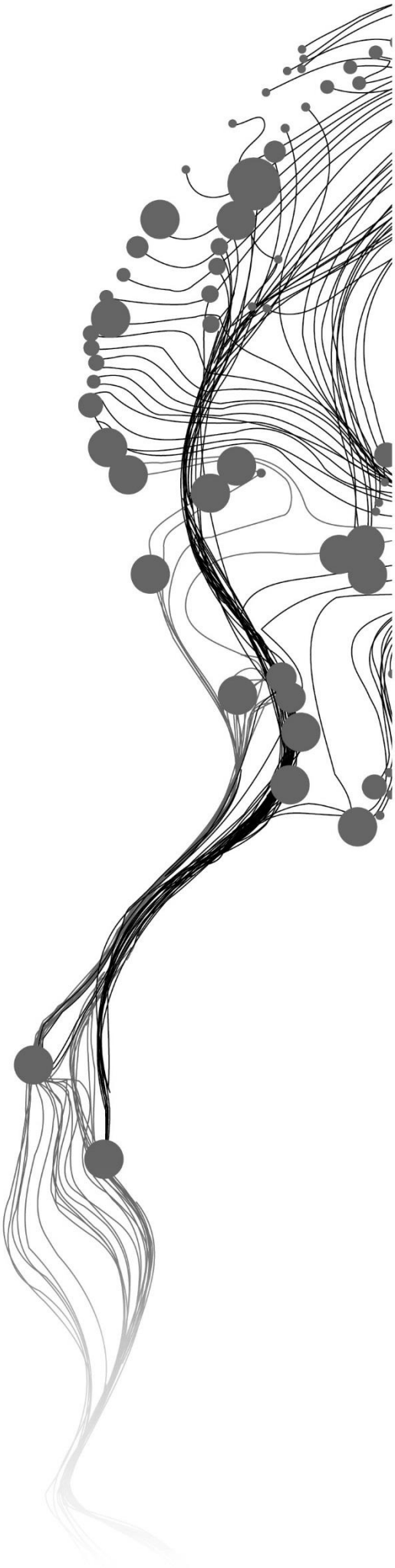

LAND SURFACE NET RADIATION MODELLING

ISADORA REZENDE DE OLIVEIRA SILVA

Enschede, The Netherlands, February 2019

Thesis submitted to the Faculty of Geo-Information Science and Earth Observation of the University of Twente in partial fulfilment of the requirements for the degree of Master of Science in Geo-information Science and Earth Observation.
Specialization: Water Resources and Environmental Management

SUPERVISORS:
Dr. Ir. C. van der Tol
Ir. G. N. Parodi
Dr. H. Pelgrum (External Supervisor)

THESIS ASSESSMENT BOARD:
Dr. Z. Su (Chair)
Dr. S. Pareeth (External Examiner, IHE Delft Institute for Water Education)

ABSTRACT

Land surface net radiation (R_n) constitutes the energy to be partitioned between soil, sensible and latent heat fluxes, influencing crop growth and evapotranspiration. Existing ground measurements are too sparse for mapping R_n globally, and none of the alternative estimates is valid globally under all-sky conditions in the spatiotemporal resolution necessary for routine agricultural applications. In this study, ground data from 10 stations of a high-quality network were used to validate 2 models for albedo, 2 for upwelling longwave ($R_{L\uparrow}$), 9 for clear sky solar fluxes ($R_{S\downarrow clear}$), and 12 methods for incoming longwave radiation ($R_{L\downarrow}$). The performance of these 25 parameterised or remote-sensing approaches was analysed in terms of spatiotemporal characteristics, inaccuracies of the input data and environmental conditions. The upwelling elements showed a strong dependency on the spatial aspects, being worse for a satellite-based model with coarse resolution (1°x1°). The root mean square error (RMSE) between predicted and measured daily $R_{S\downarrow clear}$ estimate by the best method was approximately 11.0W/m², and the leading cause of error was high aerosol loads. The RMSE was slightly larger for all-sky $R_{L\downarrow}$ (17.0W/m²) using locally measured meteorological data. The change in the input source from ground variables to modelled generally decreased the performance of the $R_{L\downarrow}$ methods.

ACKNOWLEDGEMENTS

To Marcos and Catarina, who gave me all the support I could ever ask for.

To Bernardo, for saying exactly what I needed to hear.

To Ema and Paolo, for being my family in Europe.

To Pramod, for trying to keep me calm in this journey.

To Christiaan and Gabriel, for the knowledge and advice.

To Henk, for the opportunity to work in this topic and all the instructions.

To Arno, for the support along the whole masters.

To Rita and Jean-Michel, for making me interested in remote sensing.

To Marie-Chantal and Theresa, for all the hard work.

To my friends in ITC: **we did it**!

TABLE OF CONTENTS

LIST OF FIGURES

LIST OF TABLES

LIST OF ACRONYMS AND SYMBOLS

AB12	Abramowitz et al. (2012) longwave downwelling model
α	Ångström's exponent [-]
β	Ångström's turbidity coefficient [-]
Ba	Ratio of the forward-scattered irradiance to the total scattered irradiance due to aerosols
BH81	Clear sky shortwave downwelling model by Bird and Hulstrom (1981)
BON	Station Bondville
BT75	Brutsaert (1975) longwave downwelling model
CAB	Station Cabauw
CD99	Crawford and Duchon (1999) longwave downwelling model
CERES	Clouds and the Earth's Radiant Energy System
c_f	Cloud fraction [-]
c_k	Unclearness index [-]
c_{mf}	Cloud modification factor [-]
DB98	Dilley and O'Brien (1998) longwave downwelling model
DF14	Clear sky shortwave downwelling model by Dai and Fang (2014)
DK00	Diak et al. (2000) longwave downwelling model
DRA	Station Desert Rock
ε	Squared inverse relative distance between the Sun and the Earth [-]
e_0	Vapour pressure [hPa]
E13	Station South Great Plains
EI00	Rigollier et al. (2000) model with Ineichen (2008a) Linke turbidity factor formulation
ER00	Rigollier et al. (2000) model with Remund et al. (2003) Linke turbidity factor formulation
ESRA	European Solar Radiation Atlas
FAO	Food and Agriculture Organization of the United Nations
FPK	Station Fort Peck
GEOS	Goddard Earth Observing System
GOB	Station Gobabeb
GOES	Geostationary Operational Environmental Satellites
GWN	Station Goodwin Creek
h_0	Solar elevation angle [º]
I_0	Solar constant [W/m²]
IN08	Clear sky shortwave downwelling model by Ineichen (2008b)
IQ83	Clear sky shortwave downwelling model by Iqbal (1983)
KB82	Kimball et al. (1982) longwave downwelling model
LW	Longwave
m	Air mass [-]
MAC87	Modified MAC clear sky shortwave downwelling model by Davies et al. (1975)
MK73	Modified Maykut and Church (1973) longwave downwelling model
MODIS	Moderate Resolution Imaging Spectroradiometer
MSG	Meteosat Second Generation
p_g	Surface pressure [hPa]
p_{sl}	Sea level pressure [hPa]
PT96	Prata (1996) longwave downwelling model
PSU	Station Rock Springs
RES08	REST2 Clear sky shortwave downwelling model by Gueymard (2008)

ρ_g	Surface broadband shortwave albedo [-]
$R_{L\uparrow}$	Surface longwave upwelling radiation [W/m²]
$R_{L\downarrow}$	Surface longwave downwelling radiation [W/m²]
R_n	Surface net radiation [W/m²]
ρ_s	Sky albedo [-]
$R_{S\downarrow DIF}$	Surface shortwave downwelling diffuse radiation [W/m²]
$R_{S\downarrow DIR}$	Surface shortwave downwelling direct radiation [W/m²]
$R_{S\downarrow TOA}$	Solar radiation reaching the top of the atmosphere [W/m²]
$R_{S\uparrow}$	Surface upwelling shortwave radiation [W/m²]
$R_{S\downarrow}$	Surface shortwave downwelling radiation [W/m²]
SXF	Station Sioux Falls
SW	Shortwave
T_a	Screen-level air temperature [K]
TBL	Station Boulder
T_c	Cloud base temperature [K]
τ_c	Cloud visible optical depth [-]
T_G	Global shortwave broadband transmissivity [-]
T_g	Surface temperature [K]
τ_λ	Aerosol optical depth in the wavelength λ [-]
T_{LK2}	Linke turbidity coefficient at air mass 2 [-]
TOA	Top of atmosphere
w	Total column atmospheric water vapour [cm]
w_{ci}	Cloud ice water path [g/m²]
w_{cw}	Cloud liquid water path [g/m²]
ZC07	Zhou et al. (2007) longwave downwelling model
ϵ_{clear}	Clear sky atmospheric emissivity [-]
ϵ_{cloud}	Cloud emissivity [-]
ϵ_g	Surface emissivity [-]
σ	Stefan-Boltzmann constant

1. INTRODUCTION

1.1. Background

The amount of radiative energy available in a surface is represented by its net radiation (R_n), the driving force for many physical and biological mechanisms. On a global range, the heterogeneous distribution of R_n powers atmospheric and oceanic circulations (Suttles & Ohring, 1986). On a longer timescale, the increase in greenhouse gases causes substantial changes in the net radiation budget, affecting the Earth's climate. As global warming drives us away from fossil fuels, photovoltaic systems are becoming more popular, and their design is dictated by the characteristics of incoming fluxes. On a land surface, R_n constitutes the energy to be partitioned between soil, sensible, and latent heat fluxes, influencing snowmelt (Sicart et al., 2004), crop growth (Diak, Bland, Mecikalski, & Anderson, 2000; Hunt, Kuchar, & Swanton, 1998) and evapotranspiration (Allen, Masahiro, & Trezza, 2007; Bastiaanssen et al., 1998; Su, 2002).

Commonly used to model evapotranspiration via remote sensing, energy balance approaches are particularly sensitive to the net radiation (Zheng, Wang, & Li, 2016). In a scenario of global population growth, climate change and water scarcity, assessing R_n in detailed temporal and spatial scales is mandatory to increase agricultural water use efficiency.

Net radiation represents the balance between incoming and outgoing shortwave (SW) and longwave (LW) fluxes at the surface. It is s a function of: (i) Latitude, day and time, which dictates the amount of solar radiation reaching the top of atmosphere (TOA); (ii) Atmospheric conditions, i.e. presence of clouds and aerosols, temperature and water vapour profiles, which influence the incoming SW and LW components; and (iii) Surface properties, i.e. albedo (ρ_g), emissivity (ϵ_g) and temperature (T_g).

The incoming fluxes are highly influenced by the presence and properties of clouds. In the tropics, clouds can decrease the noontime solar radiation that reaches the surface from about 1000 W/m² to 100 W/m² (Suttles & Ohring, 1986). They have the opposite effect on the incoming longwave component since water vapour is a dominant emitter of longwave radiation (Shunlin Liang, Zhang, He, Cheng, & Wang, 2013). Furthermore, R_n on cloudy conditions is highly variable due to the clouds' great spatiotemporal heterogeneity (Kalisch & MacKe, 2012).

Net radiation can be measured in situ or modelled. Traditional ground observations are accurate if the instruments are well calibrated, but their spatial representation and distribution are limited, making it unsuitable for most applications (Jia, Jiang, Liang, Zhang, & Ma, 2016). Furthermore, while incoming solar radiation is commonly measured by meteorological stations, incoming longwave ($R_{L\downarrow}$) is not routinely monitored given the costs of purchasing and calibrating the instruments (Li, Jiang, & Coimbra, 2017).

In the past decades, many models have been developed to derive one of the net radiation fluxes. They can be generally grouped into three categories: (i) Physically based methods, which yield precise results using extensive radiative transfer calculations and detailed atmospheric profiles information; (ii) Parameterized methods, which calculate the fluxes employing easily available parameters based on locally fitted empirical relationships or radiative transfer theory; (iii) Hybrid methods; they combine one of the previous two approaches with the TOA irradiance measured by satellites, which act as a constraint. Due to the computation efficiency and the availability of the inputs, research has been focused in the parameterised and, more recently, in hybrid methods.

Recently, Liang et al. (2013) carried out an extensive review of the alternatives to estimate net radiation components. The authors mainly analysed ground networks and satellite-derived products. The later ones have an obvious problem with cloud coverage and are always subject to uncertainties regarding inversion procedures. As in ground measurements, there are more products for SW fluxes than for LW ones. Further on, the spatiotemporal resolutions and coverages of these estimates vary widely. According to the authors, all methods reviewed have their strengths and weakness, so it is nearly impossible to choose the best one.

Parameterised methods are also conditioned to some limitations. The main ones are the validity of locally fitted coefficients and the uncertainties of the input dataset. Calibrated parameters can be extrapolated over time and space, but only to places with similar environmental conditions (Choi, Jacobs, & Kustas, 2008; Gubler, Gruber, & Purves, 2012; Zhu, Yao, Yang, Xu, & Wang, 2017). If they differ, a high-quality time series of at least five year of data is necessary to generate stable coefficients (Kjaersgaard, Plauborg, & Hansen, 2007), which is particularly hard for longwave fluxes due to the limited number of ground stations. Even for locally fitted algorithms, the uncertainties of the dataset alone can degrade the accuracy of the modelled fluxes (Gubler et al., 2012; Ruiz-Arias & Gueymard, 2018; Yu, Xin, Liu, Zhang, & Li, 2018)

1.2. Problem Statement

Widespread in remote sensing-based evapotranspiration algorithms, energy balance methods are particularly sensitive to net radiation. Existing ground measurements are too sparse for mapping R_n globally especially when it comes to the longwave radiation, which is monitored in fewer locations. None of the alternative estimates, hybrid and parameterised methods, are valid globally for all sky conditions in the spatiotemporal resolution necessary for agricultural applications.

1.3. Objectives

The objective of this research is to identify the most suitable accurate hourly and daily, easy to apply models of land surface net radiation valid between 60°S and 60°N for all sky conditions from readily available data.

1.4. Specific Objectives

The specific objectives of the research are:

- To review existing methods to estimate net radiation and its components under clear, cloudy and all-sky (mixed) conditions;
- To determine the most suitable set of algorithms with global validity to estimate hourly and daily net radiation under all sky conditions for routine, near real-time data provision with limited computational effort.

1.5. Research Questions

Based on the specific objectives, the research questions are:

- What are the scopes, the strengths and weaknesses of existing methods regarding the estimation of R_n?
- What are the effects of the different spatial and temporal characteristics of the ground measurements and satellite-based data when validating the methods?
- What is the consequence of changing the source of inputs (e.g. air temperature from ground stations or retrieved from remote sensing) in the accuracy of the models?
- What are the contributions of specific site conditions (e.g. temperature, elevation, landcover) to the errors in R_n?
- How well can a limited number of ground stations represent the whole globe?

1.6. Thesis Structure

The thesis is outlined in nine chapters. Chapter 1 briefly introduces the subject, defines the problem and objectives and formulates the research questions. Chapter 2 expands the subject by giving more detail on the physical background, on the current methods to estimate net radiation components and the common issues faced. Chapter 3 generally describes the methodology steps taken. Chapter 4 justifies the selection of certain parameterisations or existing products to model R_n components. In Chapter 5, the datasets and their pre-processing are explained. Chapter 6 presents the description of the selected parametrisations. In Chapter 7, the modelled R_n fluxes are validated. Chapter 8 discusses the results in terms of the research questions. Chapter 9 presents the conclusions and recommendations from this research. References and appendices are presented at the end of the document.

2. BACKGROUND

The first section of this chapter gives the physical background of the radiation fluxes, which are important to understand the complexity of each component and its variation in space and time. Section 2.2 discusses the different methods to estimate the fluxes as well as common problems of the algorithms and review studies.

2.1. Physical Background

All-wave surface net radiation (R_n) is the sum of incoming and outgoing shortwave (0.3 to 4 μm) and longwave (4 to 100 μm) fluxes, which can be expressed by:

$$R_n = R_{S\downarrow}\left(1 - \rho_g\right) + R_{L\downarrow} - R_{L\uparrow} \quad (1)$$

where $R_{S\downarrow}$ is the incoming shortwave radiation, ρ_g, the surface shortwave broadband albedo, $R_{L\downarrow}$ and $R_{L\uparrow}$ the downward and the upward longwave fluxes, respectively.

$R_{S\downarrow}$ (2) is the solar radiation reaching the top of the atmosphere modified by scattering and absorption of different atmospheric components, expressed by T_G the global shortwave broadband transmissivity.

$$R_{S\downarrow} = R_{S\downarrow TOA} T_G \quad (2)$$

The solar radiation reaching the top of the atmosphere ($R_{S\downarrow TOA}$) can be written as:

$$R_{S\downarrow TOA} = I_0 \varepsilon \sin h_0 \quad (3)$$

where I_0 is the solar constant, ε the squared inverse relative distance between the Sun and the Earth and h_0 the solar elevation angle. The solar constant I_0 (≈1367 W/m²) is defined as the amount of solar radiation received at TOA on a surface normal to the incident radiation per unit area and per unit time at the mean Earth-sun distance. ε ranges from 0.967 to 1.033 and accounts for the variations between the Sun and the Earth due to the elliptical orbit. The solar elevation angle projects the extra-terrestrial radiation on the surface considering latitude, time of the day, the day of the year and sometimes the aspect and elevation of the surface.

The transmissivity T_G accounts for attenuation effects due to atmospheric components: ozone water vapour absorption and mixed gases (O_2, NO_2, CO_2) absorption; Rayleigh scattering; aerosol extinction; cloud droplets and ice crystals scattering and absorption. T_G can be written as:

$$T_G = \frac{1}{I_0} \int_0^\infty I_{0,\lambda} \left(\exp\left(-\frac{\tau_\lambda}{\sin h_0} \right) + T_{dif,\lambda} \right) d\lambda \quad (4)$$

where $I_{0,\lambda}$ is the extra-terrestrial incident radiation per wavelength λ, τ_λ is the monochromatic optical thickness and $T_{dif,\lambda}$, the diffuse transmissivity for λ. The first term in the wavelength integral (4) corresponds to the contribution by the direct solar beam, and the second one, the diffuse solar radiation. τ_λ can be computed by adding the individual inputs of each atmospheric element. The estimation of $T_{dif,\lambda}$ on the other hand, is more complicated since it should account for all scattering processes, including surface albedo via re-reflection. Because of this, the calculation of $R_{S\downarrow}$ is often divided between direct beam ($R_{S\downarrow DIR}$) and diffusive sky ($R_{S\downarrow DIF}$) radiations. From equations (3) and (4), it can be noted the solar elevation angle has a major effect on the flux at the surface, dictating the amount of radiation reaching TOA and the transmissivity of the direct beam.

The surface shortwave broadband albedo (ρ_g) is defined as the ratio between the reflected radiation and the incident radiation $R_{S\downarrow}$. The element $R_{S\downarrow}(1-\rho_g)$ in equation (1) corresponds to the shortwave energy absorbed by the surface. The albedo varies spatially and temporally according to soil moisture, vegetation growth, changes in snow cover and solar illumination, as well as human activities that impact the land cover, e.g. deforestation, urbanisation and agricultural practices (Shunlin Liang et al., 2013). Albedo can be assumed constant during a short period of time (Jiang et al., 2015). ρ_g values can range from below 0.1 for some regions in the ocean up to 0.9 for fresh deep snow (Dobos, 2006), for land surfaces, its average is roughly 0.24 (S. Liang, 2018).

The incoming longwave ($R_{L\downarrow}$) is the dominant incoming wave component during the night. It is the result of scattering, absorption and emission of the different atmospheric components above the surface. The principal and most variable emitter of LW radiation in the atmosphere is water vapour. Carbon dioxide is the second, while O_3, CH_4, N_2O and aerosols are minor ones. In drier places, the contribution of these components to the longwave radiation becomes more relevant. $R_{L\downarrow}$ can be expressed as:

$$R_{L\downarrow} = -\int_0^{\infty}\int_{p_g}^{0} \pi\, B_\lambda(T(p)\frac{dT_\lambda(p_g,p)}{dp}dp\, d\lambda \tag{5}$$

where B_λ is the monochromatic Planck function evaluate for the temperature T at pressure p, T_λ is the monochromatic transmissivity function evaluated from the pressure p until the surface, whose pressure is p_g. The surface $R_{L\downarrow}$ comes then from the entire atmospheric column (5). However, the main share comes from the lower atmosphere: the bottom 500m accounts for 80% of the radiation and the lower 10m, about 35% (J. Schmetz, 1989). Therefore, for clear sky conditions, the downwelling longwave flux ($R_{L\downarrow clear}$) is commonly expressed in the Stefan-Boltzmann law (6), where ϵ_{clear} is the clear sky atmospheric emissivity, σ is the Stefan-Boltzmann constant, T_a, the screen-level air temperature (≈2m above the surface).

$$R_{L\downarrow clear} = \epsilon_{clear}\sigma {T_a}^4 \tag{6}$$

The upwelling longwave ($R_{L\uparrow}$) is the main cause of surface cooling at night. It consists of two components: the surface LW emission and the reflected $R_{L\downarrow}$, expressed respectively by the first and second term in equation (7). In this formula, ϵ_g is the surface emissivity and T_g the surface temperature. For densely vegetated and humid areas, the ϵ_g is almost equal to one (S. Liang, 2018); for bare soils and rocks, the value depends on the composition, typically ranging between 0.8 and 1.0 (Gillespie, 2014).

$$R_{L\uparrow} = \epsilon_g\sigma {T_g}^4 + R_{L\downarrow}(1-\epsilon_g) \tag{7}$$

Clouds have opposite effects on the incoming shortwave and longwave radiations, decreasing and increasing the fluxes, respectively. In the SW range, they reflect in the visible and absorb in the near infrared. They reduce the intake by water vapour below them so that the total absorption by the atmosphere is not changed radically by clouds (J. Schmetz, 1989). In the LW range, they enhance $R_{L\downarrow}$ by filling the atmospheric window region (8 – 13 μm). Their relative contribution decreases in locations with higher humidity. In this range, the most important parameters that determine the cloud contribution are cloud cover, amount of ice and water, cloud base height and temperature (J. Schmetz, 1989).

According to a study of the global radiative fluxes between 2000 and 2010 performed by Stephens et al. (2012) nearly 30% of the solar radiation entering the Earth system is reflected back to space, and clouds are responsible for about 64% of that total. The remaining 70%, is either absorbed by the atmosphere (22%) or by the surface (48%). In the LW range, clouds account for 7.5% of the radiation that reaches the ground; the surface emits 15% more longwave radiation than it receives. The Earth surface net radiation is about 115 Wm^{-2}.

These numbers represent the average R_n on a global scale for ten years; however, it varies tremendously in space and time. For example, $R_{S\downarrow}$ changes during the day, seasons and has even presented significant fluctuations on decadal timescales due to clouds and atmospheric pollution (Shunlin Liang et al., 2013). The land surface albedo changes greatly for different spatial scales due to distinct land covers. Moreover, there is a lot of concern regarding the emissions of anthropogenic greenhouse gases, which increase the LW emission towards the surface.

2.2. Methodology Background

A vast number of algorithms have been developed in the last decades to derive one of the elements of the surface radiative budget. They can be grouped into three categories:

i. Physically-based methods (Dedieu, Deschamps, & Kerr, 1987; Duguay, 1995; Fu, Liou, Cribb, Charlock, & Grossman, 1997), which require detailed atmospheric information (i.e. vertical profiles of water vapour and temperature, information about ozone, trace gases, aerosols, cloud properties) as an input for radiative transfer calculations. These methods yield accurate results, but they are computationally extensive, and the detailed atmospheric dataset is rarely available from field measurements and often inaccurate when derived from satellite products;
ii. Parameterized methods (Bird & Hulstrom, 1981a; Brunt, 1932; Brutsaert, 1975; Choudhury, 1982; Crawford & Duchon, 1999; Dilley & O'Brien, 1998; Gueymard, 2008; Idso, 1981; Idso & Jackson, 1969; Ineichen, 2008a; Iqbal, 1983; Prata, 1996; Swinbank, 1963; Yaping Zhou & Cess, 2001; Yaping Zhou, Kratz, Wilber, Gupta, & Cess, 2007), which calculate the radiation fluxes from easily available atmospheric and surface features (e.g. near-surface air temperature, land surface temperature) based on empirical relationships or on the radiative transfer theory. These methods are easy to operate, but they were created for certain conditions and may not be suitable for different ones; and
iii. Hybrid remote sensing methods, which can be further divided into two groups:
    a. "Look-up table" methods, as classified by (Shunlin Liang et al., 2013), usually begin by simulating the TOA radiances and the surface radiative fluxes using radiative transfer models for a vast number of representative atmospheric profiles (Cheng, Liang, Wang, & Guo, 2017; Kim & Liang, 2010; Wang & Liang, 2009; Yingji Zhou et al., 2018). Empirical relationships are then built based on machine learning or statistical analysis. These methods don't rely on any atmospheric parameters, but relationships must be built for each sensor.
    b. Another type of hybrid method is the one from Clouds and the Earth's Radiant Energy System (CERES) and the International Satellite Cloud Climatology Project (ISCCP). In this approach, the radiative fluxes are estimated by physically-based methods or by simpler parametrisations using atmospheric and surface properties retrieved from remote sensing or reanalysis datasets. The radiative fluxes at TOA act as a constraint to those methods.

Due to their ease computation and implicit physic basis, research has been focused on the parameterised methods which are based on radiative transfer theory and, on the past few years, on hybrid methods.

Remote sensing R_n products are more numerous for shortwave measurements than for longwave ones (Shunlin Liang et al., 2013). There is a clear coupling between the SW radiation remotely measured at TOA and the surface fluxes. At this wavelength, atmospheric constituents absorb and scatter but do not emit SW radiation. On the other end, the relationship between TOA radiances and LW components is not so evident and quantifying them requires further information on the atmosphere (J. Schmetz, 1989).

The presence of clouds complicates remote observations of the land surface. In the visible and infrared (including thermal) ranges, clouds obscure remote observations of the land surface, decoupling the radiative fluxes measured from remote sensing (RS) to the surface ones. Further on, optical RS can only provide info

regarding the cloud-top when some of the most sensitive parameters are actually located at their bottom (J. Schmetz, 1989). Thus, the main challenge to generate R_n via hybrid methods relies on thermal components and cloudy conditions (Jiang et al., 2016).

The spatiotemporal resolutions and coverages of remote sensing estimates vary widely, which imposes an additional limitation of these type of R_n model for agricultural applications. A common problem to all RS estimates is the scale issue of the ground measurements, which are used for calibration/validation, and the satellite pixel size. Geostationary satellites can provide detailed temporal information, but their pixel size is too coarse. Polar-orbiting sensors can give the spatial resolution and coverage needed for a global analysis. However, they consist of snapshots of R_n in time and generally require interpolation to daily values. In a study by Zheng et al. (2016), the instantaneous estimates of evapotranspiration were better than the daily ones calculated by temporal upscaling. These authors state there is an urgent need to improve the temporal upscaling methods for all RS algorithms and products.

According to Ruiz-Arias and Gueymard (2018), model-vs-measurement review studies can be quite useful for ranking methods, but they have some shortcomings:

i. The number of ground stations used for validation is quite limited. They are located mainly in developed countries in a few climate zones, which makes it harder to generalise them globally;
ii. The input data comes from many different sources, with different spatiotemporal resolutions and different degrees of interpolation. A severe degradation in the performance of the model can happen exclusively because of the dataset;
iii. The definition of clear sky may vary. The cloud-screening process is uncertain, and there is no standard method. This difference may link comparisons under partly cloudy conditions to clear sky methods or the other way around, limiting the meaning of the results.

To overcome the first two limitations, the authors compared $R_{S\downarrow}$ models with each other using a synthetic input database built from atmospheric reanalysis. This approach allowed them to identify the conditions where the models disagreed the most which should be targeted in further researches. Even though their study was limited to parameterised clear sky shortwave downwelling model, these issues are equally relevant for modelling other net radiation components under all sky conditions.

Shunlin Liang et al. (2013) mention the accuracies of the ground measurements vary inter and even intra-networks. The problems related to calibration of longwave radiometers limits, even more, the number of stations that accurately measure these fluxes. This aggravates issue (i), constraining the validity of the parameterised $R_{L\downarrow}$ methods, which are largely dependent on the environmental conditions they were developed for (Choi et al., 2008). As such, Zhu et al. (2017) recognise calibrated parameters can be easily extrapolated in time, but not in space; Gubler et al. (2012) indicate that local calibration or the choice of a method fitted in similar climatic zone are key steps for modelling $R_{L\downarrow}$. Making matters worse, Kjaersgaard et al. (2007) remark that, to obtain stable local coefficients, at least 5 years of data are necessary.

Relating (ii) with (iii), it can be expected that the accuracy of the cloud corrections methods depends on the cloud representation in the models. All the parametrised algorithms to derive $R_{L\downarrow}$ for cloudy conditions reviewed by Yu et al. (2018) require further improvement. These authors compared the performance of 8 cloud correction algorithms for longwave components using synthetic, ground-based and satellite/reanalysis datasets and concluded the uncertainties in the cloud parameters are the leading source of error in the estimate of $R_{L\downarrow}$. Gubler et al. (2012) acknowledge a mistake of around one-tenth in the cloud transmissivity results in differences up to 15% in the modelled $R_{L\downarrow}$.

To investigate the effects of the issue of point (iii), Marthews, Malhi, and Iwata (2012) checked the performance of 18 $R_{L\downarrow clear}$ parametrisations combined with 6 cloud corrections for one station in the Amazon forest (Brazil). They found out some clear sky methods performed worse for strictly clear sky conditions than cloudy sky models, while some schemes represented $R_{L\downarrow}$ better than the cloud corrections even when the sky conditions were not clear. These authors compiled a table of 7 indicators that describe "lack of clearness in the atmosphere". Amongst them are:

- cloud fraction or cloud coverage (c_f), the portion of the visible sky that is obscured by clouds. It is traditionally estimated by ground observers, but it can also be done by satellite;
- unclearness index (c_k), which is defined by 1 minus the ratio between the measured $R_{S\downarrow}$ and the $R_{S\downarrow TOA}$.

Another common indicator was introduced by Crawford and Duchon (1999):

- cloud modification factor (c_{mf}), defined as 1 minus the ratio of the measured $R_{S\downarrow}$ and the estimated $R_{S\downarrow clear}$.

All these indicators have their strengths and limitations. As discussed by Ruiz-Arias and Gueymard (2018) there is no standard to define c_f for ground observations; furthermore, the difference between the "visible sky" and the satellite pixel will lead to different clear sky definitions. c_k accounts not only for the clouds but also for all the other components which reduce the $R_{S\downarrow}$. c_{mf} has the advantage of accounting for the clouds' radiative forcing (Alados, Foyo-Moreno, & Alados-Arboledas, 2012). Indeed, in their comparison of four all-sky $R_{L\downarrow}$ models, Li et al. (2017) noted the using c_{mf} instead of c_f reduced the errors in all methods. However, c_{mf} requires estimates of the clear shortwave flux, which might introduce more uncertainties in the models, especially at low sun angles (Flerchinger, Xaio, Marks, Sauer, & Yu, 2009). Both c_k and c_{mf} need local measurements of $R_{S\downarrow}$, which are not always available. Besides, these indicators only work for daytime, limiting the evaluation of longwave estimates during the night, as in the studies by Carmona, Rivas, and Caselles (2014) and Choi et al. (2008). The night-time $R_{L\downarrow}$ contribution cannot be neglected in a daily analysis; for this reason, temporal extra- or interpolation is needed. Cloud correction methods that employ c_{mf} as inputs can use different intervals for this: Zhu et al. (2017) used linear interpolation between the last three hours before sunset and the first three hours after sunrise; Gubler et al. (2012) studied different interpolation possibilities and concluded four hours functioned better.

Because of the cloud's high temporal variation and the time-steps used by the parameterised methods, e.g. 1 minute or 1 day, an additional complication on point (iii) is the time period that is used for the cloud cover estimation. Analysing cloud correction methods that relied on c_{mf}, Flerchinger et al. (2009) noticed high errors occurred when the clouds shading the pyranometer did not represent the average conditions of the surrounding environment (partially cloudy conditions). To suppress this issue, the authors used diverse time windows to estimate c_{mf} and concluded it was better to compute 30-min $R_{L\downarrow}$ considering the mean solar radiation of a 4-hour period rather than the instantaneous $R_{S\downarrow}$ measurement. On the other hand, for daily averages, the authors noticed they needed 30-min or hourly estimates of $R_{L\downarrow}$ to capture the diurnal variation. The time window for daily averaging in $R_{S\downarrow}$ methods also imposes a challenge since many models discard measurements for low sun elevation angles (Ruiz-Arias & Gueymard, 2018). This is reasonable for the direct components but not for the diffuse ones.

Summing up, there are many approaches to monitor R_n components on a global scale. The number of ground stations is too small for a worldwide analysis and to validate methods in different climatic conditions. Hybrid satellite methods have problems related to longwave fluxes, cloud coverage and spatiotemporal resolution. Parameterised methods are subject to a series of complications: spatial extrapolation of locally calibrated parameters, uncertainties in the input dataset, definitions of clear and cloudy conditions, cloud representation and of time windows for the analysis.

3. METHODOLOGY

The methodology is represented in the flowchart in Figure 3-1. The first part of this thesis consisted of selecting models for estimating R_n Selection of Methods(Chapter 4). The result at this stage was a set of existing R_n products, algorithms and their required inputs. The input dataset was thus defined based on method selection and is presented in Chapter 5. The approaches were then described (Chapter 6) and applied to the pre-processed inputs. To determine the best set of models, a comparison between predicted and expected fluxes was performed (Chapter 7).

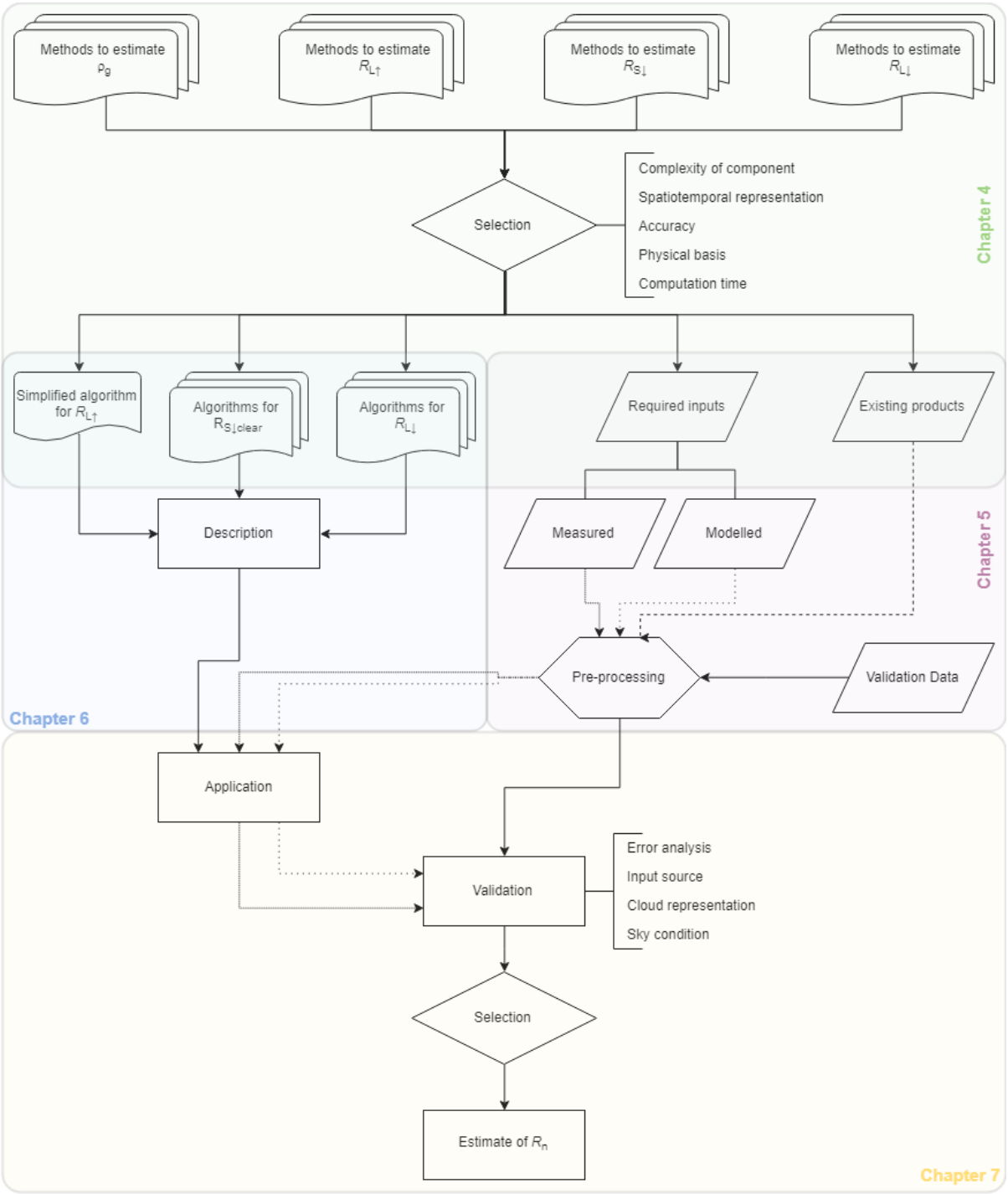

Figure 3-1 – Methodology steps flowchart

Given the number of algorithms to estimate net radiation or one of its components and the limited time for this thesis, a pre-selection was carried out to identify the most promising ones. The starting criteria were the complexity of the radiation components and their variation in space and time. Thus, more methods were analysed for longwave downwelling components than for shortwave upwelling ones.

Then, research papers were used to assess the performance of satellite-based products and parameterised models. The first ones were selected based on their accuracy, spatiotemporal resolution and coverage. Since this study aims at identifying models that can be globally used and the ground stations are not enough to allow worldwide calibration, the parametrisations were selected based on their performance using the original coefficients. Further criteria for these algorithms include: the frequency of use as indicated by the number of citations of the paper, the availability of required inputs and equations, the computation time and the physical basis

The dataset was determined based on the selected models. The inputs, validation data and existing products were detailed in terms of their units, instruments or conceptual algorithms. An extrapolatory data analysis was carried out to summarise the main characteristics and check for inconsistencies. Required assumptions, interpolations or other adjustments were also detailed.

The original publications of the chosen parameterisations were used to describe the models in terms of their conceptualisation, assumptions made and conditions they were developed for, which largely dictates the models' limitations. In this stage, it was also verified whether the publications included all the equations that were necessary to reproduce the method.

The algorithms were tested for the typical conditions of the dataset to check for inconsistencies. Some models were slightly adapted when the outputs were unreasonable, e.g. produced negative transmissivities. All the required adjustments are detailed.

The parametrisations were then applied to the pre-processed inputs, and their results were compared to the validation data via visual inspection and statistical indicators. Root mean square error (RMSE – Eq. (8), Mean Bias Error (MBE – Eq. (9) and the coefficient of determination (R^2 – Eq.(10) are commonly used for assessing the performance of the radiation models and were also used in this study.

$$RMSE = \sqrt{\frac{\sum_i \left(R_{mod_i} - R_{mea_i}\right)^2}{n}} \tag{8}$$

$$MBE = \frac{\sum_i R_{mod_i} - R_{mea_i}}{n} \tag{9}$$

$$R^2 = 1 - \frac{\sum_i \left(R_{mod_i} - R_{mea_i}\right)^2}{\sum_i \left(R_{mea_i} - \overline{R_{mea}}\right)^2} \tag{10}$$

The models were analysed on hourly and daily scales. For the daily averages, the fluxes were computed each hour and then averaged as recommended by Flerchinger et al. (2009). The solar radiation at TOA was computed using the mid-point of each time step.

The first step in this quantitative analysis was the separation of clear and cloudy sky periods. In the shortwave analysis, the cloudless skies were defined as:

- The ratio between $R_{S\downarrow}$ and $R_{S\downarrow TOA}$ equal to or larger than 0.75;
- The ratio between $R_{S\downarrow DIR}$ and $R_{S\downarrow}$ equal to or larger than 0.75.

As the two previous conditions rely on solar radiation, an extra standard was necessary for longwave as nighttime contributions are also significant. During this period, the cloud modification factor (c_{mf}(11) of the last and first sunshine hours were linearly interpolated. All points that had c_{mf} above 0.9 and satisfied the other two conditions at daytime were deemed clear.

$$c_{mf} = 1 - \frac{R_{S\downarrow clear}}{R_{S\downarrow}} \tag{11}$$

The cloud correction algorithms that relied on clear sky estimates were tested with different clear sky models to choose the best combination. Since clear sky methods can behave better than cloud corrections ones for all sky conditions (Marthews et al., 2012), the various parametrisations were assessed for both scenarios. As the performance of the methods for all skies is largely dependent on the accuracy and frequency of clear sky estimates (Carmona et al., 2014), the algorithms were also assessed for strictly cloudy conditions.

Since the accuracy of the models is highly dependent on the accuracy of the input data (Yu et al., 2018), different data sources were used as inputs for some methods, e.g. air temperature from ground data and modelled datasets. In all-sky LW methods, the performance was also evaluated considering two cloud representations (c_{mf} or $\underline{c_f}$) as in Li et al. (2017)

According to Suttles and Ohring (1986), a major limitation of net radiation models is the inadequate description of the conditions they can be applied due to the poor specification of the input parameters and their variability. Therefore, an error analysis was conducted to link the methods' performance to specific site characteristics, e.g. land cover, solar elevation angle, humidity, aerosol content and temperature.

The accuracies of the different algorithms were intercompared, and best set of algorithms for an hourly and daily estimate of R_n were defined.

4. SELECTION OF METHODS

In this chapter, the selection of models is separated by net radiation component. It starts with the choice of the upwelling elements, which was limited to existing products or simplified approaches. Then, the downwelling methods are selected: the shortwave ones were chosen based on the review of Ruiz-Arias and Gueymard (2018); for the longwave parametrisations, a more detailed review was conducted.

4.1. Upwelling Methods

4.1.1. Shortwave Upwelling Methods

The shortwave upwelling element can be expressed as a product of the surface downward solar radiation and the surface albedo ($R_{S\uparrow}=R_{S\downarrow}\rho_g$). The diurnal cycles of $R_{S\uparrow}$ will be largely dependent on the incoming radiation, as albedo fluctuations tend to happen at a larger temporal scale, related to changes in seasons and land cover (Shunlin Liang et al., 2013). Certainly, the amount of radiation reflected by the surface can also shift quicker, as in forest fires or intermittent snow events; however, its main variations happen in space. Therefore, for the correct estimation of the $R_{S\uparrow}$, it is mandatory to have a high spatial resolution of albedo and a high temporal resolution of the incoming solar flux.

Shunlin Liang et al. (2013) list global albedo products available in 2013. The one from the Moderate Resolution Imaging Spectroradiometer (MODIS) had the best spatial representation (0.5−1 km) and was, therefore selected for this study. It is recognised that MODIS is reaching the end of its lifetime; nevertheless, it is expected that other products from similar sensors, like Visible Infrared Imaging Radiometer Suite (VIIRS) will be more mature and accurate when MODIS stops working, smoothing the transition.

To check the importance of the spatial representation, the albedo of the Clouds and the Earth's Radiant Energy System (CERES) was calculated from its hourly $R_{S\uparrow}$ and $R_{S\downarrow}$ fluxes, available at 1° resolution.

4.1.2. Longwave Upwelling Methods

It is accepted that it is easier to calculate the longwave upwelling component than the downward one. Gui, Liang, and Li (2010) compared 4 longwave products retrieved from remote sensing with 15 locations for 2003 and confirmed all of them estimate $R_{L\uparrow}$ better than $R_{L\downarrow}$.

$R_{L\uparrow}$ has been traditionally estimated as a function of the LW downwelling element, surface emissivity and temperature (7). Sometimes, it is calculated by simply assuming $\epsilon_g \approx 1.0$ and $T_g \approx T_a$ (Yaping Zhou et al., 2007). More frequently, both ϵ_g and T_g are estimated directly via remote sensing in thermal and microwave bands; however, there large uncertainties in these products. An alternative solution is determining $R_{L\uparrow}$ directly from TOA longwave observations, in hybrid methods, as it is done in the CERES product.

CERES net radiation products were validated with ground data from 340 stations on a daily basis between 2000 and 2014 by Jia et al. (2016). They classified the estimate as strongly consistent. In their comparison, Gui et al. (2010) acknowledged CERES daily $R_{L\uparrow}$ estimates were better than the other 3 products analysed. Accordingly, this prediction was analysed here.

Additionally, an attempt to downscale this product was conducted using a ratio between the locally measured temperature and the one which is used as an input for CERES. The simplified approach used by Yaping Zhou et al. (2007) to retrieve the outgoing longwave radiation was also studied (7).

4.2. Downwelling Methods

The atmospheric constituents scatter and absorb shortwave radiation, but they do not emit it. The transmittance of the solar radiation can then be interpreted in the basis of two essentially independent processes. The first one is triggered by the clear sky atmospheric elements, mainly aerosols and water vapour; and the second one, by clouds. The all-sky $R_{S\downarrow}$ can be estimated by multiplying clear sky calculations ($R_{S\downarrow clear}$) with a cloud function that represents its transmissivity and backscattering (Ruiz-Arias & Gueymard, 2018). $R_{S\downarrow}$ is then directly proportional to $R_{S\downarrow clear}$. The effects of cloud in the longwave spectrum are more complex, as they also emit LW radiation. On these grounds, in this thesis, parametrisations were used to estimate only $R_{S\downarrow clear}$ fluxes, while existing products were used for all-sky $R_{S\downarrow}$. On the other hand, $R_{L\downarrow}$ was computed under clear and cloudy conditions; one $R_{L\downarrow}$ product was also analysed.

4.2.1. Shortwave Downwelling Methods

The choice of clear sky shortwave methods was based on the work performed by Ruiz-Arias and Gueymard (2018). These authors compiled 36 papers that validated parameterised $R_{S\downarrow clear}$ models to select the ones for their own research. This compilation included studies published between 1993 and 2017 and excluded articles which analysed the fluxes in long time steps (>1 hour) or which used machine learning. The 36 validations studies were then evaluated according to the number of ground stations, number of models tested, components ($R_{S\downarrow}$, $R_{S\downarrow DIR}$, $R_{S\downarrow DIF}$), time step and study area.

Their choice was then based on the recommendations of the authors, weight by the number of validation sites and number of models tested. Ruiz-Arias and Gueymard (2018) selected 15 algorithms to compute clear sky solar radiation an intercompared them in their own research.

Out of them, 8 models were validated in this thesis: (1) BH81, the Bird model, by Bird and Hulstrom, (1981a, 1981b); (2) IQ83 by Iqbal (1983); (3) MAC87 by J. A. Davies, Schertzer, and Nunez (1975); John A. Davies and McKay (1982); R. Davies, Randall, and Corsetti (1987); ESRA European Solar Radiation Atlas (ESRA) model by Rigollier, Bauer, and Wald (2000) with two different formulations for Linke Turbidity: (4) ER00 by Remund, Wald, Lefevre, Ranchin, and Page (2003); and (5) EI00 by Ineichen (2008b); (6) IN08 by Ineichen (2008a); (7) RES08, REST2 model, by Gueymard (2008); and (8) DF14 by Dai and Fang (2014). The reasons for exclusion of the other 7 methods were the availability of inputs and incomplete presentation of the equations in the publications.

Table 4-1 summarises the inputs required by each $R_{S\downarrow clear}$ model. All of them demand an estimate of the shortwave radiation at the top of the atmosphere, which is a function of latitude, the day of the year and the time. A better description of these models is presented in Section 6.1 and of the input in Chapter 5.

Additionally, $R_{S\downarrow}$ products from geostationary satellites (GOES and MSG) were also checked.

Table 4-1 – Inputs required by each shortwave downwelling model

	Model	p_g	p_{sl}	w	τ_{380}	τ_{500}	τ_{550}	τ_{700}	α	β	O_3	ρ_g	ω_0	k_1	B_a	NO_2
$R_{S\downarrow clear}$	**BH81**	■	■	■	■	■					■	■		■	■	
	IQ83	■	■	■					■	■	■	■	■		■	
	MAC87	■	■	■	■	■					■	■	■		■	
	ER00	■	■	■						■						
	EI00	■	■	■			■									
	IN08	■	■	■				■								
	RES08	■	■	■					■	■	■	■	■			■
	DF14	■	■	■		■			■							

4.2.2. Longwave Downwelling Methods

For the downward longwave component, a collection similar to the work of Ruiz-Arias and Gueymard (2018) was performed: 21 papers which relate parameterised methods with ground measurements of were analysed. Their publication dates go from 2001 to 2018. The articles were investigated considering: the sky conditions the methods were applied in; the temporal steps; the number of models tested; the number of ground stations and their locations; the input data source; the period analysed; and which models were recommended. Table 4-2 contains the result of this gathering.

In this table the column "Number of models", the amount is not always the same as the ones the authors claimed to have analysed, as some of them correspond to different calibrations of the same model; furthermore, the numbers between parenthesis in that column correspond to methods developed in that paper. For "Ground stations", the total between parenthesis include the stations also analysed in this thesis. The column "Best models" does not necessarily correspond to the suggestions of the authors: they represent the methods that behave better without local calibration.

For the clear sky parametrisations, Brunt (1932)[1] and Brutsaert (1975) were deemed the best models by many of the paper analysed in Table 4-2. They are frequently used to estimate $R_{L\downarrow clear}$. Wang and Liang, (2009) checked the performance of these two methods in 36 stations and concluded both predict $R_{L\downarrow clear}$ well over most surfaces on a global scale. An additional model, not represented in Table 4-2, was considered in this study: the net longwave model predicted by Food and Agriculture Organization of the United Nations (FAO) (Allen, Pereira, Raes, & Smith, 1998), the 'FAO-56 method'. As it consists of a variation of Brunt method, it was redundant to consider both.

According to Carmona et al. (2014), Duarte, Dias, and Maggiotto (2006), Santos, Da Silva, Rao, Satyamurty, and Manzi, (2011), the models that do not include the water content of the atmosphere generally perform worse, so the models by Swinbank (1963) and by Idso and Jackson (1969) were not analysed.

Analysing Table 4-2, the only apparent consensus for all-sky $R_{L\downarrow}$ is Crawford and Duchon (1999). Because of the difficulties to estimate the LW downward component for cloudy conditions, more methods for these circumstances were selected than for clear skies.

Abramowitz, Pouyanné, and Ajami (2012) developed their all-sky LW model using data from ground stations in many different climates without any cloud inputs, so it was relevant to test it.

Based on the compilation, 10 models were selected: (1) BT75 by Brutsaert (1975); (2) PT96 by Prata (1996); (3) DB98 the B model by Dilley and O'Brien (1998); (4) AB12 by Abramowitz et al. (2012); (5) MK73 by Maykut and Church (1973); (6) CD99 by Crawford and Duchon (1999); (7) KB82 by Kimball, Idso, and Aase (1982); (8) SC86 by P. Schmetz, Schmetz and Raschke (1986); (9) DK00 by Diak et al. (2000); and (10) ZC07 by Yaping Zhou et al. (2007).

In an extensive review of longwave downwelling fluxes, Wang and Dickinson (2013) compared reanalysis and RS products with ground data from 193 stations between 1992 and 2003 on a monthly basis. They concluded the products from CERES were more accurate. On a daily analysis, Gui et al. (2010) also determined these were more accurate than the other 3 $R_{L\downarrow}$ products analysed. Accordingly, this prediction was also analysed here.

[1] The coefficients for the Brunt model are the ones presented by Sellers (1965) as the original publication does not specify a calibration.

Table 4-2 – Surface downwelling longwave radiation validation studies of the literature.

Paper	Sky conditions	Time step	# of models		Ground stations		Input data source	Period	Best models	
			Clear Sky	All-sky	#	Location			Clear	Cloudy
Yu, et al. (2018)	Cloudy	Daytime and nighttime	0	8	13(2)	China, US, Spain, Israel, Algeria, Australia, Papua New Guinea, Antarctica	Synthetic, Ground, Satellite and Reanalysis	2010	-	Diak et al. (2000); Gupta, Kratz, Stackhouse, and Wilber (2001); P. Schmetz et al. (1986); Yaping Zhou et al. (2007)
Li, et al. (2017)	All	<30min	15	4(1)	7(7)	US	Ground data	2012, 2013	Idso (1981); Niemelä, Räisänen, & Savijärvi (2001); Prata (1996); Satterlund (1979)	Crawford and Duchon (1999)
Zhu, et al. (2017)	All	Hourly	13	9	5	Tibetan Plateau	Ground data	2010, 2011-2013	Idso (1981); Idso and Jackson (1969); Prata (1996); Swinbank (1963)	Sicart, Pomeroy, Essery, and Bewley (2006)
Carmona, et al. (2014)	All	Hourly (no nighttime)	6	8(2)	8	Argentina	Ground data	2007-2010	Brunt (1932); Brutsaert (1975)	Crawford and Duchon (1999)
Choi (2013)	All	30 min (no nighttime)	6	8	2	Korea	Ground data	2006	Brunt (1932); Brutsaert (1975); Prata (1996)	Maykut and Church (1973)
Abramowitz, et al (2012)	All	30 min	4	2(1)	10	US, Canada, Netherlands, Italy, Australia, South Africa, Botswana	Ground data	1997-2006	Own model	
Alados, et al. (2012)	All	<30 min (no nighttime)	5	1	2	Spain, France	Ground data	2001-2003, 2006	Brutsaert (1975)	-
Gubler, et al. (2012)	All	Hourly	12	2(1)	6	Switzerland	Ground data	1996-2008	Brunt (1932); Brutsaert (1975); Dilley and O'Brien B model (1998)	Own model
Marthews, et al. (2012)	All	Hourly	18	6	1	Brazil	Ground data	2002-2003	Dilley and O'Brien B model (1998)	Kimball et al. (1982)
Wu, Zhang, Liang, Yang, and Zhou (2012)	Clear sky	Instantaneous	8	0	23(3)	US, Asia, Europe	Satellite data	2000-2006	Ångström (1915); Dilley and O'Brien B model (1998); Prata (1996)	-

Table 4-2 (continued)

Paper	Sky conditions	Time step	# of models		Ground stations		Input data source	Period	Best models	
			Clear Sky	All-sky	#	Location			Clear	Cloudy
Santos, et al. (2011)	Clear sky	Daytime and nighttime	5	0	1	Brazil	Ground data	2005-2006	Brutsaert (1975); Prata (1996)	-
Wang & Liang (2009)	All	Instantaneous and daily (no nightime)	2	1	36(7)	US, Asia, Australia, Africa	Ground data	1995-2007	Brunt (1932); Brutsaert (1975)	-
Flerchinger, et al. (2009)	All	30min/hourly and daily	13	10	21	US, China	Ground data	1982-2007	Ångström (1915); Dilley and O'Brien B model (1998); Prata (1996)	Crawford and Duchon (1999); Kimball et al. (1982); Unsworth and Monteith (1975)
Choi, et al. (2008)	All	Daily	5	7	11	Florida	Ground data	2004-2005	Brunt (1932)	Crawford and Duchon (1999)
Bilbao and de Miguel (2007)	All	Daytime	4	1(1)	1	Spain	Ground data	2001-2004	Brunt (1932)	Own model.
Kjaersgaard, et al. (2007)	All	Hourly (no nighttime)	11	2	2	Denmark	Ground data	1973-2005	Brutsaert (1975); Prata (1996)	
Duarte, et al. (2006)	All	Daytime	5	5	1	Brazil	Ground data	2003 -2004	Brutsaert (1975)	Crawford and Duchon (1999); Jacobs (1978)
Finch and Best (2004)	Clear sky	Daily	5	0	Global grid	Global	Global Climate Model	1979-1988	Brutsaert (1975); Garratt (1992); Idso and Jackson (1969)	-
Pérez-García (2004)	Clear sky	Nighttime	4	0	1	Spain	Ground data	1992-1994	Brunt (1932)	-
Iziomon, Mayer and Matzarakis (2003)	All	Hourly	7	1(1)	3(1)	Germany, US	Ground data	1992-1995	Brunt (1932); Brutsaert (1975)	Own model.
Niemelä, et al. (2001)	All	Hourly (no daytime)	9(1)	3(1)	1	Finland	Ground data	1997-1999	Ångström (1915); Dilley and O'Brien B model (1998); Idso (1981); Prata (1996); Own model	Maykut and Church (1973); Own model.

Table 4-3 summarises the inputs required by each one of the selected $R_{L\downarrow}$ models and by FAO-56. ZC07 requires an estimate of the upwelling flux; however, in their work, they approximate it using screen air temperature in the simplified approach defined in Section 4.1.2. The same was done here. The models are better described in Section 6.2 and the input data in Chapter 5.

Table 4-3 – Inputs required by each longwave downwelling model

	Model	T_a	e_0	w	c_f	T_c	ϵ_{clouds}	w_{cw}	w_{ci}	$R_{S\downarrow clear}$	$R_{S\downarrow}$	$R_{L\downarrow clear}$
$R_{L\downarrow clear}$	**BT75**	■	■									
	PT96	■		■								
	DB98	■		■								
$R_{L\downarrow}$	**AB12**	■	■									
	FAO56	■	■							■	■	
	MK73	■			■							■
	CD99	■								■	■	■
	KB82				■	■	■					■
	SC86	■			■	■	■					■
	DK00				■	■	■					■
	ZC07	■		■	■			■	■			

5. DATASET

5.1. Overview

Table 5-1 gives an overview of the sources, units and spatiotemporal resolutions of the data used in this work, which was downloaded for the whole of 2017. The Baseline Surface Radiation Network (BSRN) provides surface radiation fluxes measured in ground stations, as well as auxiliary meteorological parameters (Driemel et al., 2018). The Goddard Earth Observing System (GEOS) data comes from the most recent validated Atmospheric General Circulation Model of the National Aeronautics and Space Administration (NASA) (Rienecker et al., 2008). CERES delivers radiative fluxes along with auxiliary cloud variables. The MODIS sensor on board of the Terra and Aqua satellites prepares a 16-days albedo product (Schaaf & Wang, 2015). Geostationary Operational Environmental Satellites (GOES) and Meteosat Second Generation (MSG) are geostationary satellites that provide downward surface shortwave fluxes; the first one covers the Americas while the second one, Africa and Europe.

Table 5-1 – Sources, units and spatiotemporal resolutions of the dataset

Source	Name		Unit	Resolution	
	Symbol	Long name		Temporal	Spatial
BSRN	$R_{S\downarrow}$	Surface Shortwave Downwelling Radiation	W m^{-2}	1 min	Ground data
	$R_{S\downarrow DIR}$	Surface Solar Direct Radiation	W m^{-2}	1 min	Ground data
	$R_{S\downarrow DIF}$	Surface Solar Diffuse Radiation	W m^{-2}	1 min	Ground data
	$R_{S\uparrow}$	Surface Shortwave Upwelling Radiation	W m^{-2}	1 min	Ground data
	$R_{L\downarrow}$	Surface Longwave Downwelling Radiation	W m^{-2}	1 min	Ground data
	$R_{L\uparrow}$	Surface Longwave Upwelling Radiation	W m^{-2}	1 min	Ground data
	T_a	Air Temperature at 2m	°C	1 min	Ground data
	RH	Relative Humidity at 2m	%	1 min	Ground data
GEOS	T_a	Air Temperature at 2m	K	1 hour	0.25°x0.312°
	e_0	Vapour Pressure at 2m	bar	1 hour	0.25°x0.312°
	p_g	Surface Pressure	Pa	1 hour	0.25°x0.312°
	p_{sl}	Sea Level Pressure	Pa	1 hour	0.25°x0.312°
	τ_{550}	Aerosol Optical Depth at 550 nm	-	3 hours	0.25°x0.312°
	α	Ångström Exponent	-	3 hours	0.25°x0.312°
	w	Total Column Atmospheric Water Vapour	kg m^{-2}	1 hour	0.25°x0.312°
	O_3	Total Column Atmospheric Ozone	D. U.	1 hour	0.25°x0.312°
CERES	c_f	Cloud Fraction	-	1 hour	1°
	T_c	Cloud Temperature	K	1 hour	1°
	τ_c	Cloud Visible Optical Depth	-	1 hour	1°
	w_{cw}	Cloud Liquid Water Path	g m^{-2}	1 hour	1°
	w_{ci}	Cloud Ice Water Path	g m^{-2}	1 hour	1°
	$R_{S\downarrow}$	Surface Shortwave Downwelling Radiation	W m^{-2}	1 hour	1°
	$R_{S\uparrow}$	Surface Shortwave Upwelling Radiation	W m^{-2}	1 hour	1°
	$R_{L\downarrow}$	Surface Longwave Downwelling Radiation	W m^{-2}	1 hour	1°
	$R_{L\uparrow}$	Surface Longwave Upwelling Radiation	W m^{-2}	1 hour	1°
MODIS	ρ_g	Ground albedo	-	16 days	500 m
GOES	$R_{S\downarrow}$	Surface Shortwave Downwelling Radiation	W m^{-2}	Hourly	1°
MSG	$R_{S\downarrow}$	Surface Shortwave Downwelling Radiation	W m^{-2}	30 min	1°

It is necessary to use globally available data as input when trying to select a that can be globally applicable. Global gridded databases are provided by satellites or atmospheric reanalysis/models. In this work, the atmospheric variables derived from GEOS were employed as it does not have the data gaps that commonly happen to satellite products due to clouds and orbit constraints.

The choice of the source of the cloud parameters was mainly motivated by their high temporal variation. Some polar orbiting sensors could provide the cloud parameters in better spatial resolutions, but they would require temporal interpolation for routine agricultural applications. The cloud variables were downloaded from CERES, which combines the cloud products from polar and geostationary satellites, in virtue of their high temporal resolution (1 hour). Furthermore, its good cloud representation is one of the reasons why CERES longwave downward estimates were deemed more accurate than similar satellite/reanalysis products (Wang & Dickinson, 2013).

The radiative data from BSRN was used for validation purposes while the meteorological were used as inputs. It can be observed from Table 5-1 that the temperature and moisture data can be obtained from BSRN and GEOS. They were both used to compare the performance of the methods, as ground data is usually of better quality, but not always available.

As described in Chapter 4, the radiative fluxes from CERES and the shortwave fluxes from geostationary satellites (GOES and MSG) were also downloaded for validation.

5.1.1. BSRN

There are various types of radiometers with different accuracies. In a comparison between modelled predictions and local observations, it is important the validation data are of good quality. Even though it limits the spatial coverage of the study, only data from the high-quality BSRN was used in this work. This network operates only with first class radiometers that are frequently calibrated (Driemel et al., 2018). For each station, a scientist is responsible for the condition of the submitted data, which undergo a preliminary quality assessment.

The objective of the BSRN is to provide surface radiation fluxes data at the best possible quality with a high sampling rate (1 min). The data is available for *bona fide* research at no cost near real time[2]. The network is designed to cover major climatic zones. The current readings come from 59 stations[3], of which 21 provide measurements of all four net radiation components ($R_{S\downarrow}$, $R_{S\uparrow}$, $R_{L\downarrow}$, $R_{L\uparrow}$) as well as the solar irradiance elements ($R_{S\downarrow DIR}$, $R_{S\downarrow DIF}$). Excluding the stations located outside the study area (i.e. high latitudes), 10 stations of BSRN were used in this study, of which 7 belong to the Surface Radiation Budget Network – SURFRAD (Augustine, DeLuisi, & Long, 2000; Augustine, Hodges, Cornwall, Michalsky, & Medina, 2005). The characteristics of each station are detailed in Table 5-2, in which stations marked with a * belong to SURFRAD network.

To be representative of the environmental conditions of the US, SURFRAD locations were chosen considering the uniformity of the landcover. Further on, they could not be located near to large bodies of water or major sources of anthropogenic aerosol emissions. The immediate-surrounding land cover of the other 3 stations is also homogeneous. The river Lek, approximately 300m wide, is located within 1 km of the station CAB; GOB is located in the vicinity of a sand desert.

[2] https://bsrn.awi.de/data/data-retrieval-via-ftp/

[3] Number of BSRN stations active at the end of 2017 according to Driemel et al. (2018)

Table 5-2 – Summary of the location of the ten ground-stations

Code	Name	Country	Latitude (º)	Longitude (º)	Elevation (m)	Surface	Topography
BON*	Bondville	USA	40.0519	-88.3731	230	Grass	Flat, Rural
CAB	Cabauw	Netherlands	51.9711	4.9267	0	Grass	Flat, Rural
DRA*	Desert Rock	USA	36.6237	-116.0195	1007	Gravel	Flat, Rural
E13	South Great Plains	USA	36.6050	-97.4850	318	Grass	Flat, Rural
FPK*	Fort Peck	USA	48.3078	-105.1017	634	Grass	Flat, Rural
GOB	Gobabeb	Namibia	-23.5614	15.0420	407	Desert	Flat, Rural
GWN*	Goodwin Creek	USA	34.2547	-89.8729	98	Grass	Hilly, Rural
PSU*	Rock Springs	USA	40.7201	-77.9309	376	Cultivated	Mountain Valley, Rural
SXF*	Sioux Falls	USA	43.7340	-96.6232	473	Grass	Hilly, Rural
TBL*	Boulder	USA	40.1250	-105.2368	1689	Grass	Hilly, Rural

The radiometers in the SURFRAD and E13 are elevated 10m from the surface, while the elevation of the other ones is 2m. These stations are equipped with Eppley radiometers, while the ones from CAB and GOB use equipment from the brand Kipp & Zonen. The ranges of these two brands are about 280 to 3000 nm and 200-3600 nm respectively for the shortwave and 3000-50,000 nm and 4500-40,000 nm, respectively for the longwave. The calibration accuracy of all instruments is below 5% for hourly averages of shortwave radiation, and under 10 W/m² for the longwave. The operation uncertainties in field conditions might be higher than that.

The pyranometers that measure global and diffuse solar radiation are susceptible to thermopile cooling to space, which result in small negative signals at night. This offset is also present in daytime, but it is masked by the solar signal. In the SURFRAD, the instrument that measures the diffuse component has been changed to a "black and white" model, which does not have this behaviour. The global solar irradiance is still measured with the same equipment. It is therefore recommended to calculate global solar irradiance as a sum of the direct and diffuse irradiances. The Kipp & Zonen measurements also present this offset. The scientists responsible for the stations CAB and GOB do not mention any correction

The stations also provide relative humidity (RH) and air temperature (T_a) data, which were used as inputs.

5.1.2. GEOS AND CERES

The Global Modelling and Assimilation Office of NASA provides GEOS data products in near real-time for research purposes. Their Atmospheric General Circulation Model (AGCM) can be run with different spatial and temporal resolutions. However, the global products are available[4] in the ones specified in Table 5-1. AGCM is a physically based atmospheric model. Actual measurements of aerosol, temperature, pressure, moisture and ozone from various sources are constantly added to keep its the simulation as accurate as possible (NASA, 2015). The products "totexttau" (τ_{550}) and "totangstr" (α) from GEOS5 FP 2d

[4] https://fluid.nccs.nasa.gov/weather/

time-averaged primary aerosol diagnostics (tavg3_2d_aer_Nx) along with "ps" (p_g), "tqv" (w), "to3" (O_3), "slp" (p_{sl}), "t2m" (T_a) and "qv2m" (e_0), from the single level diagnostics (tavg1_2d_slv_Nx) were downloaded to be used as inputs for the methods.

The fourth edition of Synoptic Radiative Fluxes and Clouds hourly gridded product (SYN1deg-1Hour) from CERES[5] is used in this study. The surface fluxes are computed with Langley Fu-Liou Radiative Transfer Code using MODIS and geostationary cloud products, MODIS aerosol and GEOS-5 atmospheric profiles. The computed TOA fluxes are tuned with the ones observed by CERES instruments, which are on board of different satellites, like Terra, Aqua and S-NPP (NASA, 2018). The cloud products from the polar-orbiting satellites offer a better view of the optically thin clouds and the cloud base height, while the geostationary products give a better understanding on their diurnal variation (Kato et al., 2011). The surface adjusted fluxes ($R_{S\downarrow}$, $R_{S\uparrow}$, $R_{L\downarrow}$, $R_{L\uparrow}$) were downloaded. The coincident total cloud parameters (ε_T, T_c, τ_c, w_{cw}, w_{ci}); were acquired to be used as inputs for the cloud correction algorithms. Additionally, the direct and diffuse radiation were downloaded to be used as auxiliary data, more specifically: they were used to compute the albedo and to define clear sky days.

5.1.3. MODIS, GOES AND MSG

MCD43A3[6] Version 6 Albedo Model of MODIS is a 16-days composite. The algorithm combines the atmospherically corrected surface reflectance data from multiple bands and dates to fit a Bidirectional Reflectance Distribution Function (BRDF) (Strahler et al., 1999). It operates with the best representative pixels from Terra and Aqua sensors, which are weighted according to the central date of the period. The algorithm performs angular integrations to deliver the directional hemispherical reflectance (black sky albedo) as well as the bi-hemispherical reflectance (white sky albedo) for each of the MODIS bands along with the global shortwave band, used in this study. This compound has achieved stage 3 validation and delivers quality layers for each band.

The Geostationary Surface and Insolation Product (GSIP) are produced hourly for the northern hemisphere using radiance data from GOES-East and -West sensors (Milan, 2011). For every pixel, their complex algorithm sets the one with least clouds in a period of 28 days as a clear sky reference. They employ auxiliary data from the NCEP Global Forecast System (GFS) model: surface pressure, profiles of temperature and humidity, precipitable water and ozone. Using those inputs and the clear sky reference, it estimates the cloud variables and the surface radiative fluxes. The surface $R_{S\downarrow}$ (200-4000nm) is only produced when the cosine of the solar zenith angle is greater than 0.2. The GOES-East Imager Northern Hemisphere Extended Scan Sector acquired[7] for this work comes in a 1º grid cell and has reached level 3 in NOAA processing.

The European Organization for the Exploitation of Meteorological Satellites (EUMETSAT) Satellite Application Facility on Land Surface Analysis (LSA-SAF) estimates the $R_{S\downarrow}$ (300 to 4000 nm) on a 30-min basis. It uses the three shortwave channels of the SEVIRI sensor onboard of the MSG satellite and auxiliary cloud, aerosol, water vapour, ozone and albedo inputs (Trigo et al., 2011). The product has different algorithms for the clear and cloudy skies: the first one uses transmission functions which rely on atmospheric components while the second one assumes a homogeneous cloud covers the whole pixel and incorporates cloud albedo and transmittance (LSA SAF, 2011). The Downward Surface Shortwave Flux (DSSF) 30 min level 2 product[8], which contains the fluxes and their quality flags, were downloaded for this work.

[5] https://ceres-tool.larc.nasa.gov/ord-tool/jsp/SYN1degEd4Selection.jsp

[6] https://e4ftl01.cr.usgs.gov/MOTA/MCD43A3.006/

[7] https://www.bou.class.noaa.gov/saa/products/search?sub_id=0&datatype_family=GSIP&submit.x=20&submit.y=2

[8] https://landsaf.ipma.pt/products/disseminationMethod.jsp

5.2. Pre-processing

For BSRN, the pre-processing started by deleting poor data previously identified by the station scientists through the quality flag. The UT offset was then corrected. When the sun was below the horizon, the values of the shortwave fluxes were set to zero. The recommended quality checks of Long and Dutton, (2010); and Roesch et al. (2011), which include physically possible limits and comparison between fluxes, were performed. In this process, 1.10%, 0.76%, 0.16%, 0.10% and 0.07% of points were lost for $R_{S\downarrow DIF}$, $R_{S\uparrow}$, $R_{S\downarrow DIR}$, $R_{L\downarrow}$, $R_{L\uparrow}$, respectively.

According to the recommendations, the $R_{S\downarrow}$ fluxes were computed as a sum of $R_{S\downarrow DIR}$ and $R_{S\downarrow DIF}$ when these were available. The fluxes and inputs were hourly averaged. For that, at least 70% of the data for each hour should be present. The vapour pressure was calculated according to the FAO 56 paper (Allen et al., 1998) considering the highest and lowest *RH* and temperature (T_a) values of each hour (APPENDICES Appendix A: formulas. Non-available hourly inputs were linearly interpolated.

Data from CERES, GOES, MSG, GEOS and MODIS come in image files of different formats. The first step was to extract the information of the pixel which contains the ground station of the BSRN network. When quality flags were available, they were used to exclude poor quality data. The UT offset of the first four sources were corrected. The same quality checks for BSRN data were conducted for the radiative fluxes in the first three products.

The aerosol inputs of GEOS are available every three hours. Their value was assumed to be constant in this interval. The units of some of the inputs from GEOS and BSRN were converted: temperatures were changed to Kelvin, pressure variables to hPa, total column atmospheric water vapour and ozone to cm.

For the daily averaging, all the radiative fluxes should have values in at least 23 hours. The white and black sky albedo from MODIS were converted to broadband albedo using the diffuse fraction from CERES.

Figure 5-1 summarizes the main characteristics of the dataset in whisker plots, constructed for the individual stations and the total dataset. In this figure, all the values corresponding to hourly averages, except the albedo, which is represented daily. The atmospheric water content is represented both in vapour pressure computed from BSRN (Figure 5-1.f) and in total precipitable water (Figure 5-1.g), from GEOS.

The input ranges analysed in this study were $-38.87<T_a<58.96$ºC, $0.16<e_0<26.67$hPa, $0.04<w<7.14$cm and $0.0<\tau_{550}<3.94$. In Figure 5-1.a, it can be seen the difference in $R_{S\downarrow}$ between stations located in a smaller (GOB) and bigger latitudes (CAB). A relationship can be seen between temperature (Figure 5-1.e) and $R_{L\downarrow}$ (Figure 5-1.b), especially for the stations with the lowest (FPK) and higher (GOB) temperatures. For the stations located in desert/gravel areas (DRA and GOB), the $R_{L\uparrow}$ tend to be higher (Figure 5-1.c). The presence of snow can be easily seen in the albedo plot (Figure 5-1.d) for the stations FPK, SXF and, in a smaller extent, TBL and BON. The atmospheric water content is lower in DRA, FPK and TBL; while GWN, BON and E13 are the most humid (Figure 5-1.f and Figure 5-1.g). The aerosol optical depth remains below 0.5 in most situations. It has its lowest values in the station in a gravel area (DRA), while more outliers are 0.5 are seen in FPK, PSU and BON.

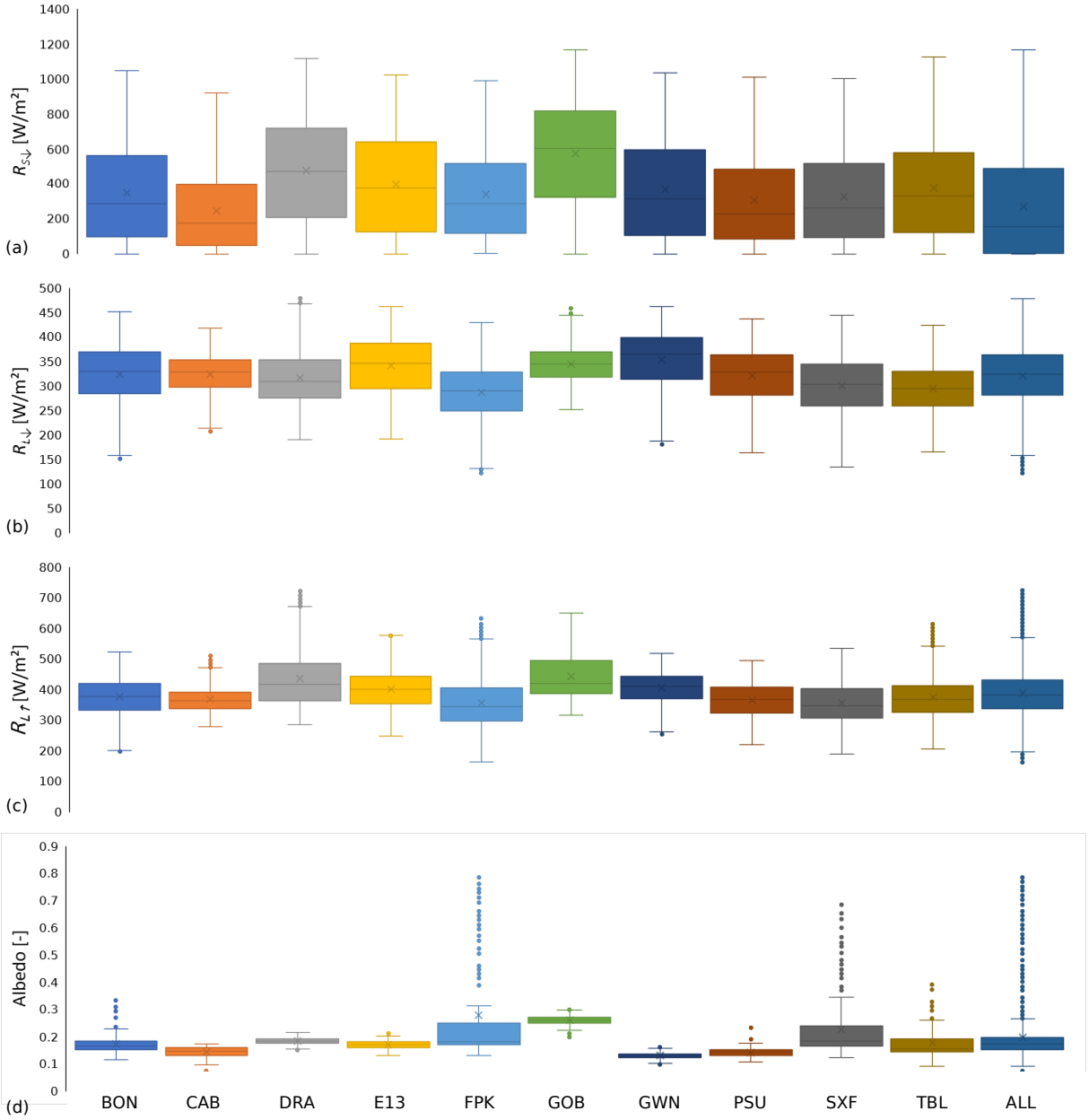

Figure 5-1 – Whisker plots of $R_{S\uparrow}$ (a), $R_{L\uparrow}$ (b), $R_{L\downarrow}$ (c), albedo (d), temperature (e), vapour pressure (f), total precipitable water (g) and aerosol optical depth at 550nm (h) by ground station

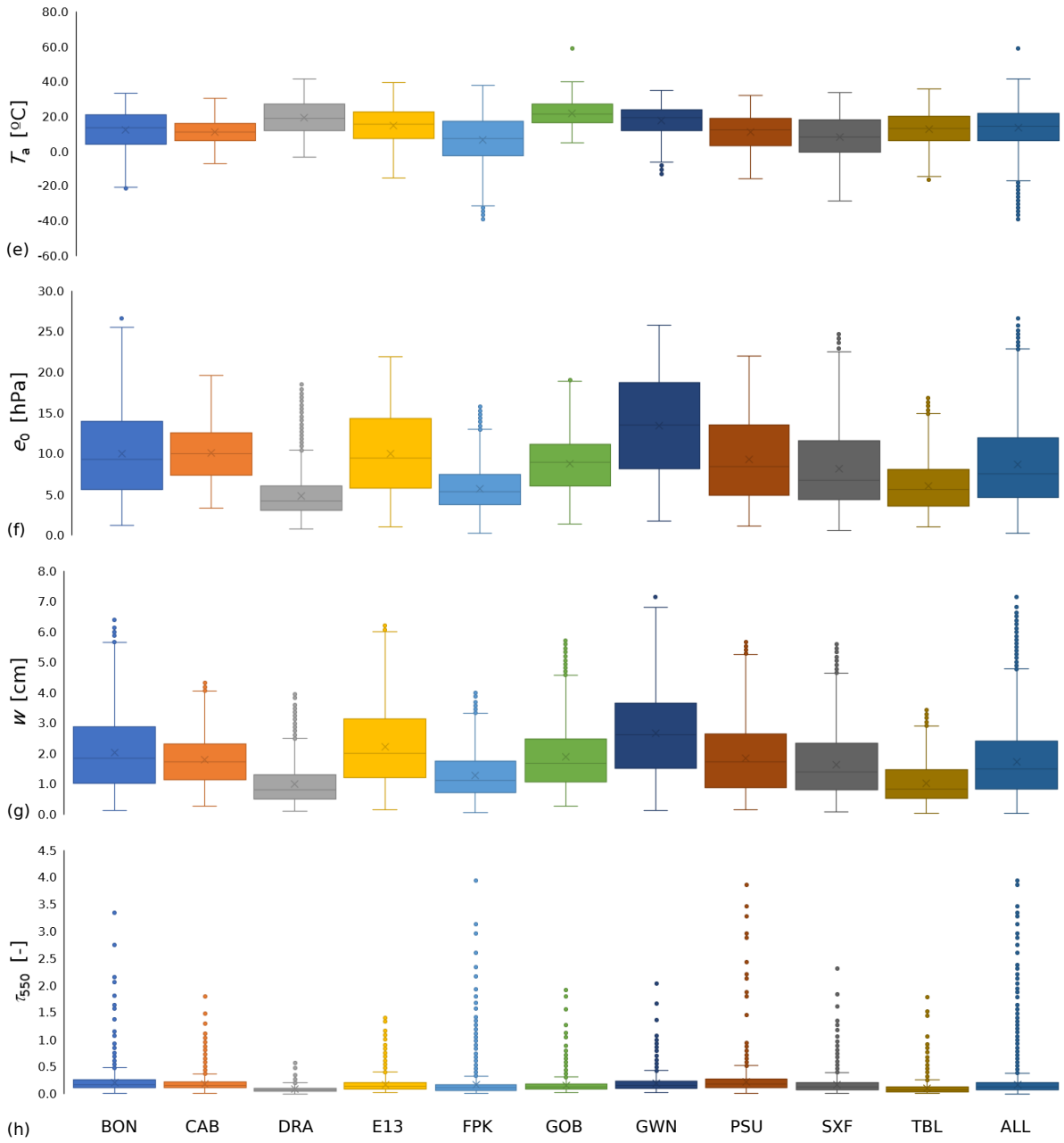

Figure 5-1 (continued)

6. DESCRIPTION OF SELECTED METHODS

6.1. Shortwave Downwelling Methods

The selected models are mostly based on transport or empirical equations to represent the transmissivity of the solar radiation. In the ESRA models (Rigollier et al., 2000), the Linke Turbidity is used to combine the effects of the water vapour and aerosol. This model, Ineichen (2008b); and Dai and Fang (2014) don't consider the surface albedo, so they do not account for backscattering effects. In some cases, the models consist of a simplification of more complex radiative transfer approaches (Bird & Hulstrom, 1981a; Gueymard, 2008; Ineichen, 2008a). Many models rely on the Beer-Lambert law (12), to estimate transmissivity (T_i) of the atmospheric element i based on its optical depth (τ_i) and the air mass m.

$$T_i = \exp(-m\tau_i) \tag{12}$$

For consistency, the incident shortwave radiation at the top of the atmosphere ($R_{S\downarrow TOA}$) was calculated in the same way for all models as in Equation (3). The computation ε and h_0 is detailed in the APPENDICES Appendix A: formulas. m was calculated according to (Kasten & Young, 1989) (13), where h_0 is in degrees, for all models that require it unless stated otherwise. Some models use the pressure corrected air mass m' (14).

$$m = (\sin h_0 + 0.50572(h_0 + 6.07995)^{-1.6364})^{-1} \tag{13}$$

$$m' = {}^{p}/_{p_{sl}}\, m \tag{14}$$

In models that utilize the aerosol optical depth in wavelengths (τ_λ) other than 550 nm, the Ångström's Law (15) was used. The Ångström's turbidity coefficient, β, was calculated based on the Ångström's exponent, α, and the optical depth at 550nm, τ_{550} (16).

$$\tau_\lambda = \beta\lambda^{-\alpha} \tag{15}$$

$$\beta = \tau_{550} 0.55^{\alpha} \tag{16}$$

In the next sessions, the models analysed in this study will be shortly described. The main equations for each model are presented, while ancillary ones are shown in the APPENDICES
Appendix A: formulas. Further details can be found in the original publications.

6.1.1. Bird Model (BH81)

Bird and Hulstrom (1981a) constructed a model that would work with readily available meteorological data based on SOLTRAN atmospheric transmission model. For the direct solar radiation ($R_{S\downarrow DIR\ clear}$) (17), it uses five transmittance factors: T_R, T_O, T_{UM}, T_w and T_A which are related to Rayleigh scattering; ozone, uniformly mixed gases (carbon dioxide and oxygen) and water vapour absorptances; and aerosol extinction, respectively. The 0.9662 factor was added by the authors because the SOLTRAN spectral interval is from 0.3 to 3.0 µm. For the solar irradiance from atmospheric scattering ($R_{S\downarrow ASclear}$) (18), the model separates the effects of aerosol absorptance, expressed by T_{AA} and scattering, T_{AS}. B_a is the ratio of the forward-scattered irradiance to the total scattered irradiance due to aerosols. The global shortwave radiation (19) considers the effect of multiple reflections between the atmosphere and the ground; it is computed by considering the ground and sky albedos, ρ_g and ρ_s.

The original formulation does not include the Earth-Sun distance, which was added in this work. Following what was suggested by the authors, the values of B_a=0.84 and K_l=0.1 were used since there was no reliable information on the aerosol type.

$$R_{S\downarrow DIR_{clear}} = 0.9662 R_{S,TOA\downarrow} T_R T_O T_{UM} T_w T_A \quad (17)$$

$$R_{S\downarrow AS_{clear}} = \frac{0.79 R_{S,TOA\downarrow} T_O T_{UM} T_w T_{AA} \left(0.5(1 - T_R) + B_a(1 - T_{AS})\right)}{1 - m + m^{1.02}} \quad (18)$$

$$R_{S\downarrow_{clear}} = \frac{R_{S,DIR\downarrow_{clear}} + R_{S,AS\downarrow_{clear}}}{1 - \rho_s \rho_g} \quad (19)$$

6.1.2. Iqbal Model (IQ83)

The direct irradiance model-C from Iqbal (1983) is a modification of the Bird approach. It also uses five transmittance factors for the direct irradiance (20) , which are all computed the same way, except for the aerosol extinction factor. This element was originally computed for situations in which Ångström's turbidity coefficient β<0.5.

The diffuse component also considers multiple reflections and is calculated as in Bird assuming of B_a=0.84, and K_I=*1*-ω_0, where ω_0 is the is the single-scattering aerosol albedo. For consistency, ω_0 value was set as 0.9. The global radiation is the sum of the direct and diffuse components, and the terrain reflected radiation ($R_{S\downarrow TER}$), which, for flat surfaces, can be approximated as in equation (21).

$$R_{S\downarrow DIR_{clear}} = 0.9751 R_{S,TOA\downarrow} T_R T_O T_{UM} T_w T_A \quad (20)$$

$$R_{S\downarrow TER_{clear}} = 0.03 \rho_g \left(R_{S,DIR\downarrow_{clear}} + R_{S,DIF\downarrow_{clear}}\right) \quad (21)$$

6.1.3. MAC Model (MAC87)

The MAC model was first developed at McMaster University by J. A. Davies et al. (1975) based on ground observations in Canada. In its 1982 formulation by John A. Davies and McKay for the direct beam (22), the solar radiation is attenuated by Rayleigh scattering (T_R), ozone (T_O) and water vapour (a_w) absorptions, as well as aerosol extinction (T_A). The diffuse component for atmospheric scattering (23) is made of two terms, one for Rayleigh scatter and the second one for scattering by aerosol, which includes B_a and ω_0. As in Bird's model, global radiation considers the effect of the sky and ground albedos. In the original paper, the ozone depth was fixed at 3.5 mm and the water path was calculated based on a locally fitted equation related to dew point temperature. In this work, the water and vapour contents were entered directly as an input, and, for consistency, B_a=0.84 and ω_0=0.9.

$$R_{S\downarrow DIR_{clear}} = R_{S,TOA\downarrow}(T_O T_R - a_w) T_A \quad (22)$$

$$R_{S\downarrow AS_{clear}} = R_{S,TOA\downarrow}(0.5 T_O(1 - T_R) + (T_O T_R - a_w)(1 - T_A)\omega_0 B_a) \quad (23)$$

Due to its simplistic representation of the aerosol extinction, which was diminishing its performance, MAC's proponents have suggested using a version the Beer-Lambert law (12) that uses the pressure corrected air mass (Gueymard, 2003). The aerosols optical depth in this work was calculated based on Bird's model, adapting it to the globally available inputs. The Rayleigh scattering element was modified in a later version of the model since the various polynomial expressions by the original author resulted in numerical instability, the formula used here is presented in (Gueymard, 2012).

6.1.4. ESRA Model (EI00 and ER00)

The current model used by the European Solar Radiation Atlas (ESRA) has its latest version in Rigollier et al. (2000). To estimate the beam component (24), it employs the classical Linke formulation. It expresses the total optical thickness of a cloudless atmosphere as a product of *m'*, the pressure corrected airmass; δ_R, the optical thickness of a pure Rayleigh scattering atmosphere (aerosol- and water-free); T_{LK2}, the Linke turbidity coefficient at air mass 2, which represents the number of clean and dry atmospheres that would

result in the actual solar radiation extinction. In this model, m' is calculated with h_{0ref}, the solar elevation angle corrected by the atmospheric refraction. The diffuse irradiance is calculated empirically using T_{RD}, the diffuse transmission function at zenith, which is a quadratic function of T_{LK2}; and the diffuse angular function F_D, a nested quadratic function of T_{LK2} and h_0 (25)

$$R_{S\downarrow DIR\,clear} = R_{S,TOA\downarrow} \exp(-0.8662 m' \delta_R T_{LK2}) \tag{24}$$

$$R_{S\downarrow DIF\,clear} = \frac{R_{S,TOA\downarrow}}{\sin h_0} T_{RD} F_D \tag{25}$$

Since Rigollier et al. (2000) do not define the T_{LK2} formulation, two approaches by the authors Ineichen, (2008b) and Remund et al. (2003) were analysed. The first one was developed by fitting the results from the radiative transfer model SOLIS; the range analysed by the author was: $0 \leq \tau_{550} \leq 0.6$, $0.2\text{cm} \leq w \leq 10\text{cm}$, up to 7km of elevation and urban aerosol type. The second formula was developed according to SPECTRAL2 model, the results were compared to ground and gridded measurements of T_{LK2}; the equation was developed considering $\alpha = 1.3$, $0 \leq \beta \leq 0.26$, $0.5 \leq w \leq 6\text{cm}$.

6.1.5. Ineichen Model (IN08)

Also based in SOLIS, Ineichen (2008a) proposed a simplified model in which the global solar irradiance and its components are estimated in modified forms of the Beer-Lambert law. The author acknowledges this law is only valid for monochromatic radiation, but he believes the adapted versions are good approximations. In the equations for the direct (26), diffuse (27) and global (28) shortwave radiations valid when $h_0 > 0$, τ_{DIR}, τ_{DIF} and $\tau_{S\downarrow}$ are the corresponding optical depths and r, f, s, the fitting parameters. The author added the term T_C as a common modification factor. The fitting for all these variables was performed considering $0 \leq \tau_{700} \leq 0.45$, $0.2 \leq w \leq 10\text{cm}$, up to 7km of elevation, urban aerosol type and constant ozone content (340 Dobson units).

$$R_{S\downarrow DIR\,clear} = R_{S,TOA\downarrow} T_C \exp\left(-\tau_{DIR} / (\sin h_0)^r\right) \tag{26}$$

$$R_{S\downarrow DIF\,clear} = \frac{R_{S,TOA\downarrow}}{\sin h_0} T_C \exp\left(-\tau_{DIF} / (\sin h_0)^f\right) \tag{27}$$

$$R_{S\downarrow clear} = R_{S,TOA\downarrow} T_C \exp\left(-\tau_{S\downarrow} / (\sin h_0)^s\right) \tag{28}$$

6.1.6. REST2 Model

The REST2 is a two-band model developed based on the SMARTS spectral radiation model. Its 5th version is described in Gueymard (2008) and is analysed in this work. The shortwave spectrum is separated at 0.7µm: band 1 covers the UV and visible range, being characterized by high absorption by ozone and strong scattering by aerosol and air molecules; band 2 covers the near infrared where there is strong absorption by water vapour, CO_2 and other gases, but only limited scattering. For each band, the direct beam (29) uses six transmittance factors: T_{Ri}, T_{UMi}, T_{Oi}, T_{Ni}, T_{wi} and T_{Ai} which are related to Rayleigh scattering; uniformly mixed gases (carbon dioxide and oxygen), ozone, nitrogen dioxide, and water vapour absorptances; and aerosol extinction, respectively. Due to the band separation, the solar radiation at TOA is divided between band 1 ($I_{0,f1}$=46.51%) and band 2 ($I_{0,f2}$=51.95%). This model uses individual air masses m_R, m_O, m_w and m_A to describe the solar ray's paths through the atmosphere. The aerosol extinction is modelled according to the Beer-Lambert law (12) and the aerosol optical depth is estimated with the Ångström's law (15) using band specific exponents and an effective wavelength for each band. When there is not enough aerosol information, the exponents can be assumed to be equal, so here $\alpha_1 = \alpha_1 = \alpha$.

The diffuse component for atmospheric scattering and absorption (30) uses a two-layer approach: in the first layer, all the Rayleigh scattering, ozone and mixed gas absorptions occur; in the second layer, aerosol scattering (T_{AS}); water vapour, NO_2 and aerosol absorptions happen. The function *Fi* was added to compensate for multiple scattering effects. B_{Ri}, represent forward scattering fractions for Rayleigh extinction. Unlike the other models, here the ratio of the forward-scattered irradiance to the total scattered irradiance (B_a) is calculated as a function of the solar elevation angle. For the global radiation, the model also considers the effect of the sky and ground albedos.

$$R_{S\downarrow DIR_{clear_i}} = R_{S,TOA\downarrow} I_{0,f_i} T_{R_i} T_{UM_i} T_{O_i} T_{N_i} T_{w_i} T_{A_i} \quad (29)$$

$$R_{S\downarrow AS_{clear_i}} = R_{S,TOA\downarrow} I_{0,f_i} T_{O_i} T_{UM_i} T'_{N_i} T'_{w_i} \left(B_{R_i} \left(1 - T_{R_i}\right) {T_{A_i}}^{0.25} + B_a F_i T_{R_i} \left(1 - {T_{AS_i}}^{0.25}\right) \right) \quad (30)$$

The fitting was performed for the input ranges $300 \leq p \leq 1100$hPa; $0 \leq O_3 \leq 0.6$cm; $0 \leq NO_2 \leq 0.03$cm; $0 \leq w \leq 10$ cm; $0 \leq \alpha \leq 2.5$; and $0 \leq \beta \leq 1.1$. In this work, following the author recommendations, the single-scattering albedo for band 1 was fixed 0.92 and the one for band 2 at 0.84. The nitrogen dioxide amount was set as 0.0002 atm-cm. The ground albedo was the same for the two bands.

6.1.7. Dai and Fang Model (DF14)

In the model proposed by Dai and Fang (2014), the coefficients were fitted to one year of ground data from a single station in Colorado, US. The direct radiation formula (31) is like Bird's model, but it only uses three transmission factors: T_R, T_w and T_A which account for Rayleigh scattering, water vapour absorption and aerosol extinction, respectively. These three terms are based on the Beer-Lambert law (12). The diffusion part (32) considers the top of atmosphere irradiance that does not reach the ground directly is modified by a transmission factor, T_{DIF}, which depends on the solar elevation angle, atmospheric water and aerosol contents. Even though the model was locally calibrated, it was validated using the results from the reference code SMARTS which extended its applicability.

$$R_{S\downarrow DIR_{clear}} = R_{S,TOA\downarrow} T_R T_w T_A \quad (31)$$

$$R_{S\downarrow DIF_{clear}} = T_{DIF} \left(R_{S,TOA\downarrow} - R_{S,DIR\downarrow_{clear}} \right) \quad (32)$$

The model originally calculates the water path (w) with a locally fitted equation that relates it to screen level air temperature and relative humidity. In this work, the water path was entered directly as an input. The model was not developed for situations in which RH > 90% or $\tau_{550} > 0.5$.

6.2. Longwave Downwelling Methods

In the longwave downwelling ($R_{L\downarrow}$) models, the water content of the atmosphere is represented either as vapour pressure (e_0) or as water path (w). When necessary, the water path was calculated following (Prata, 1996) formulation (Appendix A: formulas) which assumes the US standard atmosphere's rate of change of temperature and moisture with height.

In the algorithms that calculate the longwave radiation under cloudy conditions, clouds are mostly represented in two ways: either as cloud fraction (c_f) or as cloud modification factor (c_{mf}) (11). The clear sky solar radiation was calculated from the best $R_{S,\downarrow clear}$ model. As in (Crawford & Duchon, 1999), the values were clipped between 0.0 and 1.0 to be physically realistic.

The formulations for the 11 models analysed in this work are summarized in Table 6-1. In this table, the coefficients displayed in grey correspond to the values stated in the original papers, except Maykut and Church (1973). The first three models can be used to calculate clear sky longwave downwelling radiation $R_{L\downarrow clear}$ while the others can be used for every sky condition.

Some cloud correction algorithms require an estimate of the clear-sky emissivity (ϵ_{clear}). In this work, the three clear sky models were tested with these algorithms. ϵ_{clear} was calculated by isolating it in the Stefan Boltzmann law (6).Th e revised Zhou and Cess model (ZC07) has its own formulation for $R_{L\downarrow clear}$ (43), which is also analysed here. The models from Table 6-1 are described in the next sub-sections.

Table 6-1 - Longwave downwelling parameterisations

BT75	$R_{L\downarrow clear} = 1.24\left(\frac{e_0}{T_a}\right)^{1/7}\sigma {T_a}^4$	(33)
PT96	$R_{L\downarrow clear} = \left(1-(1+w)\exp\left(-(1.2+3.0w)^{1/2}\right)\right)\sigma {T_a}^4$	(34)
DB98	$R_{L\downarrow clear} = 59.38 + 113.7\left({T_a}/{273.16}\right)^6 + 96.96\left({w}/{2.5}\right)^{1/2}$	(35)
AB12	$R_{L\downarrow} = 3.1e_0 + 2.48T_a - 522.5$	(36)
FAO56	$R_{L_{daily}} = \sigma\left(\frac{{T_{a,max}}^4 + {T_{a,min}}^4}{2}\right)\left(0.34-0.14\left(\frac{e_0}{10}\right)^{1/2}\right)\left(1.35\left(1-c_{mf}\right)-0.35\right)$	(37)
MK73	$R_{L\downarrow} = \left(1+0.22{c_f}^{2.75}\right)\epsilon_{clear}\,\sigma {T_a}^4$	(38)
CD99	$R_{L\downarrow} = \left(c_{mf}+\left(1-c_{mf}\right)\epsilon_{clear}\right)\sigma {T_a}^4$	(39)
KB82	$R_{L\downarrow} = R_{L\downarrow clear} + \tau_8\sigma\sum_{i=1}^{4} c_{f_i} f_{8_i}\epsilon_{clouds_i}{T_c}_i^4$	(40)
SC86	$R_{L\downarrow} = \left(\epsilon_{clear}+(1-\epsilon_{clear})c_f\epsilon_{clouds}\exp\left(\frac{T_c-T_a}{46}\right)\right)\sigma {T_a}^4$	(41)
DK00	$R_{L\downarrow} = R_{L\downarrow clear} + (1-\epsilon_{clear})\epsilon_{clouds}c_f\sigma {T_c}^4$	(42)
ZC07	$R_{L\downarrow} = \left(1-c_f\right)R_{L\downarrow clear} + c_f R_{L\downarrow clouds}$	(43)
	$R_{L\downarrow clear} = 37.687 + 0.474R_{L\uparrow} + 94.190\ln(1+w) - 4.935\ln^2(1+w)$	(44)
	$R_{L\downarrow clouds} = 60.349 + 0.480R_{L\uparrow} + 127.956\ln(1+w) - 29.794\ln^2(1+w) + 1.626\ln(1+w_{cw}) + 0.535\ln(1+w_{ci})$	(45)

6.2.1. Brutsaert Model (BT75)

Brutsaert (1975) developed a physically based model from the solution of a radiative transfer equation through simplifying assumptions. The coefficients of Equation (33) were obtained using the US standard atmosphere's rate of change of temperature and moisture with height. The author stated his model could be easily modified to reflect changes in atmospheric conditions, although the value 1.24 appears to work well for most conditions. In his work, Brutsaert (1975) does not compare the model with ground truth data; he only checks how it behaves when compared to different calibrations of the Brunt (1932) approach.

6.2.2. Prata Model (PT96)

Prata (1996) developed his clear sky model based on theoretical considerations and previous models of Ångström (1915), Brunt (1932), and Brutsaert (1975). The author tried representing the absorption by the main gases in the thermal spectral region: water vapour, carbon dioxide and ozone. Since he was looking for an easy to use expression, he disregarded the variations in the latter two, fixing their contribution to the longwave radiation. Equation (34) was theorised as a modification from the Beer-Lambert formulation (12) to include the effect of other atmospheric gases under low water vapour contents. The coefficients of the model were determined as in Brutsaert (1975) considering the US standard atmosphere's water vapour and temperature lapse rates. Using the radiative-transfer model LOWTRAN for a broad range of atmospheric profiles, Prata (1996) extensively tested his model. The author stated it behaves well in many conditions, though on polar regions its performance remained a concern.

6.2.3. Dilley and O'Brien Model (BD98)

Due to the increasing availability of precipitable water data, Dilley and O'Brien (1998) decided to revisit some of the most popular parametric longwave models of the time. Their clear sky B model (35) is a slight modification of the one proposed by Swinbank (1963) who claimed the longwave radiation was better represented by the screen air temperature alone than combined with the near-surface vapour pressure. The authors derived their formula by introducing a grey-body optical thickness, which accounted for the emission of both water vapour and CO_2, in the Beer-Lambert approach and expanded this new variable to a power series. The coefficients were computed using a nonlinear least square fit of LOWTRAN results for a broad range of atmospheric profiles. Dilley and O'Brien (1998) used the same dataset to evaluate the quality of their model, which performed well for cloud-free skies except for strong inversions. The authors highlighted the importance of accurate screen temperature and water path data.

6.2.4. Abramowitz Model (AB12)

Abramowitz et al. (2012) used a robust empirical approach to create their all-sky longwave model. Their calibration consisted of clustering T_a, e_0 and ϕ_k data from 10 high-quality ground stations spread around the globe and then training multiple linear regressions to calculate $R_{L\downarrow}$. The data were obtained between 1997 and 2006, organised so that the training and testing dataset was always different. The authors concluded the most practical and accurate approach was a linear regression against T_a and e_0, without any cloud input. The authors acknowledge formula (36) is quite controversial, yet they say it is well supported by their robust procedure and high-quality experimental data which covered many different climates. Three of the ten stations studied by the authors are also analysed in this study: BON, CAB, GWN.

6.2.5. FAO 56 Model (FAO56)

A reference for the agriculture community, the longwave approach recommended by the FAO (Allen et al., 1998) is a modification of Brunt (1932) model. They consider the cloud contribution and the water content, while all other longwave absorbers are assumed constant (37). It is advised to calibrate the coefficients when local measurements of $R_{L\downarrow}$ are available.

6.2.6. Modified Maykut and Church Model (MK73)

Using hourly data from one station in Alaska between 1962 and 1965, Maykut and Church (1973) developed a model to estimate longwave radiation under cloudy skies in the form:

$$R_{L\downarrow} = \left(0.7855 + 0.000312{c_f}^{2.75}\right) \sigma {T_a}^4 \tag{46}$$

where c_f is the cloudiness in tenths, curiously, this model is different from the form (38) presented in the validation literature (Choi, 2013; Choi et al., 2008; Duarte et al., 2006; Flerchinger et al., 2009; Shunlin Liang et al., 2013; Niemelä et al., 2001). None of these authors stated there was a modification from the original method (46). Some papers also use c_f as the cloudiness in tenths, while the others two simply replace it with the fractional cloud cover. In this work, we consider the modified model (38), where c_f is the fractional cloud cover ($0.0 \leq c_f \leq 1.0$).

6.2.7. Crawford and Duchon Model (CD99)

Crawford and Duchon (1999) developed a simple cloud modification method (39) which requires an estimate of the clear sky emissivity. Equation 39 does not include any coefficients, so there is no need for local calibration. The model was originally elaborated using a calibrated version of the Brutsaert (1975) model for one year of data from the ARM station in Southern Great Plains and tested in other 10 stations. The model was only evaluated during daytime.

6.2.8. Kimball Model (KB82)

Kimball et al. (1982) developed a cloud correction model which assumes the cloud radiation adds to the clear sky estimate and is only transmitted through the atmospheric window between 8-14 µm (40). The model uses the Idso (1981) formulation to calculate the clear sky emissivity and one variation thereof to compute the atmospheric transmissivity in the window (τ_8) as in Equations (47), (48) and (49). Their approach then computes the radiation emitted by each cloud layer (i) as a product of the cloud fraction, emissivity and temperature and the fraction of black body radiation emitted in the 8-14 µm window (f_8) (50) for a maximum of four cloud layers. The authors claim the model is valid for a wide range of climates, but they only used one year of half-hourly ground data from a station in the northern US to validate it.

$$\tau_8 = 1 - \epsilon_8 \tag{47}$$

$$\epsilon_8 = \epsilon_{8_z}(1.4 - 0.4\epsilon_{8_z}) \tag{48}$$

$$\epsilon_{8_z} = 0.24 + 2.98 \times 10^{-6} \left(\frac{e_0}{10}\right)^2 \exp\left(\frac{3000}{T_a}\right) \tag{49}$$

$$f_{8_i} = -0.6732 + 0.006240T_{c_i} - 0.9140 \times 10^{-5}{T_{c_i}}^2 \tag{50}$$

When the model was developed, the cloud variables used were cloud amount and cloud height. The elevation of the cloud was used to estimate its temperature assuming a standard lapse rate. It was also utilized for the cloud emissivity: low clouds had ϵ_{clouds}=1.0 and high thin ones, ϵ_{clouds}=0.5.

In this work, CERES cloud products were used assuming a single cloud layer. CERES doesn't have products related to the cloud emissivity. The cloud visible optical depth product (τ_c) was used to estimate the cloud emissivity based on the Beer-Lambert law (12) as in equation (51), with a=*1.0* and b=*1.0*.

$$\epsilon_{clouds} = a - \exp(-b \times \tau_c) \tag{51}$$

6.2.9. Schmetz Model (SC86)

P. Schmetz et al. (1986) developed one of the first models that use satellite data to retrieve longwave downwelling radiation. They split the all-sky $R_{L\downarrow}$ into a clear sky and a cloud contribution (41). In the original paper, the clear sky emissivity was determined using the equations of Idso (1981) for lower temperatures and Idso and Jackson (1969) for higher ones. The temperature data in different pressure levels, which was used in the clear sky models and to estimate the lapse rate, was obtained from a meteorological analysis grid with a 60km resolution. Back in 1986, no reliable humidity (RH) fields and cloud products for cloud base

temperature (T_c) and emissivity (ϵ_{clouds}) were available. The *RH* was then fixed at 85.5%. The cloud products instead were derived from look-up tables based on Meteosat-2 radiances in the visible and near infrared in a 25 km resolution, and on the temperatures. Since the model used visible channels of the geostationary satellite, it was limited to daytime. The performance of their approach was first assessed using only conventional ground data and then using remote sensing data for two moments near midday in four stations in western Germany. In their analysis, P. Schmetz et al. (1986) found a systematic error in case of small cloud fraction.

In this work, CERES cloud products were used. Its temperature was used directly, assuming it represented the one of the cloud base. To represent a range similar to the one of P. Schmetz et al. (1986) ($0.42 \leq \epsilon_{clouds} \leq 1.0$), the coefficients $a=1.0$ and $b=0.5$ were adopted in Equation (51). The values of ϵ_{cloud} ranged from 0.39 to 1.0, with an average of 0.84.

6.2.10. Diak Model (DK00)

Diak et al. (2000) developed a parameterised model that could be easily operated with geostationary satellite cloud products. Equation (42) was developed as a variation of the Montieth and Unsworth (1990) model. It was derived with a detailed radiative transfer model assuming one cloud layer at various pressure levels. For the simulations, the authors set the cloud temperature T_c as the environmental temperature at that pressure. The algorithm was tested using Prata (1996) clear sky formulation for half hourly ground data from two close-by ground stations in the northern US and 30km-hourly cloud products from GOES: cloud top temperature and effective cloud fraction, defined as times the cloud infrared emissivity. The authors acknowledge the issue imposed by satellite measurements of clouds, as the characteristics of the cloud base are more significant than the ones of the top. However, they state it is hard to evaluate the significance of this problem due to the extreme variability of the clouds.

In this work, the cloud products from CERES are used assuming one single cloud layer using the same approach as described above. Since Diak et al. (2000) algorithm was tested assuming effective cloud fraction equal to one, here the coefficients $a=1.0$ and $b=1.0$ were adopted for Equation (51).

6.2.11. Zhou and Cess Model (ZC07)

Yaping Zhou et al. (2007) improved the Yaping Zhou and Cess (2001) algorithm which was based on extensive radiative transfer modelling. The previous model (52) expresses the longwave radiation as a function of the upwelling longwave radiation ($R_{L\uparrow}$), which was computed using to the Stefan-Boltzmann law (6) considering screen air temperature at 2m and emissivity equal to unity, column precipitable water vapour (w) and cloud liquid water path (w_{cw}). The coefficients *a, b, c, d* and *e* were calibrated using data from the ARM station in the Southern Great Plains. Despite the calibration for only one station, the model performed well for many geographic locations. However, systematic errors were found in cold and dry regions and for areas covered with ice clouds.

$$R_{L\downarrow} = a + bR_{L\uparrow} + c\ln(w) - d\ln^2(w) + e\ln(w_{cw}) \tag{52}$$

To overcome these issues, the new model (36) studied here considers the ice water path (w_{ci}) and replaces the $ln(w)$ terms with $ln(1+w)$, which corrects for the rapid decrease in the logarithmic function for water paths below 1.0. The input data were obtained from CERES, and this parametrisation is one of the models used in its calculations. Data from 29 high-quality ground stations, including the SURFRAD and the ARM ones, were used to calibrate and test the new version. The training and testing datasets were different, and the period covered was from 2000 to 2005.

7. QUANTITATIVE ASSESSMENT OF METHODS

7.1. Shortwave Downwelling Methods

According to Ruiz-Arias and Gueymard (2018), the most important elements that dictate the atmospheric transmissivity are the aerosol and the water contents. For this reason, a local sensitivity analysis over the range of each input variable was carried out for the models first.

For REST2 model, (RES08) it was necessary to include a correction for the effective wavelength of each band as sometimes it was negative. Effective λ lower than zero happened when the sun elevation angle and α were low, below 1.8 ° and 0.4, respectively. In these cases, the wavelengths were replaced by λ_1=0577µm and λ_2=1.165µm. The values adopted correspond to the mean ones when $0.4<\alpha<0.5$ and $2.0°<h_0<5.0°$.

Figure 7-1 displays the behaviour of the direct and diffuse fluxes as a function of the aerosol optical depth at 550 nm for different solar elevation angles. In this simulation, the other variables were kept as their mean clear-sky values.

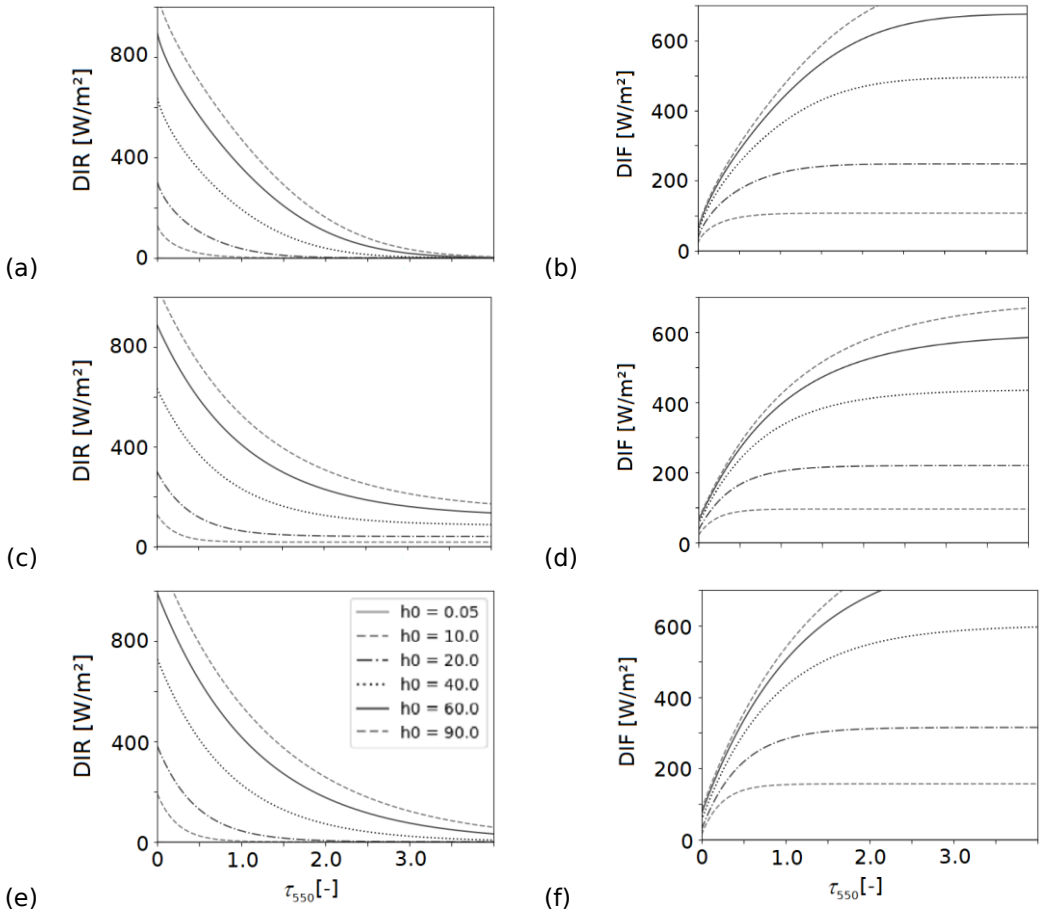

Figure 7-1 – Modelled direct and diffuse solar radiation for models BH81 (a) and (b), IQ83 (c) and (d), MAC87 (e) and (f), EI00 (g) and (h), ER00 (i) and (j), IN08 (k) and (l), RES08 (m) and (n) and DF14 (o) and (p); as a function of the aerosol optical depth for different solar elevation angles [°]

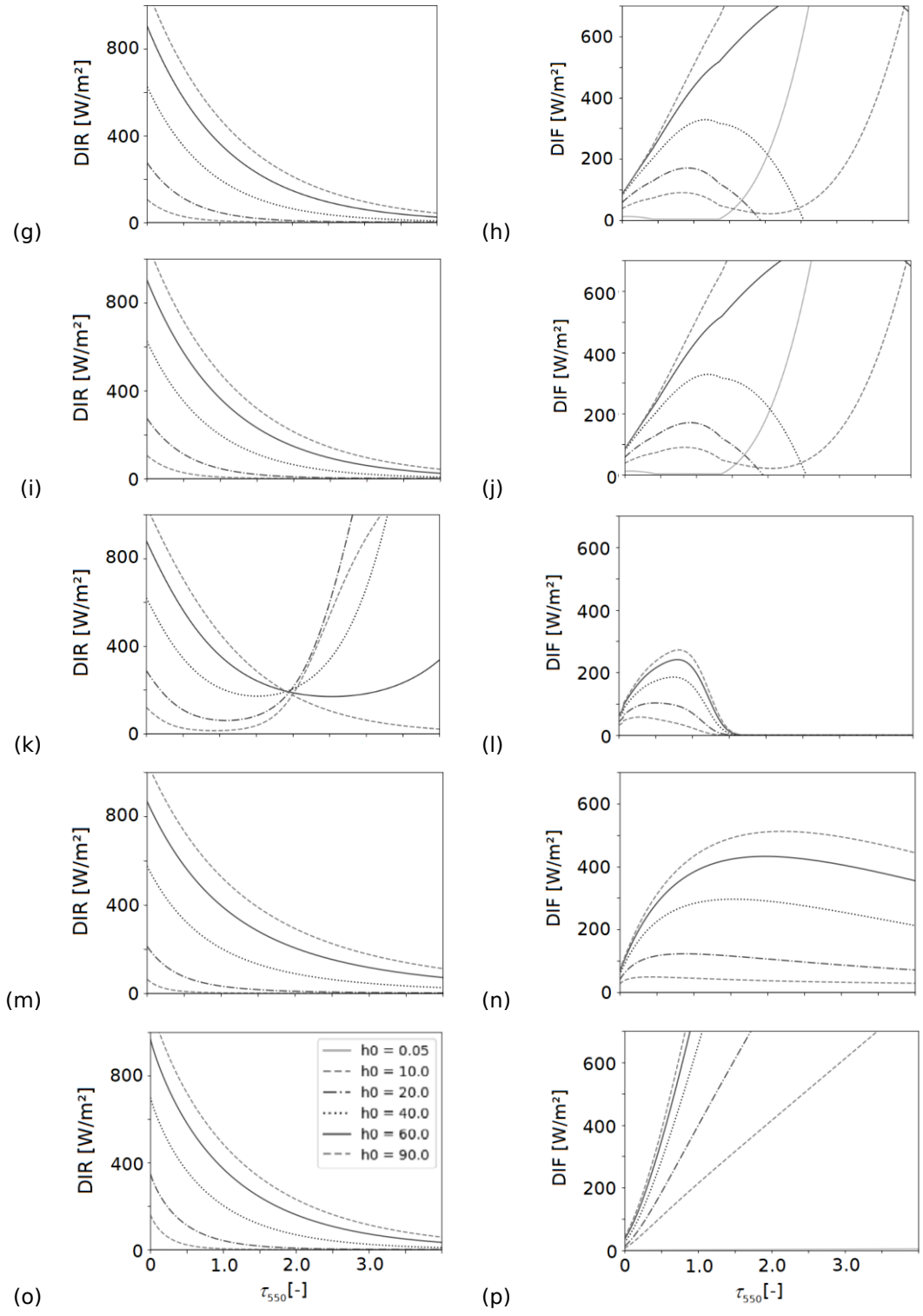

Figure 7-1 (continued)

In the models BH81 (Figure 7-1.a and 7-1.b), IQ83 (Figure 7-1.c and 7-1.d) and MAC87 (Figure 7-1.e and 7-1.f), the behaviours are consistent: as the aerosol load goes up, $R_{S\downarrow DIR}$ decreases and $R_{S\downarrow DIF}$ increases, stabilising at value function of the h_0. IQ83 performs a bit better as all $R_{S\downarrow DIF}$ values are below 700 W/m², which is close to the maximum range of the observed dataset. Similar behaviour is seen in RES08 (Figure 7-1.m and 7-1.n). However, the plateau of the diffuse component is replaced by a slight decrease, which can

be explained by further absorption of aerosols. Therefore, no additional corrections for these models were performed.

EI00 (Figure 7-1.g and 7-1.h), and ER00 (Figure 7-1.i and 7-1.j) behave the same way as the τ_{550} increases. The different approaches for T_{LK2} don't result in big differences. Until $\tau_{550}\approx1.4$, EI00 and ER00 are consistent; however, for $h_0\leq10^o$ or $h_0>40^o$, the diffuse output increases dramatically as τ_{550} goes up. A correction for $R_{S\downarrow DIF}$ was implemented clipping the τ_{550} values above 1.25.

Unlike the previous models, the direct radiation of IN08 (Figure 7-1.k) doesn't continue its decrease as the optical depth raises: at a certain point, the predicted $R_{S\downarrow DIR}$ increases drastically which is physically impossible. For the simulated $R_{S\downarrow DIF}$, the values peak between $\tau_{550}=0.1$ and $\tau_{550}=0.9$ and then decrease, reaching 0.0 just after $\tau_{550}>1.5$. The correction applied here caps the τ_{550} values to 1.1, allowing a gentle decrease in $R_{S\downarrow DIF}$ but preventing the sudden increase in $R_{S\downarrow DIR}$. Furthermore, because all the transmissivities are formulated with the sinus of the solar elevation angle in the denominator, when the value is too low $h_0<0.1^o$, the simulated fluxes are also inconsistent. For that reason, all the fluxes were set to zero in this condition.

In the very simple formulation of DF14, the increase in diffuse radiation with τ_{550} is unlimited, which results in unrealistically high values of $R_{S\downarrow DIF}$ for all tested solar angles (Figure 7-1.p). Since the limit is not clear in the graph, τ_{550} was capped to 0.5, which was the maximum value analysed by the authors.

None of the corrections applied here had a big impact on the performance of the models since 99% of the τ_{550} values of the clear sky dataset are below 0.7. However, these corrections made the models more physically stable, possibly extending their applicability to situations with higher aerosol content.

A similar analysis was carried out with the water content (not shown). The models are much less sensitive to the change in this variable. The diffuse fluxes of BH81, IQ83, MAC87, IN08 and RES08 are roughly constant. EI00 and ER00 increase slightly while DF14 decreases. The $R_{S\downarrow DIR}$ fluxes vary a bit more, declining subtly. All the models are more sensitive to changes in small water contents ($w<0.25$cm). No corrections regarding the atmospheric water content were performed.

After this sensitivity analyses, the models were ran using GEOS inputs for the total column atmospheric water vapour, the aerosol optical depth, Ångström's exponent, sea level and local pressure and compared with the ground measurements of the BSRN network. Table 7-1 contains the statistical indicators RMSE, MBE and R^2 as a function of the major inputs (h_0, τ_{550} and w) for clear sky hourly $R_{S\downarrow}$ fluxes while Table 7-2 gives this indicator separating them per station. The scatter plot of the hourly outputs is displayed in Figure 7-2Figure 7-2 – Scatter plots coloured by density for modelled and measured direct, diffuse and global solar radiation [W/m²] for models BH81 (a), (b),(c), IQ83 (d), (e), (f), MAC87 (g), (h), (i), EI00 (j), (k), (l), ER00 (m), (n) (o), IN08 (p), (q) (r), RES08 (s), (t), (u), and DF14 (v), (w), (x). The ranges of τ_{550} and w in Table 7-1 were defined based on the min, median and max value as well as the 25% and 75% quartiles for clear sky conditions.

The solar radiation at the top of the atmosphere for each hour was calculated considering the mid time step and the BSRN fluxes were averaged during the whole hour. Only day-time hours more than 30 minutes away from sunrise and sunset were included. A total of 6536 hourly points was selected. The number of clear sky points per station varied from 112 (CAB) to 1706 (DRA).

The general tendency for the models is an increasing performance with solar elevation, except for MAC87, which presents larger errors when the sun is above 60º. The variance of the fluxes is better explained by h_0 when the sun elevation angle is at a medium range $30º<h_0<60º$. Between 60º and 90º, $\sin(h_0)$ does not vary much, so the models' response is more dependent on the transmittance and its input parameters.

Table 7-1 – Indicators of hourly clear sky global shortwave downwelling radiation per solar elevation angle, aerosol optical depth and water content

	Solar elevation angle																							
	BH81			**IQ83**			**MAC87**			**EI00**			**ER00**			**IN08**			**RES08**			**DF14**		
h_0 [°]	**RMSE**	**MBE**	**R²**	**RMSE**	**MBE**	**R²**	**RMSE**	**MBE**	**R²**	**RMSE**	**MBE**	**R²**	**RMSE**	**MBE**	**R²**	**RMSE**	**MBE**	**R²**	**RMSE**	**MBE**	**R²**	**RMSE**	**MBE**	**R²**
0.0-15.0	48.8	-44.1	-1.44	40.4	-34.5	-0.68	28.7	19.3	0.15	60.2	-53.8	-2.71	60.2	-53.8	-2.71	51.7	-44.4	-1.74	112.0	-109.6	-11.85	49.0	-40.3	-1.47
15.0-30.0	46.6	-36.4	0.59	35.1	-18.2	0.77	55.8	47.0	0.41	64.1	-48.4	0.22	64.1	-48.4	0.22	59.3	-43.4	0.33	108.2	-101.5	-1.22	51.5	-31.8	0.50
30.0-60.0	34.8	-20.8	0.90	30.4	10.2	0.93	90.9	86.3	0.34	49.9	-29.0	0.80	49.9	-29.0	0.80	48.5	-30.6	0.81	57.8	-41.1	0.73	36.2	-9.1	0.89
60.0-90.0	26.7	-10.9	0.78	38.2	29.4	0.54	116.8	114.1	-3.29	39.4	-15.8	0.51	39.4	-15.8	0.51	39.0	-22.9	0.52	30.2	5.5	0.71	30.5	8.0	0.71
τ_{550} [-]	Aerosol Optical Depth at 550 nm																							
0.0-0.06	25.6	-14.7	0.98	25.7	8.3	0.98	82.1	77.3	0.77	29.3	-11.2	0.97	29.3	-11.2	0.97	25.8	-13.7	0.98	69.2	-56.4	0.84	24.7	3.7	0.98
0.06-0.09	30.3	-16.2	0.97	33.1	13.8	0.97	95.0	88.7	0.75	37.1	-16.1	0.96	37.1	-16.1	0.96	34.8	-20.0	0.97	60.6	-35.5	0.90	31.9	-0.9	0.97
0.09-0.13	35.7	-21.2	0.96	35.4	11.8	0.96	98.1	90.7	0.71	46.7	-29.9	0.93	46.7	-29.9	0.93	46.8	-32.4	0.93	62.6	-33.1	0.88	38.6	-11.0	0.96
0.13-2.06	49.1	-36.2	0.92	38.1	-0.6	0.95	89.9	79.2	0.72	78.8	-65.3	0.79	78.8	-65.3	0.79	75.5	-61.7	0.80	75.7	-47.9	0.80	54.2	-33.5	0.90
w [cm]	Total column atmospheric water vapour																							
0.06-0.63	27.9	-16.9	0.98	27.2	8.1	0.98	82.3	77.1	0.83	36.3	-18.9	0.97	36.3	-18.9	0.97	29.9	-16.7	0.98	68.2	-49.8	0.88	27.2	-2.2	0.98
0.63-1.04	31.7	-18.0	0.97	31.7	11.4	0.97	92.1	85.8	0.77	45.5	-25.2	0.94	45.5	-25.2	0.94	38.2	-22.1	0.96	63.0	-39.1	0.89	32.4	-2.1	0.97
1.04-1.76	37.3	-21.8	0.96	35.6	10.2	0.96	95.5	87.8	0.73	54.1	-30.8	0.91	54.1	-30.8	0.91	49.0	-31.9	0.93	65.1	-37.8	0.88	38.1	-7.3	0.96
1.76-5.24	45.1	-31.0	0.92	37.8	4.0	0.95	95.6	85.8	0.66	64.4	-45.9	0.84	64.4	-45.9	0.84	69.9	-56.0	0.82	72.1	-45.9	0.81	52.5	-29.0	0.90

Table 7-2 – Indicators of hourly clear sky global shortwave downwelling radiation per station

	BH81			**IQ83**			**MAC87**			**EI00**			**ER00**			**IN08**			**RES08**			**DF14**		
	RMSE	**MBE**	**R²**	**RMSE**	**MBE**	**R²**	**RMSE**	**MBE**	**R²**	**RMSE**	**MBE**	**R²**	**RMSE**	**MBE**	**R²**	**RMSE**	**MBE**	**R²**	**RMSE**	**MBE**	**R²**	**RMSE**	**MBE**	**R²**
BON	27.2	-19.6	0.97	23.4	12.2	0.98	95.8	92.7	0.69	52.1	-40.5	0.91	52.1	-40.5	0.91	43.0	-32.2	0.94	56.8	-43.7	0.89	23.8	-8.4	0.98
CAB	38.1	-30.1	0.95	28.4	-3.9	0.97	82.5	74.8	0.76	62.1	-54.0	0.87	62.1	-54.0	0.87	54.8	-47.3	0.90	84.9	-72.3	0.75	42.7	-26.9	0.94
DRA	23.2	-12.7	0.99	28.6	17.8	0.98	92.9	89.0	0.80	28.2	-10.7	0.98	28.2	-10.7	0.98	27.6	-15.6	0.98	48.7	-24.3	0.95	24.7	3.0	0.99
E13	65.4	-48.5	0.82	49.2	-16.8	0.90	81.0	64.8	0.72	74.6	-58.7	0.77	74.6	-58.7	0.77	76.1	-60.0	0.76	93.3	-73.0	0.63	59.9	-36.2	0.85
FPK	24.2	-15.4	0.98	27.5	13.5	0.98	93.9	89.4	0.77	35.7	-25.4	0.97	35.7	-25.4	0.97	30.0	-22.4	0.98	61.2	-43.4	0.90	23.2	-3.3	0.99
GOB	54.2	-38.8	0.94	45.2	-8.8	0.96	87.7	70.6	0.85	78.0	-59.2	0.88	78.0	-59.2	0.88	78.6	-61.5	0.88	95.5	-68.4	0.82	62.6	-34.7	0.92
GWN	20.7	-9.7	0.98	28.9	22.9	0.96	106.1	104.1	0.51	43.5	-29.4	0.92	43.5	-29.4	0.92	35.1	-20.5	0.95	46.5	-35.7	0.91	24.4	2.6	0.97
PSU	28.1	-17.7	0.98	27.0	12.6	0.98	93.8	89.6	0.73	46.0	-33.2	0.93	46.0	-33.2	0.93	37.2	-24.5	0.96	59.6	-45.5	0.89	28.8	-5.8	0.97
SXF	32.8	-23.7	0.97	27.8	4.0	0.98	87.2	80.4	0.82	50.3	-38.3	0.94	50.3	-38.3	0.94	45.0	-34.4	0.95	74.1	-58.2	0.87	34.4	-14.7	0.97
TBL	24.1	-13.7	0.98	27.5	17.5	0.98	90.2	86.9	0.78	27.6	-1.3	0.98	27.6	-1.3	0.98	26.3	-14.4	0.98	40.7	-19.6	0.95	23.6	5.0	0.98
All	**36.0**	**-21.9**	**0.97**	**33.3**	**8.5**	**0.97**	**91.5**	**84.1**	**0.80**	**51.0**	**-30.1**	**0.94**	**51.0**	**-30.1**	**0.94**	**48.9**	**-31.5**	**0.94**	**67.2**	**-43.2**	**0.89**	**38.6**	**-10.1**	**0.96**

The RMSE for all models increases as the aerosol content goes up. In IQ83, the MBE for higher aerosol loads is smaller, but the RMSE is still high, indicating the under and overestimations cancel out. For BH81 and DF14, there is an approximate increase of about 15 W/m² in the RMSE when τ_{550}>0.13, when compared to the previous range. For EI00, ER00 and IN08, the increase of RMSE with aerosol content are nearly twice as large. All these models perform better for lower aerosol amounts. A similar pattern is observed with the water content: as w rises, so does RMSE. Nevertheless, the magnitude of the changes is smaller when compared to τ_{550}.

Comparing the stations (Table 7-2), $R_{S\downarrow}$ is most accurately modelled at TBL and DRA ($RMSE_{mean}$<40.0W/m²) and worst at GOB ($RMSE_{mean}$≈70.0 W/m²),. TBL is the highest station in the study area, which is an indicator that the performance of the models does not deteriorate with altitude. This station and DRA have the lowest median aerosol optical depth (τ_{550} =0.06 and τ_{550} =0.08, respectively), which explains the good model performance at these sites. However, GOB doesn't have an exceptionally high aerosol content that would explain the poorer model performance (Figure 5-1.h). All the models assume aerosol characteristics typical from rural, and in some cases, urban areas. GOB is located near a large sand desert, whose aerosol features are significantly different from the standard ones the models were developed to. Therefore, the performance of the models is highly dependent not only on the aerosol content but also its type.

It can be seen in Figure 7-2 that the models represent $R_{S\downarrow}$ best, followed closely by $R_{S\downarrow DIR}$, while $R_{S\downarrow DIF}$ is poorly characterised, with large scatter. Since the magnitude of the direct solar beam (150<$R_{S\downarrow DIR}$<1200W/m²) is much higher than the diffuse one (25<$R_{S\downarrow DIF}$<275 W/m²) on clear sky hours, the great scatter in the diffuse component is hardly noticed amid the dominant direct radiation flux, and the performance of the models is good on these conditions.

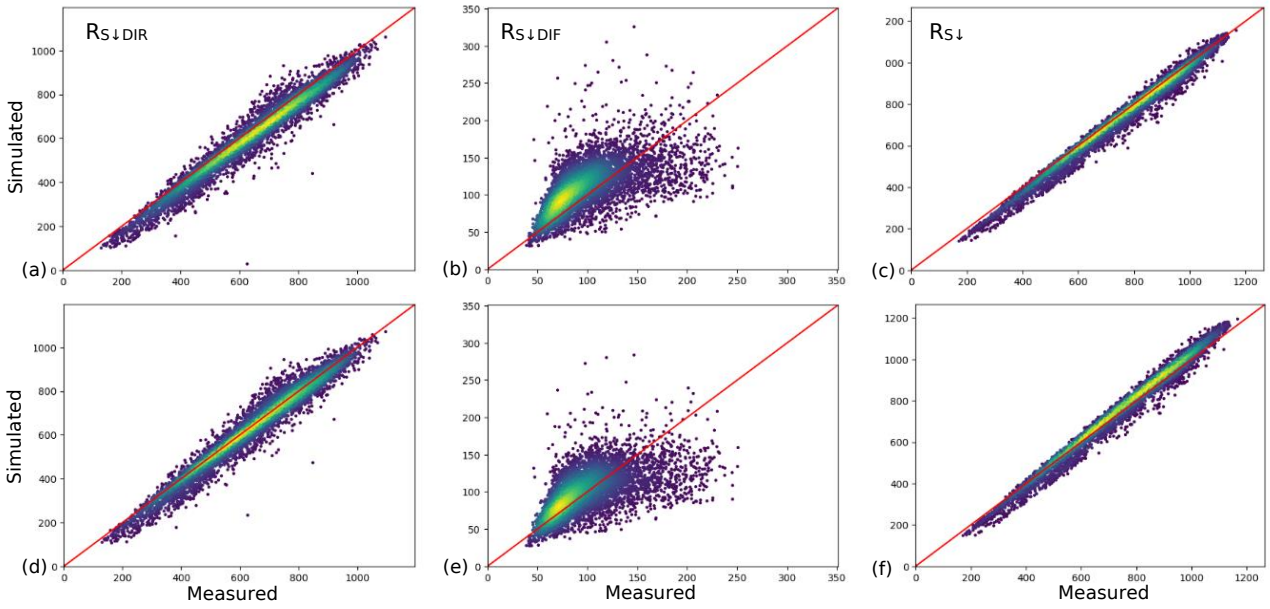

Figure 7-2 – Scatter plots coloured by density for modelled and measured direct, diffuse and global solar radiation [W/m²] for models BH81 (a), (b),(c), IQ83 (d), (e), (f), MAC87 (g), (h), (i), EI00 (j), (k), (l), ER00 (m), (n) (o), IN08 (p), (q) (r), RES08 (s), (t), (u), and DF14 (v), (w), (x)

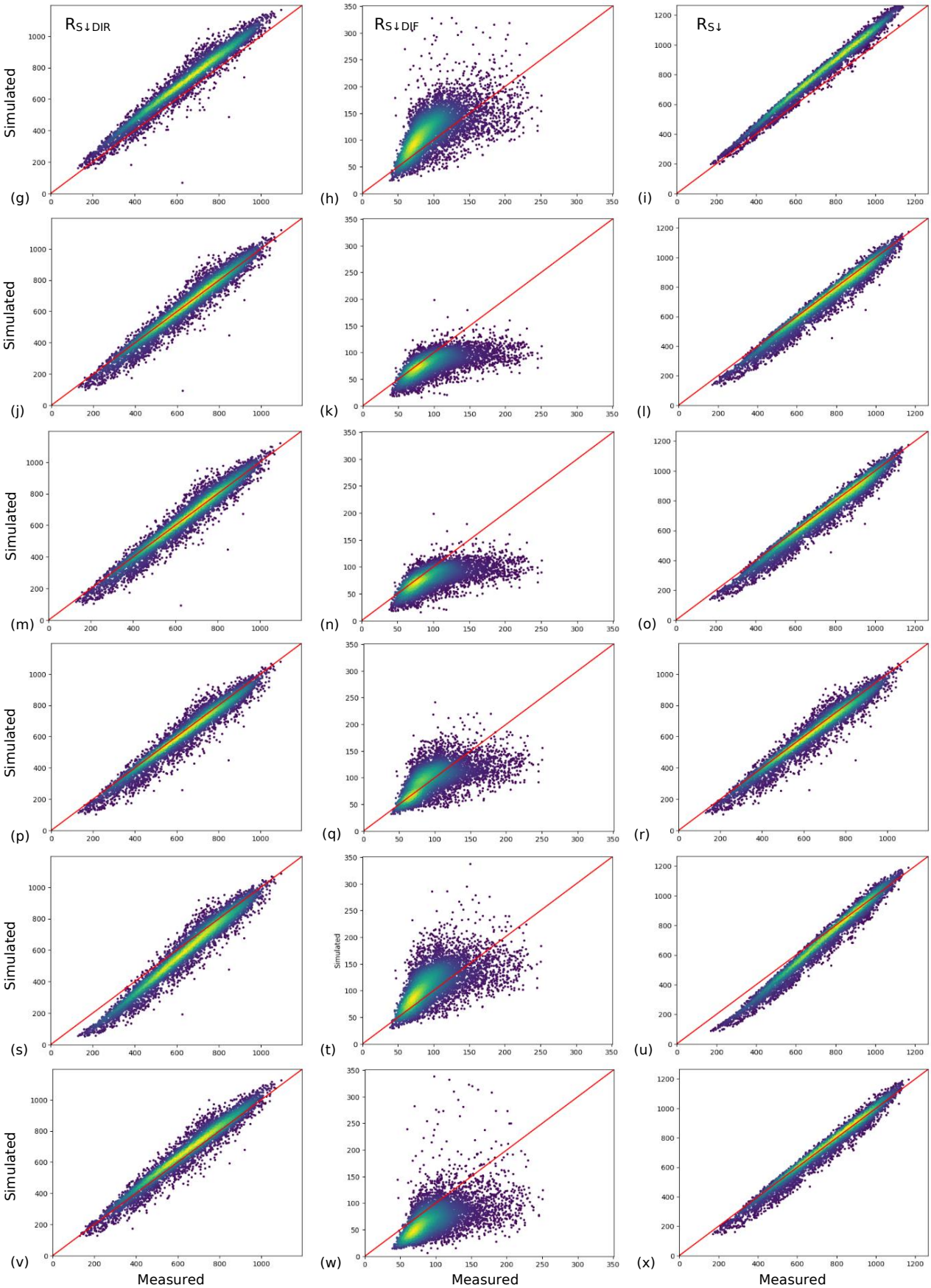

Figure 7-2 (continued)

MAC87 (Figure 7-2.g and Figure 7-2.h) overestimates both the direct and the diffuse components, having the worse performance (RMSE>60 W/m² for all stations in Table 7-2). RES08 performs worse than most models, largely underestimating the direct radiation at lower ranges (Figure 7-2.s) despite its more complex formulation with band separation. EI00, ER00 and IN08 $R_{S\downarrow}$ errors are in the same magnitude (Table 7-2). Even though the ESRA models represent $R_{S\downarrow DIR}$ well, the diffuse radiation is underestimated for larger $R_{S\downarrow DIF}$ (Fig. 7 2.k and Fig. 7 2.n) For smaller $R_{S\downarrow DIF}$ values, IN08 is the model that represents it best (Figure 7-2.q).

The models that perform better are the ones with 5 transmissivity factors (IQ83 and BH81) followed closely by DF14, despite its simpler formulation (Table 7-2). However, it can be seen in Figure 7-2.v and Figure 7-2.w that DF14 overestimates $R_{S\downarrow DIR}$ and underestimates $R_{S\downarrow DIF}$ while BH81 Figure 7-2.a and Figure 7-2.b does the opposite. Therefore IQ83 was judged to be the best model for estimating the global solar radiation (RMSE=33.29W/m² for all stations). Further on, for the range of this dataset, the model behaviour was consistent, and no corrections were required.

In a daily comparison, the same criteria to identify clear days were used for the hourly data. Out of 3650 days, only 287 days were judged cloudless. Due to this limited number, an analysis per station could not be performed: in this classification, CAB, E13 and PSU had less than 10 clear sky days. Table 7-3 thus presents the clear sky daily indicators of each model for all stations combined. Since ER00 and EI00 had similar results, only one of them (EI00) is shown here. Overall, the performance of the models increased in this temporal upscaling, and the RMSE decreased at least 20W/m² for all approaches. It is important to remember the limited number of points of this analysis. Furthermore, over 60% of the points originate from the stations DRA and TBL, which had the best hourly results.

Table 7-3 – Indicators of daily clear sky global shortwave downwelling radiation for all stations

	RMSE	MBE	R²
BH81	7.2	-3.9	0.99
IQ83	10.8	7.9	0.98
MAC87	43.1	41.5	0.72
EI00	12.5	-6.4	0.98
IN08	12.1	-7.6	0.98
RES08	21.1	-18.0	0.93
DF14	8.0	1.3	0.99
GOES/MSG	18.6	-8.9	0.95

Table 7-3 also displays the indicators of the geostationary satellite $R_{S\downarrow}$ products. Despite the large pixel size, the solar radiation estimates from GOES/MSG are more accurate then the models RES08 and MAC87. The performance of the other models is quite similar: BH81, IQ83, EI00, IN08 and DF14 are all able to simulate the daily clear sky solar radiation with RMSE <13W/m², |MBE|<8W/m² and R^2>0.98. This is in the range of the uncertainty of the pyranometers used at the field sites. There is limited scope and need for improvement of the performance of any clear sky parametrization.

As it was the model that best represented also the hourly approaches, IQ83 was also chosen here to represent clear sky days.

7.2. Albedo Methods

The all-sky daily land surface albedos estimated from CERES and MODIS are compared to the one measured in the BSRN network in Figure 7-3. Initially, there were 3450 points for the CERES estimates while MODIS had about half. In Figure 7-3, only the common points are shown.

The albedo from MODIS was estimated combining the black and white surface ρ_g using the diffuse fraction from CERES. The main difference between the two graphs is then the spatial scale: the CERES product used here is at 1° while MODIS is much smaller, 500m. Both are still much larger than the area covered by a pyranometer in ground networks, which is smaller than 20m for the instruments placed at 10m and even smaller for the devices installed in lower points.

Since most values are clustered around 0.2 in Figure 7-3, the averages and standard deviations of each estimate were compared and are shown in Table 7-4. Due to the spatial mismatch, CERES presents a higher variability and a higher average, while the ones from MODIS and BSRN are more related.

Table 7-4 – Mean and standard deviation of albedo estimates

	BSRN	MODIS	CERES
Mean	0.198	0.203	0.251
STD	0.096	0.096	0.117

Across the stations, the average MBE of MODIS was 0.00 and, for CERES -0.05. Larger errors ($|MBE| \geq 0.10$) were found for CERES estimates in CAB, PSU and GOB. Considering the mean and the standard deviation values of these stations, errors in this range are not acceptable.

Out of 1750 MODIS ρ_g, 57 have an absolute error higher than 0.15. Nearly 60% of them come from the stations SXF and FPK, the two stations in the US with higher latitude. The other points come from BON, PSU or TBL, and all of them are between November and March. Thus, the most obvious cause of the scatter (Figure 7-3.b) is the intermittent presence of snow cover.

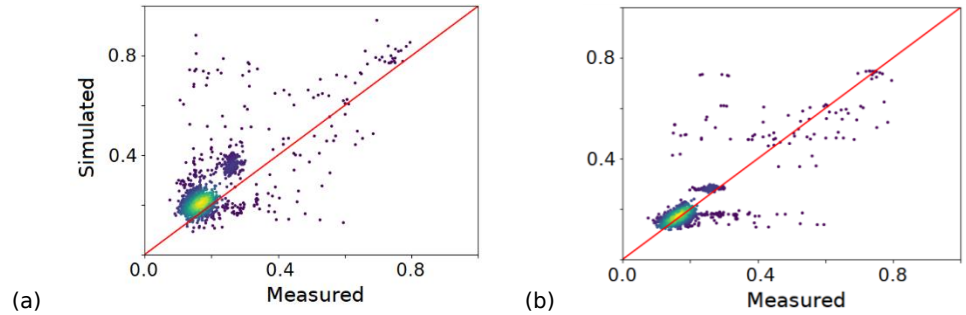

Figure 7-3 – Modelled and measured land surface albedo of CERES (a) and MODIS (b) [-]

7.3. Longwave Downwelling Methods

The longwave downwelling methods were ran using two different inputs for water content and temperature: ground data from the BSRN network; and modelled data from GEOS and CERES. To define the cloud modification factor ($c_{mf}(11)$, the $R_{S\downarrow clear}$ was calculated using IQ83 model. For the ground input, the measured $R_{S\downarrow}$ was used while for modelled, the shortwave flux from CERES. Nighttime values were linearly interpolated. For both input sources, the cloud fractions for cloudy sky corrections were simulated using the CERES c_f as well c_{mf} as an input.

Since there were two input sources to calculate c_{mf}, the number of points classified as clear and cloudy changed accordingly. Table 7-5 illustrates this sorting and shows the relative number of points for each station. Since GEOS data is modelled, it doesn't have the data gaps that are present in the BSRN network. The $R_{S\downarrow}$ flux by CERES is representative of a much larger area, so the clear sky classification is more limited. The stations DRA, FPK and TBL have the largest number of clear sky points while CAB, E13 and SXF have the smallest.

Table 7-5 – Number of clear, cloudy and all-sky points per sky condition and input source and relative contribution by station

	BSRN			GEOS		
	Clear	Cloudy	All	Clear	Cloudy	All
BON	12.0%	9.8%	10.2%	10.9%	9.9%	10.1%
CAB	2.4%	11.4%	9.9%	3.2%	10.7%	9.8%
DRA	17.3%	8.8%	10.3%	16.4%	9.3%	10.2%
E13	4.2%	11.0%	9.8%	5.9%	10.6%	10.0%
FPK	15.3%	9.3%	10.4%	13.9%	9.7%	10.3%
GOB	10.7%	9.8%	9.7%	13.4%	9.5%	9.8%
GWN	11.2%	10.0%	10.2%	10.8%	10.0%	10.1%
PSU	7.0%	11.0%	10.3%	7.1%	10.6%	10.2%
SXF	5.2%	10.1%	9.3%	6.3%	9.8%	9.3%
TBL	14.8%	8.8%	9.8%	12.2%	10.0%	10.3%
Total	**15,124**	**69,442**	**84,001**	**10,716**	**74,682**	**85,055**

7.3.1. Clear Sky Methods

As in the shortwave analysis, the clear sky longwave models were first tested considering the range of inputs in the dataset. Figure 7-4 shows the resulting emissivity (ϵ_{clear}) for this simulation as a function of temperature for varying water contents.

In general, the emissivity goes down with decreasing water content (w or e_0) and increasing temperature (T_a). PT96 (Figure 7-4.b) does not include T_a in his ϵ_{clear} formulation (34), so his model behaves a little differently. BT75 (Figure 7-4.a) model operates similarly as PT96. However this model has T_a as an input (34) and shows a slight decrease. Further, it is much more sensible to the changes in e_0 than PT96. BT75 ϵ_{clear} are quite low for e_0=0.15.

For these two physically based parameterised methods, the ϵ_{clear} values are always below unity, as they should be. Emissivity values equal to one would mean the sky is emitting radiation as a black body, which is not realistic. However, since the longwave contribution originates from the whole atmospheric column and the methods use the 2 m air temperature as a proxy, the values of $\epsilon_{clear} \geq 1.0$ observed in DB98 (Figure 7-4.c), ZC07$_{clear}$ (Figure 7-4.d) and AB12 (Figure 7-4.e) are possible.

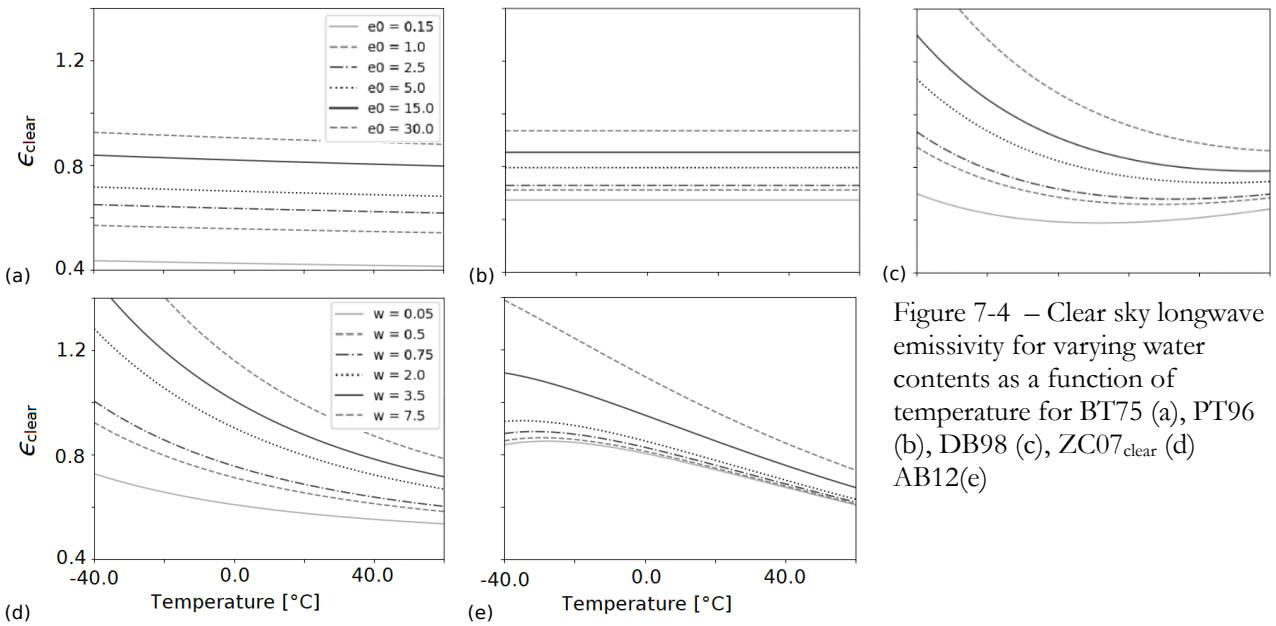

Figure 7-4 – Clear sky longwave emissivity for varying water contents as a function of temperature for BT75 (a), PT96 (b), DB98 (c), ZC07$_{clear}$ (d) AB12(e)

The clear sky models were then run using the different inputs, and their outputs were compared to the ground fluxes. Table 7-6 contains the statistical indicators RMSE, MBE and R^2 as a function of T_a and w for the hourly simulation with BSRN data and Table 7-7 shows these performances organised per station. Additionally, Table 7-7 displays the indicators for the simulation using GEOS inputs for all stations. The characteristics of the two inputs are shown in the whisker plots in Figure 7-5, and the outcomes of the runs are illustrated in the scatter plots of Figure 7-6.

Table 7-6 – Indicators of hourly clear sky longwave downwelling radiation models per temperature and water content using ground data

	Temperature														
	BT75			**PT96**			**DB98**			**ZC07$_{clear}$**			**AB12**		
T_a [º]	**RMSE**	**MBE**	**R²**	**RMSE**	**MBE**	**R²**	**RMSE**	**MBE**	**R²**	**RMSE**	**MBE**	**R²**	**RMSE**	**MBE**	**R²**
< -15	51.2	-45.2	-1.52	31.8	-18.9	0.03	31.4	-18.6	0.05	27.7	-12.2	0.26	32.3	20.3	0.00
-15 to 0	44.6	-34.9	-1.01	33.8	-17.7	-0.15	34.4	-20.3	-0.19	29.2	-10.0	0.14	36.2	21.9	-0.32
0 to 15	30.7	-21.2	0.14	25.6	-8.2	0.40	28.4	-17.4	0.26	22.6	-6.6	0.53	33.9	23.3	-0.05
15 to 30	20.8	-15.1	0.62	15.9	-5.7	0.78	26.9	-22.7	0.37	23.0	-16.8	0.54	19.8	9.6	0.66
> -30	35.8	-32.5	-0.67	22.9	-17.4	0.32	44.3	-41.7	-1.56	54.2	-51.6	-2.84	27.3	-20.1	0.03
w [cm]	**Total column atmospheric water vapour**														
0.0 - 0.5	36.8	-29.7	0.45	23.5	-2.6	0.78	25.3	-14.6	0.74	25.2	-12.1	0.74	38.4	30.8	0.40
0.5 - 1.0	32.0	-24.2	0.60	22.7	-8.3	0.80	29.9	-21.4	0.65	30.7	-17.8	0.63	29.5	16.5	0.66
1.0 - 1.5	27.1	-17.7	0.56	23.0	-10.2	0.68	31.1	-23.6	0.42	28.2	-16.0	0.52	24.3	8.4	0.65
1.5 - 2.5	22.5	-13.9	0.56	21.2	-11.6	0.60	30.8	-25.0	0.17	24.0	-12.8	0.50	20.3	3.4	0.64
2.5 - 7.5	24.7	-20.0	-0.15	25.5	-20.9	-0.22	38.2	-35.3	-1.75	25.5	-20.4	-0.23	17.1	-7.9	0.45

The general behaviour of the models is to underestimate the $R_{L\downarrow clear}$ as all MBE are below 0.0 apart from AB12 (Table 7-6). The models tend to perform better when $15<T_a<30$ºC as the errors in this range are the smallest and the R^2 are higher compared to the other ranges. BT75 has very large errors (RMSE>40W/m²) for temperatures below the freezing point. Inaccuracies in the same range can be found in DB98 and ZC07$_{clear}$ for warmer regions (T_a>30ºC), where the clear sky emissivities of these models are smaller (Figure 7-4.c and Figure 7-4.d)

For BT75 and AB12, the errors decrease with increasing water content. In BT75, small humidities yield very low emissivities (Figure 7-4.a). PT96 accuracy doesn't vary much (21.0<RMSE<26.0W/m²) and it has a higher R^2 when compared to similar range in the other models, except for w>2.5cm. In DB98, the opposite of BT75 is seen: as the water content goes up, so do the errors. For higher humidities, RMSE of AB12 gets smaller, and the model changes its behaviour from over- to underestimation. The MBEs for PT96 and DB98 become lower with increasing w, indicating the models' underestimation $R_{L\downarrow clear}$ gets higher.

Looking at differences per station, it is clear that none of the models can accurately model the longwave radiation of CAB (Table 7-7). The highest R^2 are around 0.4 for AB12 and ZC07$_{clear}$. It has the worst determination coefficient when compared to the other stations for all models except for ZC07$_{clear}$ and DB98, whose R^2 for GOB is worse. For these two models, the MBE is also one of the highest for the station in Africa, which is the warmest station in our study area. As seen in Table 7-6, both have problems representing temperatures in higher ranges. FPK is the coldest station in the dataset for clear sky days and has the worse MBE and RMSE for BT75, which performs poorly in negative temperatures (Table 7-6).

Table 7-7 – Indicators of hourly clear sky longwave downwelling radiation models per station

	BT75			PT96			DB98			$ZC07_{clear}$			AB12		
	RMSE	**MBE**	**R^2**	**RMSE**	**MBE**	**R^2**	**RMSE**	**MBE**	**R^2**	**RMSE**	**MBE**	**R^2**	**RMSE**	**MBE**	**R^2**
BON	31.1	-20.0	0.71	25.6	-11.9	0.81	30.1	-20.7	0.73	23.6	-8.6	0.84	27.5	14.5	0.78
CAB	36.2	-22.0	-0.10	33.7	-17.4	0.05	37.2	-26.5	-0.16	27.3	-12.4	0.37	26.7	6.6	0.40
DRA	31.8	-27.1	0.70	19.2	-6.6	0.89	32.6	-25.6	0.68	37.8	-27.5	0.57	31.1	11.7	0.71
E13	34.0	-27.6	0.64	27.8	-19.1	0.76	40.8	-35.5	0.47	35.2	-28.9	0.61	25.2	-3.4	0.80
FPK	38.0	-29.9	0.59	28.2	-16.9	0.77	32.3	-24.5	0.70	25.9	-15.2	0.81	25.4	12.6	0.81
GOB	21.7	-17.7	0.51	12.7	-6.2	0.83	29.7	-26.8	0.09	33.5	-28.3	-0.16	17.2	0.5	0.69
GWN	22.2	-16.3	0.85	19.5	-11.0	0.89	27.3	-21.3	0.78	18.8	-8.1	0.90	23.9	12.1	0.83
PSU	34.7	-23.4	0.57	29.9	-15.2	0.68	34.8	-24.8	0.57	26.7	-12.5	0.75	28.6	10.9	0.71
SXF	26.2	-14.6	0.81	21.8	-4.6	0.87	26.2	-16.5	0.81	21.6	-7.8	0.87	29.7	18.5	0.76
TBL	22.8	-13.5	0.76	18.4	2.9	0.84	20.1	-10.8	0.81	18.9	-5.3	0.83	35.8	29.3	0.40
All	**29.8**	**-21.4**	**0.75**	**22.8**	**-9.1**	**0.85**	**30.2**	**-22.2**	**0.74**	**27.8**	**-15.6**	**0.78**	**28.0**	**13.1**	**0.78**
GEOS	**42.1**	**-37.8**	**0.50**	**26.3**	**-29.7**	**0.80**	**29.0**	**-40.2**	**0.76**	**30.7**	**-29.2**	**0.73**	**27.8**	**-5.9**	**0.78**

Even though DRA is in the driest location, BT75 does not perform worse than at other sites, as one might expect based on the model behaviour for low humidity. The most humid station (GWN) is the best performing one in an average across all models, with smaller RMSE and best R^2: In this station, 75% of the w values for clear sky days are below 2.5 cm in the BSRN dataset, so the decrease in performance seen in PT96, DB98 and $ZC07_{clear}$ when w>2.5cm (Table 7-6) are not observed in Table 7-7.

No overestimations were noticed in PT96 for the ranges analysed in Table 7-6. However, overestimates occur at TBL (Table 7-7), the most elevated station in the study area, showing the model behaviour might be related to altitude. This place also has poor indicators for AB12, with the largest overestimation.

On an average across the stations, PT96 is the best clear sky $R_{L\downarrow}$ model in the study area while DB98 is the worst. In the graphs on the left side of Figure 7-6, it can be seen the points of PT96 (Figure 7-6.c) are more densely concentrated on the 1:1 line, except for bigger $R_{L\downarrow}$ values, where more underestimations occur. Nevertheless, it is important to consider the stations do not have the same number of clear sky points (Table 7-5), so the models that have a better performance in the station with a larger number of points, e.g. TBL, will have a better average. For the same reason, the poor performance of the models in CAB is not translated in the analysis for all stations.

When changing the input dataset from BSRN to GEOS, it is imperative to consider the differences in the distribution of the points, illustrated in Figure 7-5. The biggest differences happen when in w>50%, when GEOS have significantly higher values. Other relevant changes are in the minimum T_a values and the maximum for e_0.

When simulating with GEOS, the BT75 performance decreased significantly, and the underestimation became more pronounced (Figure 7-6.a and Figure 7-6.b). The changes in the minimum air temperature value and vapour pressure are not enough to explain this decrease, which indicates the model is very sensitive to the local conditions.

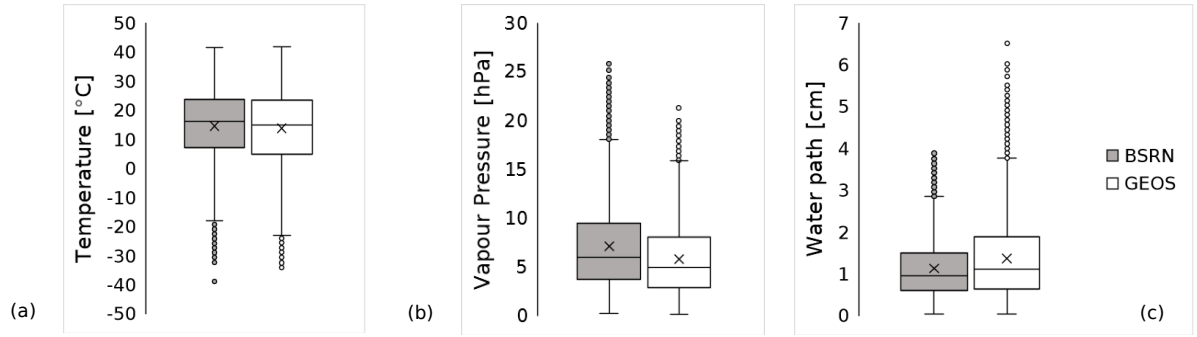

Figure 7-5 – Box plots for temperature (a), vapour pressure (b) and water path (c) for the different input sources (BSRN and GEOS)

In the change of input source, the RMSE of all models except BT75 changed less than 5W/m². There were notable differences in the MBE of $ZC07_{clear}$ and AB12, which got smaller in absolute terms (Table 7-7). Analysing Figure 7-6.g and Figure 7-6.h ($ZC07_{clear}$) it is noticed that more points tend to concentrate on the 1:1 line while overestimations happen in higher ranges, which also have more scatter. This model was sensitive to the change of sources as it has the R^2=-0.23 for w>2.5cm (Table 7-6). In this range, PT96 behaves in the same manner, which justifies the increased scatter in higher ranges (Figure 7-6.b) and the lower general R^2 observed. In the other model that uses water path as an input (DB98), the increased scatter is not seen. The upper part of the graph (Figure 7-6.e) moves up as the model captures better the variations for higher $R_{L\downarrow clear}$ (Figure 7-6.f). In general, the change of inputs for the models that use w as an input dragged the curves closer to the 1:1 line, reduced the underestimation but introduced more scatter in higher ranges.

For both input sources, PT96 had the best indicators. Thus, it was chosen as the clear sky method to represent the longwave radiation in this study. Nevertheless, the model did not represent well the longwave radiation in CAB for the two sources.

7.3.2. All-sky Methods

The cloudy sky corrections algorithms were tested for the temperature range in the dataset for different cloud fractions. The clear sky estimates for this preliminary analysis was carried out with PT96, except for the ZC07 model, which used $ZC07_{clear}$. The other parameters were kept to their average values. Figure 7-7 presents the sky emissivity as a function of temperature for different c_f.

The linear approach by CD99 (Figure 7-7.b) can be easily spotted comparing the curves spacing and the cloud fractions analysed. MK73 (Figure 7-7.a) has an analogous behaviour, however, the cloud contribution only starts appearing after 50% coverage. The general conduct of SC86 (Figure 7-7.c) and DK00 (Figure 7-7.e) is the same. A broader variation is observed in ZC07 (Figure 7-7.f).

As in the clear sky approach, the cloudy sky corrections were then simulated with different input sources. Additionally, three representations of the cloud contribution were tested: c_{mf} estimated by BSRN and by CERES as well as the cloud fraction product of CERES.

The cloudy-sky corrections were tested with the clear sky estimates from BT75, PT96 and DB98 to choose the best possible combination. The motivation for the selection is presented in Table 7-8, which contains the average indicators separated by input sources and cloud representations. These represent only cloudy conditions. For almost all models PT96 yielded the best results with smaller RMSEs and MBEs and higher R^2. DB98 had similar results for CD99, but for a better comparison between the corrections, PT96 was opted to represent $R_{L\downarrow clear}$. From now on, the models were analysed considering only this combination.

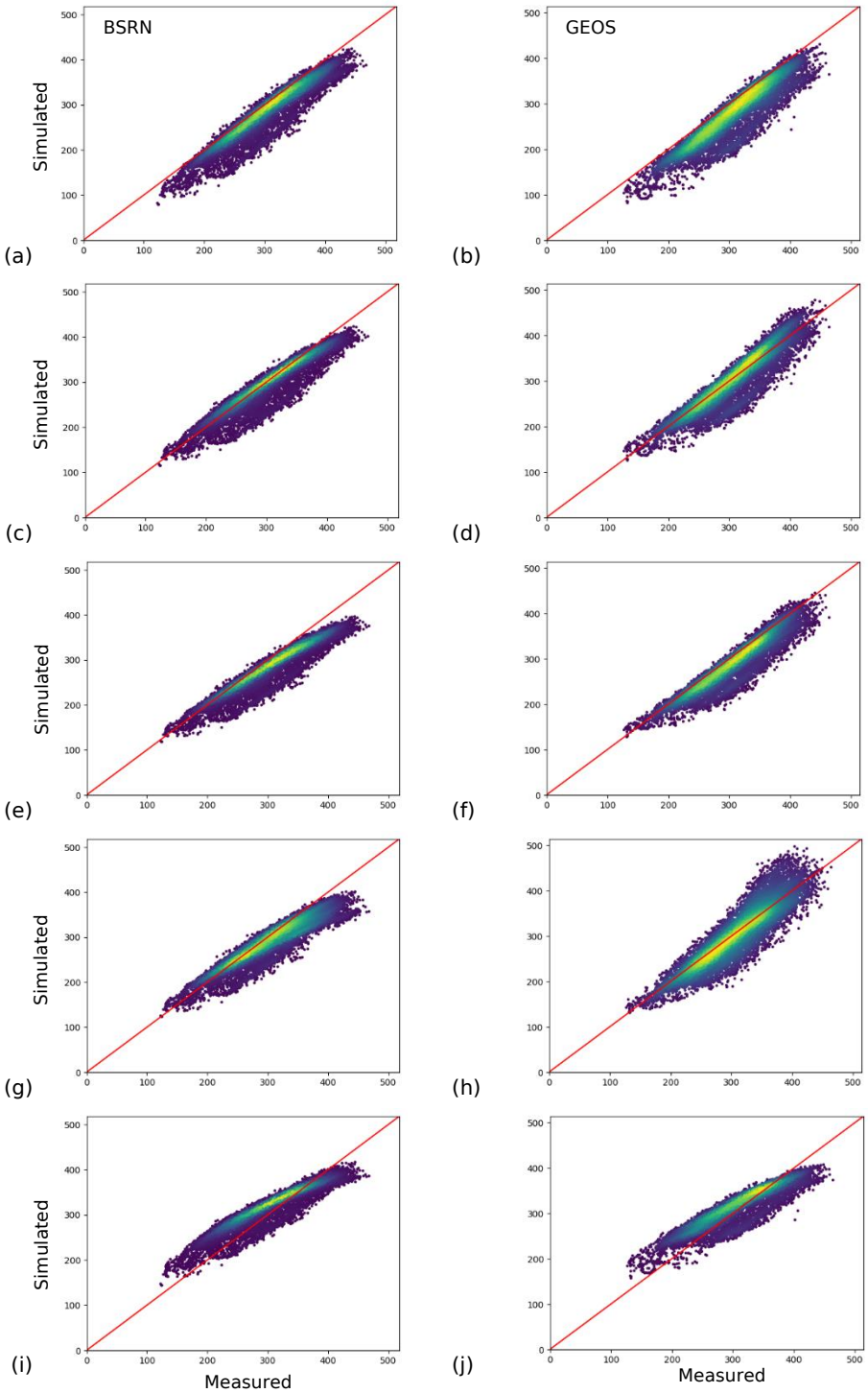

Figure 7-6 – Scatter plots coloured by density for modelled and measured hourly clear sky longwave downwelling radiation for models BT75 (a) and (b), PT96 (c) and (d), DB98 (e) and (f), $ZC07_{clear}$ (g) and (h); and AB12 (i) and (j).

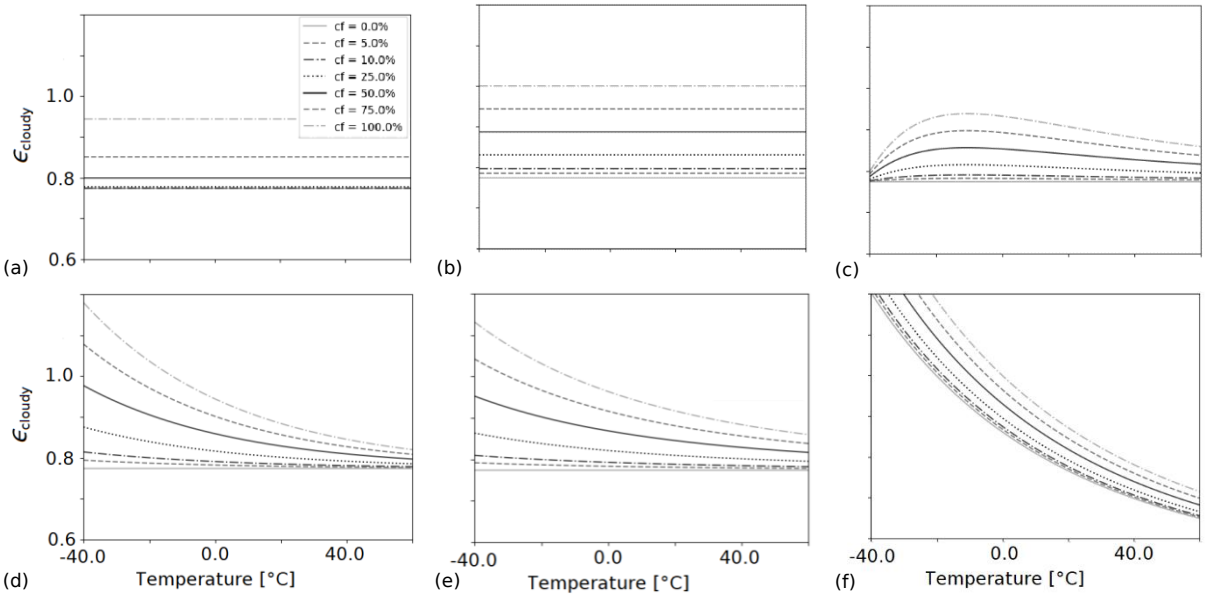

Figure 7-7 – All sky longwave emissivity for varying water contents as a function of temperature for MK73(a), CD99(b), KB82(c), SC86(d), DK00(e) and ZC07(f)

Table 7-8 – Indicators of different combinations of clear sky – cloud correction algorithms for cloudy skies longwave downwelling radiation

	BT75			**PT96**			**DB98**		
	RMSE	**MBE**	**R²**	**RMSE**	**MBE**	**R²**	**RMSE**	**MBE**	**R²**
MK73	37.48	-23.72	0.54	29.5	-6.2	0.72	31.4	-16.5	0.68
KB82	34.09	-20.01	0.63	27.8	-3.5	0.76	28.9	-13.3	0.73
SC86	32.86	-18.72	0.65	26.8	-6.3	0.77	29.1	-14.2	0.73
CD99	34.25	6.81	0.63	33.7	15.0	0.64	33.3	9.4	0.64
DK00	30.40	-11.35	0.70	26.8	-0.2	0.77	27.8	7.4	0.75

The performances of the models were assessed considering the different cloud coverage, which is shown in Table 7-10 (see page 48) These results were produced using BSRN temperature, water inputs and c_{mf} for cloudy sky conditions only. The clear sky methods are also included in the beginning of the table to check how they would perform with increasing cloud coverage (i.e. applying clear sky models to cloudy conditions). The first row (c_f<10%) does not correspond to cloudy conditions but to all sky estimates, as the first ones would be classified as clear skies.

The AB12 method was moved to the end of the table as the authors say it can be used for all conditions. Indeed, when compared to the clear sky methods, it behaves much better keeping RMSE<35.0W/m² while the other approaches the RMSE increases much quicker reaching RMSE values above 50.0W/m² for overcast conditions. Even compared to the cloud correction algorithms, AB12 has similar and in some cases better performance.

Overall, the cloud corrections of MK73, DK00, KB82, SC86 and CD99 were able to improve RMSE and MBE. Even though the relationship between cloud cover and $R_{L\downarrow}$ gets poorer (smaller R²), the errors for overcast conditions remain in a similar range as the ones of clear skies. These methods reduced the RMSE by about 25 W/m² when compared to the pure PT96 approach for c_f>75%.

Below 50% cloud coverage, MK73 hardly improves longwave radiation estimates, which is justified by Table 7-7.a. Under overcast skies (c_f>75%), MK73 outperforms the other models, but between 10-75% c_f, all the other cloud corrections applied to PT96 are better. DK00 has good indicators for c_f>75%, slightly worse than MK73. For all the other sky conditions, DK00 tends to perform best, even though the differences between this approach and the other ones that use cloud temperature (KB82 and SC86) are quite small when c_f<50%.

Although the cloud correction methods applied to PT96 improve the RMSE and MBE, reducing the underestimations, they all tend to increase in absolute terms as they get further from clear sky conditions. CD99 even overestimates the $R_{L\downarrow}$ as the cloud coverage increases.

For overcast skies (c_f>75%), only MK73 and ZC07 show R^2 above 0.6. The latter model has a good behaviour in cloudy conditions, especially when c_f>50%. However, it's important to consider it used the same inputs (CERES) and was calibrated for SURFRAD stations, which compose most of the dataset of this study. Thus, it is mandatory to consider how this method would behave for the other stations, especially for CAB, which presented poorest results in PT96. To illustrate this, Table 7-9 shows the indicator of the cloud correction methods for the stations CAB and GOB, PT96 is included as a reference in the first row. This table was generated using the same inputs as Table 7-10.

Table 7-9 – Indicators of cloud correction algorithms for hourly cloudy skies longwave downwelling radiation for stations CAB and GOB

	CAB			GOB		
	RMSE	MBE	R^2	RMSE	MBE	R^2
PT96	47.2	-38.6	-0.36	29.9	-19.9	0.26
MK73	33.9	-20.2	0.30	23.6	-0.1	0.54
CD99	28.4	3.1	0.51	40.4	25.8	-0.35
KB82	30.7	-15.8	0.43	31.8	14.2	0.17
SC86	30.7	-16.1	0.42	29.8	10.8	0.27
DK00	28.6	-10.4	0.50	34.9	17.9	-0.01
ZC07	25.3	-6.9	0.61	26.7	-8.6	0.41
AB12	28.6	-10.7	0.50	23.1	-3.5	0.56
CERES	21.8	-0.3	0.71	44.0	20.7	-0.62

PT96 performance was significantly improved in CAB for all models. CD99 and DK00 and had the best overall indicators while MK73 yielded the worse. ZC07 had the best overall results for this station when compared to the other methods, showing the applicability of this model to conditions which differ from its calibration.

For GOB, the only method that actually improved the $R_{L\downarrow}$ estimates when compared to the original PT96 approach was MK73. This is quite curious considering this method was initially developed in Alaska. Nevertheless, the calibration environment for the coefficients of the modified model (analysed here) are not known. For this station, ZC07 also showed decent results, with indicators better than all other models, however, it is still the worst station for ZC07 as its clear sky model also fails (Table 7-7).

The performance of the methods for all stations in the different sky conditions, input sources and cloud representations is summarized in Table 7-11 and Figure 7-8 contains the scatter plots of the models using ground data and c_f for cloudy skies. Unlike the clear sky analysis, the contribution for each station for cloudy conditions is similar, so the models' performance is well represented in the average of all stations.

Table 7-10 – Indicators of hourly cloudy sky longwave downwelling radiation models per cloud fraction using ground data

	BT75			DB98			PT96			MK73			CD99			KB82			SC86			DK00			$ZC07_{clear}$			ZC07			AB12		
	RMSE	MBE	R^2	RMSE	MBE	R^2	RMSE	MBE	R^2	RMSE	MBE	R^2	RMSE	MBE	R^2	RMSE	MBE	R^2	RMSE	MBE	R^2	RMSE	MBE	R^2	RMSE	MBE	R^2	RMSE	MBE	R^2	RMSE	MBE	R^2
<10%	27.2	-19.1	0.78	29.5	-22.3	0.74	20.6	-8.1	0.87	20.6	-8.0	0.87	19.3	-3.2	0.89	20.0	-5.6	0.88	19.8	-5.9	0.88	19.9	-5.2	0.89	27.3	-15.8	0.78	26.1	-13.9	0.80	26.8	11.8	0.79
10-25%	35.0	-26.9	0.63	36.6	-29.5	0.60	28.2	-17.5	0.76	27.8	-16.9	0.77	22.9	-1.5	0.84	24.6	-9.0	0.82	24.7	-9.9	0.82	24.0	-7.3	0.83	30.7	-20.3	0.72	26.7	-13.6	0.79	25.2	4.9	0.81
25-50%	43.6	-36.1	0.41	44.7	-38.0	0.38	36.8	-27.5	0.58	33.3	-22.8	0.66	27.0	6.0	0.78	28.4	-10.1	0.75	28.4	-11.4	0.75	27.2	-6.3	0.77	36.3	-27.1	0.59	27.1	-12.6	0.77	26.2	-3.1	0.79
50-75%	56.0	-49.6	-0.12	56.5	-50.7	-0.14	49.6	-42.2	0.12	35.8	-24.2	0.54	31.3	11.9	0.65	32.5	-14.0	0.62	32.0	-14.8	0.63	29.9	-7.2	0.68	45.2	-37.8	0.27	27.7	-13.2	0.73	30.7	-15.7	0.66
>75%	61.8	-56.2	-0.61	62.7	-57.5	-0.66	56.8	-50.3	-0.36	30.9	-6.7	0.60	38.5	22.3	0.37	36.1	-10.5	0.45	35.0	-11.2	0.48	34.4	-1.2	0.50	49.1	-42.6	-0.02	25.9	-8.5	0.72	34.9	-23.1	0.49

Table 7-11 – Indicators of hourly longwave downwelling radiation models for all stations per sky conditions, input sources and cloud representations

			BT75			DB98			PT96			MK73			CD99			KB82			SC86			DK00			$ZC07_{clear}$			ZC07			AB12		
			RMSE	MBE	R^2	RMSE	MBE	R^2	RMSE	MBE	R^2	RMSE	MBE	R^2	RMSE	MBE	R^2	RMSE	MBE	R^2	RMSE	MBE	R^2	RMSE	MBE	R^2	RMSE	MBE	R^2	RMSE	MBE	R^2	RMSE	MBE	R^2
BSRN	*cf*	clear	29.8	-21.4	0.75	30.2	-22.2	0.74	22.8	-9.1	0.85	18.8	0.9	0.90	32.5	17.6	0.70	19.2	3.2	0.90	18.6	2.1	0.90	20.6	6.5	0.88	27.8	-15.6	0.78	23.3	-4.2	0.85	28.0	13.1	0.78
		cloudy	46.5	-37.8	0.31	47.8	-40.2	0.27	40.6	-29.7	0.47	25.8	0.2	0.79	38.3	22.9	0.53	25.7	-3.3	0.79	24.8	-4.7	0.80	25.2	3.0	0.80	38.7	-29.2	0.52	22.2	-5.6	0.84	28.5	-5.9	0.74
		all sky	44.1	-35.0	0.41	45.2	-37.0	0.38	38.1	-26.1	0.56	24.7	0.3	0.81	37.3	22.0	0.58	24.7	-2.2	0.81	23.9	-3.6	0.83	24.5	3.6	0.82	37.0	-26.8	0.58	22.4	-5.3	0.85	28.5	-2.5	0.75
	cmf	clear	29.8	-21.4	0.75	30.2	-22.2	0.74	22.8	-9.1	0.85	23.0	-9.3	0.85	22.0	-6.5	0.86	22.4	-7.7	0.86	22.5	-7.9	0.86	22.3	-7.4	0.86	27.8	-15.6	0.78	27.1	-14.4	0.79	28.0	13.1	0.78
		cloudy	46.5	-37.8	0.31	47.8	-40.2	0.27	40.6	-29.7	0.47	30.8	-17.2	0.70	28.6	6.1	0.74	29.0	-10.6	0.73	28.8	-11.5	0.74	27.7	-6.2	0.76	38.7	-29.2	0.52	27.0	-12.9	0.77	28.5	-5.9	0.74
		all sky	44.1	-35.0	0.41	45.2	-37.0	0.38	38.1	-26.1	0.56	29.6	-15.8	0.73	27.6	3.9	0.77	28.0	-10.1	0.76	27.8	-10.9	0.76	26.8	-6.5	0.78	37.0	-26.8	0.58	27.1	-13.2	0.78	28.5	-2.5	0.75
GEOS	*cf*	clear	42.1	-33.1	0.50	29.0	-19.8	0.76	26.3	-7.3	0.80	21.6	2.6	0.87	29.0	15.6	0.76	21.6	5.1	0.87	20.6	3.0	0.88	21.4	6.7	0.87	30.7	-5.0	0.73	26.3	5.2	0.80	27.8	5.6	0.78
		cloudy	57.5	-49.6	-0.03	41.7	-33.9	0.46	37.2	-24.8	0.57	30.3	4.6	0.71	37.1	21.7	0.57	27.2	3.0	0.77	24.9	-2.2	0.81	25.9	4.6	0.79	34.4	-22.6	0.63	22.6	-1.4	0.84	31.8	-12.9	0.68
		all sky	55.8	-47.6	0.05	40.4	-32.2	0.50	36.1	-22.7	0.60	29.4	4.4	0.74	36.2	21.0	0.60	26.6	3.2	0.78	24.4	-1.6	0.82	25.4	4.8	0.80	33.9	-20.6	0.65	23.0	-0.7	0.84	31.3	-10.6	0.70
	cmf	clear	42.1	-33.1	0.50	29.0	-19.8	0.76	26.3	-7.3	0.80	26.5	-7.5	0.80	25.4	-4.2	0.82	25.8	-5.4	0.81	25.8	-5.8	0.81	25.7	-5.3	0.81	30.7	-5.0	0.73	30.2	-3.6	0.74	27.8	5.6	0.78
		cloudy	57.5	-49.6	-0.03	41.7	-33.9	0.46	37.2	-24.8	0.57	31.2	-12.3	0.70	30.7	9.2	0.70	29.2	-3.2	0.73	28.7	-6.9	0.74	28.5	-2.0	0.75	34.4	-22.6	0.63	25.3	-7.2	0.80	31.8	-12.9	0.68
		all sky	55.8	-47.6	0.05	40.4	-32.2	0.50	36.1	-22.7	0.60	30.7	-11.8	0.71	30.2	7.5	0.72	28.8	-3.5	0.75	28.4	-6.8	0.76	28.2	-2.4	0.76	33.9	-20.6	0.65	25.9	-6.8	0.79	31.3	-10.6	0.70

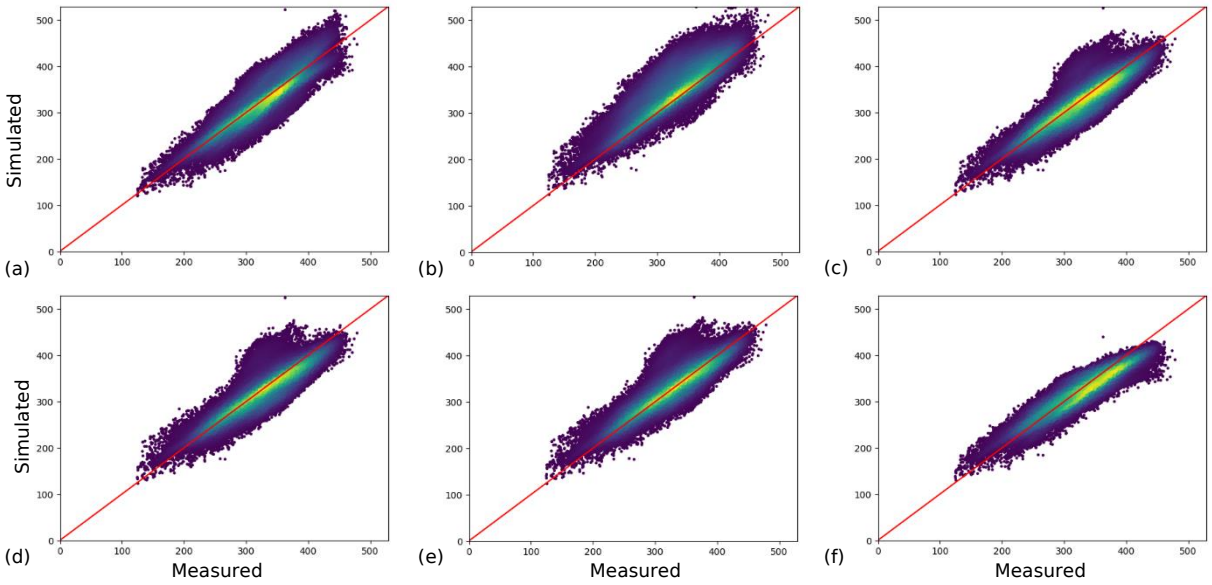

Figure 7-8 – Scatter plots coloured by density for modelled and measured hourly cloudy sky longwave downwelling radiation for models MK73 (a), CD99 (b), KB82 (c), SC86 (d), DK00 (e); and ZC07 (f)

As expected from Table 7-10 and Figure 7-7, the performance of the methods that use cloud temperature as an input (KB82, SC86 and DK00) is quite similar (Figure 7-8.c, Figure 7-8.d and Figure 7-8.e), with points concentrated on the 1:1 line and overestimations concentrated in a specific area in the scatter plot. The models that use exclusively cloud fraction (or cloud modification factor) tend to perform worse than the rest with more scatter. For ZC07, the points are closer to the 1:1 line, however there are underestimations in higher $R_{L\downarrow}$.

The performance of the models is worse when using $\epsilon_{mf,}$ apart from CD99, only model that originally uses it as an input (Table 7-11). The RMSE of the best cloud representation for each model, varied between 22.0 and 30.0W/m², |MBE|<10W/m² and R^2>0.70. ZC07 had the best overall performance followed by DK00. The later failed to represent GOB (Table 7-9), the warmest station in the study area.

The results are similar for all sky conditions considering their best cloud coverage representation. ZC07 was the best model (RMSE=22.4W/m²,MBE=-5.3W/m² and R^2=0.85) followed closely by all the cloud temperature-based models and MK73 (23.0<RMSE<25.0W/m², |MBE|<4W/m² and 0.81≤R^2≤0.83), CD99 had the worse indicators (RMSE=27.6W/m², MBE=3.9W/m², R^2=0.77). However, they are still better than the best clear sky method (PT96 RMSE=38.1W/m², MBE=-26.1W/m² and R^2=0.56), that has large underestimations. For all sky conditions, the all-sky method AB12 had really good results, comparable to CD99 (RMSE=28.5W/m², MBE=-2.5W/m² and R^2=0.75).

The change in input source from ground data to modelled data decreased performance of the models (Table 7-11). These changes were less strong in SC86 and DK00 but more significant in the cloud fraction methods (CD99 and MK73).

7.3.3. Daily All-sky Methods

The results of the temporal upscale of the methods to daily time steps is presented in Figure 7-9 and, for selected ones, Table 7-12. The daily aproach of FAO56 and the CERES longwave product are also included. FAO56 is related to the netlongwave radiation ($R_{L,net}$=$R_{L\uparrow}$-$R_{L\downarrow}$). In these figure and table, CD99 and FAO56 use the local ϵ_{mf} as the cloud factor while the others use cloud fraction from CERES.

Table 7-12 – Indicators of daily all sky longwave downwelling radiation models

	BSRN			GEOS		
	RMSE	MBE	R^2	RMSE	MBE	R^2
PT96	33.7	-26.0	0.59	31.0	-22.7	0.65
MK73	15.7	0.5	0.91	20.5	4.4	0.85
CD99	16.9	4.0	0.90	20.1	7.6	0.85
KB82	16.8	-2.1	0.90	18.2	3.2	0.88
SC86	16.2	-3.5	0.91	16.3	-1.6	0.90
DK00	16.2	3.6	0.91	17.0	4.8	0.90
ZC07	15.9	-5.2	0.91	14.5	-0.7	0.92
AB12	22.5	-2.5	0.82	25.5	-10.5	0.77
FAO56	50.9	-44.8	-1.17	50.5	-43.6	-1.13
CERES	14.1	0.3	0.93	14.3	0.0	0.93

As in the hourly analysis, all cloud correction methos improved the daily estimates of $R_{L\downarrow}$ when compared to the original PT96 approach reducing the RMSE in more than 10W/m² and decreasing significantly the underestimations. All these methods and ZC07 have very similar accuracies, with $14.0<RMSE<21.0 W/m^2$ $|MBE|<8.0 W/m^2$ and $R^2 \geq 0.85$ for the two input sources.

The following additional information can be retrieved from the scatter plots:

- MK73 overestimates higher $R_{L\downarrow}$, in this region, there is also more scatter;
- CD99 overcorrects the cloud forcing in PT96, shifting the whole curve slightly above the 1:1 line;
- The temperature based methods (KB82, SC86 and DK00) perform similarly, the overestimations noticed in the hourly analysis are less pronounced;
- ZC07 performs well with underestimations in higer ranges, as seen in the hourly approach;
- AB12 has small MBE (-2.5W/m²), however the graph shows inclination of the curve of this model away from the the 1:1 line, and the overestimations in lower ranges cancel out with the underestimations of larger $R_{L\downarrow}$;
- An inclination way from the 1:1 line is also noticed in FAO56, which is the worst performing method even considering the added uncertainties related to the $R_{L\uparrow}$ term;
- Despite it's big pixel size, the CERES product fits really well with the 1:1 line.

For MK73 and CD99, the change from locally measured to modelled data as an input decreased the indicators more significantly than the methods based on cloud temperature. Amongst them, the variations of SC86 were the smallest, probably because of the correction term that relates the screen air temperature to the cloud temperature (exponential term in Eq. (41). For ZC07, this change actually improved the model, reducing the underestimations in higher ranges.

Considering the average indicators and the graphs, CERES performs really well. The performance of this model was checked for all stations. GOB was by far the worse represented one. The indicators for this station in all sky conditions for the two input sources of selected methods are shown in Table 7-13 – Indicators of cloud correction algorithms for daily all-sky longwave downwelling radiation for station GOB.

For measured inputs, MK73 and ZC07 improve the $R_{L\uparrow}$ estimates and these are much better than the one from CERES, which is similar to the results of SC86. Interestingly, for modelled inputs, the accuracy of PT96 is better than the one with local estimates and much higher than all cloud correction algorithms and CERES, whose product is still better than all cloud corrections. Since CERES uses GEOS tempetarute inputs, it might mean the cloud representations in that region are not accurate.

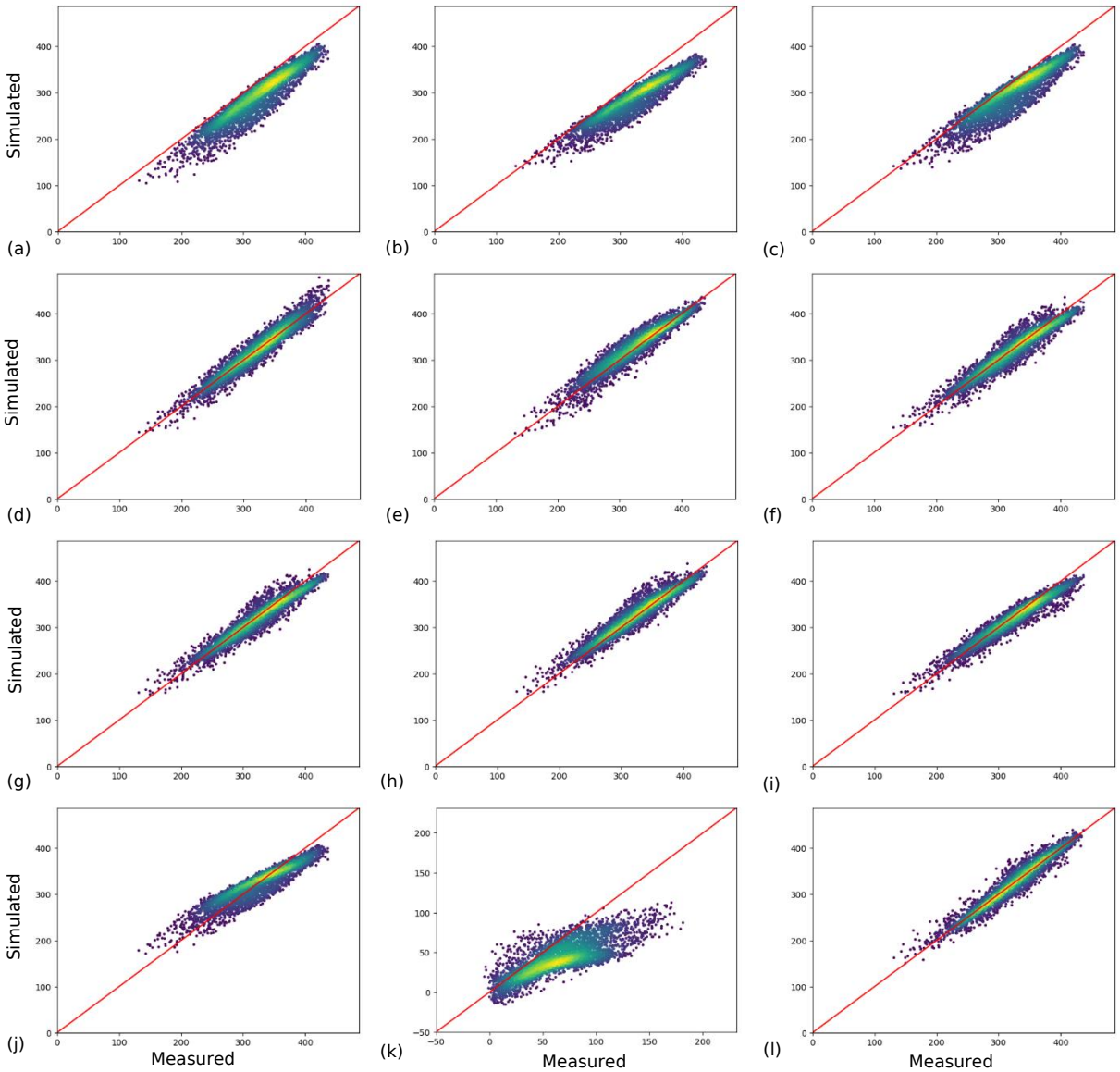

Figure 7-9 – Scatter plots coloured by density for modelled and measured daily all sky longwave downwelling radiation for models BT75(a), DB98(b), PT98 (c), MK73(d), CD99(e), KB82(f), SC86(g), KB00(h), ZC07(i), AB12(j), FAO56(k) and CERES(l)

Table 7-13 – Indicators of cloud correction algorithms for daily all-sky longwave downwelling radiation for station GOB

	BSRN			GEOS		
	RMSE	MBE	R^2	RMSE	MBE	R^2
PT96	21.4	-17.5	0.43	11.6	-2.7	0.83
MK73	15.0	6.9	0.72	27.4	22.3	0.06
CD99	24.2	20.3	0.27	37.3	35.2	-0.75
KB82	25.8	19.3	0.17	39.3	36.2	-0.94
SC86	23.5	15.5	0.31	30.8	27.5	-0.19
DK00	28.9	22.7	-0.03	36.7	33.8	-0.69
ZC07	15.1	-8.0	0.72	23.6	18.0	0.30
AB12	15.9	-3.0	0.68	17.1	-6.3	0.63
FAO56	57.9	-56.6	-11.47	58.2	-56.4	-11.26
CERES	21.9	17.6	0.39	21.9	17.6	0.39

All results considered, when there are local air temperature and water content measurements, the best approaches to calculate $R_{L\uparrow}$ are MK73, ZC07 and SC86. MK73 was ranked first since it the only cloud input it needs is the fraction. When local measurements are not available, CERES product might be used. The application of this product must be made with caution in locations with similar characteristics of GOB.

7.4. Longwave Upwelling Methods

The scatter plot of daily all sky longwave upwelling radiation CERES product is displayed in Figure 7-10.a and the estimate assuming $\epsilon_g \approx 1.0$ and $T_g \approx T_a$ is in Figure 7-10.b. The attempt to spatially downscale CERES product using the temperature ratio is presented inTable 7-14.

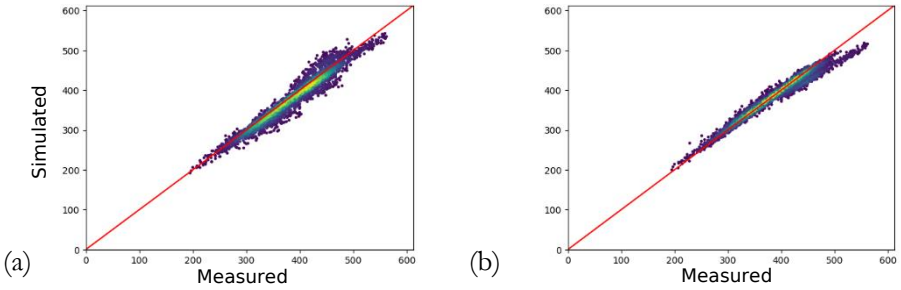

Figure 7-10 – Modelled and measured longwave upwelling radiation of CERES (a) and $\epsilon_g x T_a$ (b)

The two methods to represent $R_{L\uparrow}$ in figure 10 are quite accurate. $\epsilon_g x T_a$ reduces the scatter (R^2=0.96 against R^2=0.92) and gives better overall resuls than the CERES product. For this simplified method, the stations that perform worst are GOB and DRA while all the others have RMSE<15.0W/m², |MBE|<8.0W/m² and $R^2 \geq 0.95$. The first station has more scatter and considerable underestimations (R^2=0.49 and MBE=13.8W/m²) while the second one has highest underestimations and errors overall (MBE=17.6W.m² and RMSE=25.4W/m²). ²). The poorer performance of this simplified approach at GOB and DRA can be linked to the land cover of these stations, which are desert and gravel.

In the CERES product, DRA performs much better, however the indicators of GOB are even worse, confirming poor quality of the the R_L products of CERES in that region. In this station, CERES overestimates instead of underestimating as seen in the $\epsilon_g x T_a$ approach. The indicators are also a bit worse in TBL, the highest station of the region. The attempt to downscale the CERES cloud products improved the indicators of this station and of GOB and, thus, the overall performance of CERES product.

Considering all, the best option to estimate the all-sky longwave upwelling radiation is to simply use the $\epsilon_g x T_a$ approach for places that are not in desert/gravel areas and to downscale CERES products for those.

Table 7-14 – Indicators of daily all-sky longwave upwelling radiation methods

	CERES			CERES x T_{ratio}			ϵ_g x T_a		
	RMSE	MBE	R^2	RMSE	MBE	R^2	RMSE	MBE	R^2
BON	12.69	-7.14	0.94	12.56	-6.74	0.94	5.26	2.41	0.99
CAB	11.64	-7.48	0.87	11.08	-6.78	0.89	4.47	1.58	0.98
DRA	13.97	-9.40	0.96	10.52	-3.83	0.98	25.35	-17.58	0.85
E13	10.77	-7.26	0.96	11.97	-9.41	0.95	8.78	-7.55	0.97
FPK	15.14	-11.34	0.96	14.68	-11.38	0.96	14.36	-5.06	0.96
GOB	21.25	15.40	0.34	19.61	14.25	0.48	19.38	-13.77	0.49
GWN	13.84	-10.78	0.89	14.34	-11.53	0.88	4.31	0.42	0.99
PSU	9.42	-5.44	0.96	8.41	-3.65	0.97	7.07	4.86	0.98
SXF	9.48	-2.97	0.97	9.15	-2.55	0.98	6.18	3.12	0.99
TBL	34.15	-31.60	0.57	30.30	-28.02	0.67	11.61	3.37	0.95
All	**16.85**	**-7.86**	**0.92**	**15.51**	**-7.10**	**0.93**	**12.64**	**-2.80**	**0.96**

7.5. Net Radiation Estimate

In this final section, the net radiation (R_n) was calculated with some of the selected methods in the previous sections. Clear sky conditions were defined based on the CERES products $R_{S\downarrow DIR}$ and $R_{S\downarrow}$ for every hour during daytime to decife if CERES or IQ83 would represent $R_{S\downarrow}$. The all sky $R_{L\downarrow}$ was calculated according to MK73 correction of the PT96 algorithm. For the upwelling components, the simple approach of $\epsilon_g x T_a$ and the products of MODIS were used for the longwave and albedo, respectively. When ρ_g were not available, they were simply replaced by the average albedo of each station. This value served as input for the IQ83 model. Further on, it assumed a standard meteorological station was located nearby, so BSRN data of air temperature and pressure were used; while modelled inputs (GEOS) of total column atmospheric water vapour, sea level pressure and aerosol content were considered. The results of the R_n of the stations BON, FPK and GOB are presented in the time series of Figure 7-11.

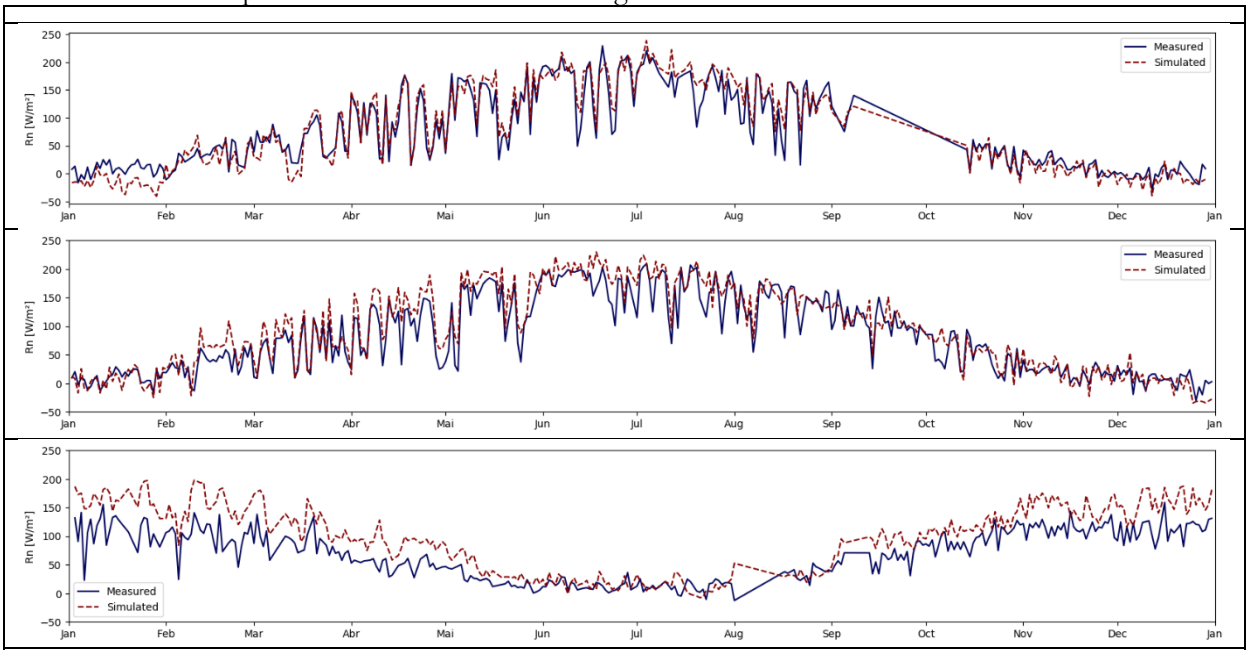

Figure 7-11 – Time series of modelled and measured daily net radiation of SXF(a), BON (b) and GOB(c)

These stations were chosen to illustrate the general performance of the models. SXF was the station that performed best with RMSE=21.35W/m², MBE=-0.61W/m² and R^2=0.90; BON was an mediocre station, with RMSE=24.35W/m², MBE=10.23W/m² and R^2=0.86; while GOB was the worst one (RMSE=38.94W/m², MBE=28.89W/m² and R^2=0.17).

In the first two graphs, it can be seen the simulated flux captures the temporal variations well, as peaks and valleys in the simulations agree with those in the model. However, the magnitude of the variations is not the same. In BON, the longwave downwelling fluxes are not represented as well as in SXF, so the magnitude of the errors is larger. Between January and February in the latter station, the linear interpolation of the albedo product from MODIS doesn't capture all the intermittent snow events. It resulted in larger albedo and thus in a consistent underestimation of the net radiation.

In GOB, the accuracy of the CERES $R_{S\downarrow}$ product is quite low, with a big overestimation (MBE=29.94W/m²), which shifted simulated curve up during the whole year except in the winter. In this station, the longwave fluxes are also not well represented (Table 7-13 – Indicators of cloud correction algorithms for daily all-sky longwave downwelling radiation for station GOBand Table 7-14 – Indicators of daily all-sky longwave upwelling radiation methods). The GEOS water column product as an input pulled the performance of the MK73 model (applied to PT96) down.

8. DISCUSSION

This discussion is organized according to the research questions. The first one was sufficiently explored in the previous chapters. Section 8.1 combines the second and third questions and discusses the performance of the different models to capture the spatiotemporal characteristics of the radiation components and the effects of inaccuracies of the input data and satellite products. In 8.2, a link is built between environmental conditions and performance errors to answer the fourth question. Finally, section 8.3 briefly describes the limitations of this study regarding the limited number of ground stations. In this last section, special attention is given to the place where models generally performed worse and possible reasons for that are delineated.

8.1. Spatiotemporal and Inaccuracies of Data

The sources of uncertainty in the modelled fluxes include not only the quality of the method representations but also the accuracy and the spatiotemporal resolution of the input data.

The spatial mismatch between satellite products and the measured fluxes was critical for albedo estimates (section 7.2). In this respect, MODIS was the better choice than CERES thanks to its higher spatial resolution (mean absolute error of 0.02 versus 0.05). These two values are consistent with what has been reported in the literature: They correspond to the lower and upper limits of the accuracy range of albedo products that Shunlin Liang et al. (2013) reviewed in their study. 17.1% of CERES estimates had errors above 0.10 while the same happened for only 4.9% in MODIS. Most of the errors in the later one were related to the temporal features of the product, which were unable to capture the intermittent snow events. In order to use MODIS ρ_g products in daily agricultural applications, it's necessary to inter- or extrapolate the data. In section 7.5, the linear interpolation approach propagated the albedo errors to the net radiation in the winter season, resulting in underestimations.

The pixel size of geostationary satellites made its clear sky estimates of $R_{S\downarrow}$ worse than most methods (Table 7-3). This flux is highly dependent on the solar position, and a pixel size of 1º couldn't capture well this variation, especially at low sun elevation angles. For the longwave upwelling flux, the attempt to disaggregate the CERES $R_{L\uparrow}$ product using a temperature ratio was fruitful, improving the estimates in all stations (Table 7-14).

The modelled inputs from GEOS are subject to a higher uncertainty and represent a much larger area than the locally measured variables of the BSRN network. The main difference between the two sources was the total column atmospheric water content, which was much higher in GEOS than in BSRN (Figure 7-5). For this variable, it's not possible to state which data source is more accurate as the local one was not directly measured but estimated according to Prata (1996) from measured relative humidity.

The incoming shortwave parametrizations were much more sensitive to a change in the atmospheric aerosol content than of water. Since the local measurements of aerosol content available at BSRN stations were not downloaded for this study, it was not possible to check how the $R_{S\downarrow clear}$ methods would behave with the change of input source.

For the longwave components, the use of GEOS (modelled data) as input instead of BSRN (field data) generally decreased the performance of most models on an hourly analysis (Table 7-7 and Table 7-11), agreeing with what was observed in the studies by Gubler et al. (2012) and Yu et al. (2018), who noticed significant decline in the performance with increasing dataset inaccuracies. This confirms what was stated as a limitation of modelled-vs-measured review studies of Ruiz-Arias and Gueymard (2018): The overall

ranking of the model performance is constrained by the quality of the input dataset; comparisons between studies to choose the best model are not straight forward and should consider this issue.

The deterioration in performance due to input source variation was particularly strong in the Brutsaert, (1975) method, confirming its dependence on locally measured inputs. The change actually improved Dilley & O'Brien (1998) model, which was developed in response to the growing availability of water vapour data for the whole atmospheric column, like the one of GEOS. In a daily analysis (Table 7-13), the modification of input source from BSRN to GOES had only a small effect on the performance indicators for the cloud correction methods which use additional cloud parameters, e.g. cloud temperature or water content.

Despite the large area covered by CERES cloud products, the $R_{L\downarrow}$ the cloud correction algorithms that applied its cloud fraction product performed better when compared to the clear sky algorithms. Due to the high clouds' spatiotemporal variability, the use of a c_f corresponding to a smaller area should further increase the performance of the models.

According to Yu et al. (2018), the uncertainties in the cloud parameters are the leading source of errors in the computation of $R_{L\downarrow}$. In their paper, the cloud correction $R_{L\downarrow}$ parametrisations that relied solely on cloud fraction performed worse, but that was not necessarily true in the analysis performed here, as the modified Maykut and Church (1973) model's performance was comparable to the ones which had more cloud inputs. This can be related to the accuracy of the cloud parameters, as estimates of cloud fraction are easier than those of temperature, water content or optical depth. These authors recommended the use of Yaping Zhou et al. (2007) when the cloud variables are not accurate. Accordingly, in this study, this model performed very well using CERES cloud products.

Amongst the 15 papers that test all-sky $R_{L\downarrow}$ algorithms, 6 recommend the use of Crawford and Duchon (1999) (Table 4-2), which uses cloud modification factor as an input. Particularly, Li et al. (2017) tested 4 cloud correction algorithms in the 7 SURFRAD stations analysed in this study and CD99 performed best without local calibration. However, this study shows the performance of this algorithm was not better than the others. These authors also found the use of c_{mf} instead of cloud fraction to represent the cloud coverage improved the estimates. This thesis demonstrates this is only the case for models that used the c_{mf} in their original publication, while for all other models, the opposite happens (Table 7-11).

A temporal issue is the fact that the ratio of $R_{S\downarrow clear}$ and $R_{S\downarrow}$, and thus cloud modification factor, cannot be computed at night. One of the causes of poorer performance using c_{mf} input might be the simple interpolation that was adopted. In this study, a linear interpolation between the last hour before sunset and the first hour after sunrise was conducted. However, Gubler et al. (2012) and Zhu et al. (2017) noted this procedure had better results when the time window of the last and first sunshine hours was bigger (3 to 4 hours). A separate analysis of daytime and night-time $R_{L\downarrow}$, would be necessary to confirm the extent of these inaccuracies. The calculation of c_{mf} particularly concerns for higher latitude sites in the winter season, when the solar elevation angle is smaller and the nights, longer. Using c_{mf} as a cloud coverage representation also bring up problems associated with the relative position of the clouds, the sun and the pyranometer.

8.2. Error Analysis

A clear relationship was found between land cover and the upwelling fluxes. The error in albedo estimates was connected to the seasonality and intermittency of snow events. The simplified longwave estimate represented the outgoing fluxes well, except at the stations located in desert or gravel areas, in which the ground temperatures are probably higher, and the emissivities are further away from unity. For CERES $R_{L\uparrow}$, the worst performances were related to higher altitudes and to sand desert areas, stations TBL and GOB

respectively. The limitations of the longwave fluxes of this satellite-based product to high elevation areas have been acknowledged in the literature by Gui et al. (2010) and by Wang and Dickinson (2013) for arid zones. Nevertheless, in the station DRA, located in a gravel area with the lowest atmospheric water content, $R_{L\uparrow}$ was represented well by CERES.

The errors in solar radiation increased with atmospheric aerosol and water content (Table 7-1). The magnitude of the errors due to the changes in aerosols was more pronounced than those in water content. This agrees with the findings of Ruiz-Arias and Gueymard (2018), who, by intercomparing the clear sky methods analysed here, noticed they diverged the most in situations with high w and τ_{550}, especially when combined. Only above a column water vapour content of 5.0cm, a discrepancy between measured and simulated fluxes appears in Ruiz-Arias and Gueymard (2018) study. This value is very close to the maximum water content of clear sky days analysed in this study (5.2cm). As such, the differences in the shortwave fluxes due to the humidity were not as pronounced as the aerosol ones (Table 7-1). These authors also noticed a seasonality effect due to the change in aerosol composition. Accordingly, in this thesis, the poorer performance of the station close to a sand desert was also linked to its distinguished aerosol characteristics.

The errors of the $R_{S\downarrow}$ models increased with decreasing solar elevation angles (Table 7-1), except for MAC87. It is important to point out that the larger the angle, the higher the $R_{S\downarrow TOA}$; so that in relative terms, the errors of the MAC model remained nearly constant. In the work of Ruiz-Arias and Gueymard (2018), the intermodal differences were also higher at lower h_0, particularly when h_0<1º. These authors attributed the variations to the different airmass formulations, which are particularly relevant for the diffuse component when the sun is close to the horizon. In this thesis, the equations to calculate m were the same in all models, apart from RES08, which had even higher errors when h_0<30º (MBE≈100W/m² against MBE≈50W/m² in the worse performing methods). Ruiz-Arias and Gueymard (2018) mentioned that these discrepancies are particularly concerning for places located at higher latitudes in the winter season, when the solar elevation angles remain low. In this study, the station closer to this condition was CAB, which did not have a particularly bad performance. However, a seasonality analysis was not conducted here, so the full effects of the errors under low solar elevation angles could not be studied. To avoid error propagation in the daily estimates, it might be better to remove the points with lower solar elevation angles, as this will cause only small underestimations in the global daily flux.

In the longwave estimates, it is more complicated to pin-point the circumstances that lead to higher errors as they are different for each model (Table 7-6). This was expected as the accuracy of the $R_{L\downarrow}$ methods is related to the similarity between the climatic conditions they were developed for (Choi et al., 2008; Gubler et al., 2012; Kjaersgaard et al., 2007; Zhu et al., 2017). Brutsaert (1975), Dilley and O'Brien (1998) and Prata (1996) used radiative transfer simulations to define the coefficients. However, none of them performed well for all the temperature and water content ranges analysed in this study. All methods tend to be more accurate for temperatures between 15 and 30ºC. Large errors were found for temperature below 0ºC in BT75 and for temperatures above 30ºC in DB98. Higher underestimations were also found in BT75 and in Abramowitz et al. (2012) models for lower humidities. This limitation of BT75 was already mentioned by Prata (1996) and was one of the motivations for this author to establish his own model.

While developing their all-sky model, Abramowitz et al. (2012) noted the unclearness index (ϵ_k) did not provide any extra information on the incoming longwave radiation when compared to temperature and water content alone. Thus, their $R_{L\downarrow}$ equation is a function of only these later two variables. In this study, their approach was indeed better than the clear sky approaches of BT75, PT96 and DB98 for cloudy and all sky conditions (Table 7-6), being comparable to the cloud correction algorithms. Additionally, as cloud coverage increases (Table 7-9), the RMSE of this model increased less than the other all-sky approaches.

However, the MBE of this method changed from -11.8 W/m² for c_f<10% to 23.1W/m² for c_f>75%, the largest variation amongst the all-sky algorithms. This shows that, despite the overall good performance of this model, T_a and e_0 alone cannot capture the changes in $R_{L\downarrow}$ due to the presence of clouds.

The cloud correction methods could control the magnitude of the errors (Table 7-10). However, they still got higher with increasing cloud coverage. For c_f>75%, only Maykut and Church (1973) and Yaping Zhou et al. (2007) show R^2>0.6. MK73 errors were smaller above 75% than below it, and the increase of performance for conditions where c_f<50% is hardly present. This indicates that this model performs better for fully overcast conditions than to partially cloudy ones. Going along with the results of Marthews et al. (2012), the all-sky methods performed better than the pure PT96 approaches even for strictly clear conditions.

Zhu et al. (2017) found relationships between the terrain elevation and the performance of the $R_{L\downarrow}$ methods. The stations analysed by these authors were in the Tibetan plateau, and the lowest altitude was about 3600m. In this study, the highest station was at 1875m (TBL), and there was only a small indicative in the PT96 model of height dependency as this method changed from under- to overestimations (Table 7-7). Compared to the average of the other stations, the CERES $R_{L\downarrow}$ product performed worse at TBL, confirming what was also observed by Gui et al. (2010) that this product is less accurate for elevated surfaces.

8.3. Ground Stations

Some of the models analysed in this study were either calibrated using US data, e.g. Dai and Fang,(2014) and Yaping Zhou et al. (2007) or conceptualised for the standard US atmosphere, e.g. Brutsaert (1975) and Prata (1996). In this thesis, 8 out of 10 stations were in this country. Thus, even though the 7 stations in the SURFRAD network have quite different environmental conditions, there is a bias in the average performance of the models as most of them accomplish better results for these stations. For similar reasons, the clear sky model of the European space agency (EI00 and ER00) perform better in the station in the Netherlands (CAB) than in most US stations, except E13 (Table 7-2).

In this study, the bias is particularly noticed in the clear sky longwave estimates (Table 7-7) for CAB, which had fewer clear sky days than the other stations. It was also pronounced in the Namibian station (GOB), on cloudy and all-sky $R_{L\downarrow}$ estimates (Table 7-11 and Table 7-13).

The station that differed most from the others was GOB. For this reason, it was given more attention in this work. The $R_{S\downarrow clear}$ estimates had their worse indicators in GOB, and this behaviour was linked to the different aerosol characteristics of sand deserts (Table 7-2). In table 20, something very intriguing happened: The change of source from field inputs (BSRN) to coarser resolution data (GEOS) improved the all-sky PT96 estimates drastically, making this clear sky method more suitable to estimate daily all-sky $R_{L\downarrow}$ than all the other cloud correction methods and CERES $R_{L\downarrow}$ product.

The outstanding behaviour of $R_{L\downarrow}$ in GOB can be linked to inaccurate GEOS representation of atmospheric water content, which already accounted for cloud contribution in the clear sky method. First, in the net radiation computation (Figure 7-11.c), the input temperature source was from BSRN while the water content was from GEOS. Comparing these results with Table 7-13, it was noted that the $R_{L\downarrow}$ errors were more similar to the ones using the modelled inputs, linking them to the GEOS w representations and not to T_a. Second, in Figure 7-5.c, it was shown that GEOS w estimates much higher than BSRN ones. This was particularly true for GOB, where the value of the 75% quartile (w=1.78cm) in BSRN is only 0.9cm higher than the median of GEOS (w=1.69cm). Third, in PT96 (Table 7-13), the higher water content in GEOS diminished the underestimation in $R_{L\downarrow clear}$ from -17.5W/m² to -3.6W/m². Then, the cloud correction

methods, which in general reduced the underestimations (Figure 7-9), resulted in significant overestimations of the fluxes using GEOS data (22.0<MBE<37.0 W/m² in Table 7-13). Putting it all together, GEOS overestimated the water content in this station, which served as a cloud correction and improved the $R_{L\downarrow}$ estimate for a clear sky method (PT96). When the cloud effect was actually entered as an input, it resulted in overestimations in $R_{L\downarrow}$ for cloud correction methods

Gui et al. (2010) and Wang and Dickinson (2013) linked some of the CERES errors to the input dataset, i.e. clouds, water and temperature, as well as its algorithms for arid regions. In here, the errors were explicitly related to the modelled w in GOB since CERES also use GEOS data as input. This also explains why it performs well in DRA, a station that is located in an even drier region than GOB.

9. CONCLUSIONS AND RECOMMENDATIONS

This study consisted of a review of methods to estimate surface net radiation in an hourly and daily scale. A total of 25 models of R_n components were compared with ground data from 10 stations of the high-quality BSRN network. More specifically, 2 albedo products, 2 models for upwelling longwave radiation, 9 for clear sky solar fluxes, 3 clear and 9 all sky longwave downwelling methods were analysed. Most of them were parametrisations, however, satellite-based products of MODIS, CERES and MSG/GOES were also included.

In the hourly analysis, the best clear sky method to estimate $R_{S\downarrow}$ was Iqbal (1983), which could estimate the fluxes with RMSE=28.4W/m², MBE=3.9W/m², R^2=0.97. The approach by Prata (1996) was able to represent well $R_{L\downarrow clear}$ (RMSE=22.8 W/m², MBE=9.1W/m² R^2=0.85), yet, it performed poorly for a station in the Netherlands. Even though the spatial resolution of CERES cloud products is quite poor (1º), the cloud correction methods that use it as an input improved the $R_{L\downarrow}$ estimates. Particularly, Maykut and Church (1973), P. Schmetz et al. (1986) and Yaping Zhou et al. (2007) were able to keep the all-sky errors in the same range as the clear sky ones (RMSE<25.0W/m², |MBE|<6.0W/m² and R^2>0.80. The accuracy of the methods varied across stations, and the one closer to a desert in Namibia had the worse overall performances.

Temporal upscaling from hourly to daily reduced the errors of the longwave downwelling components (RMSE<17.0W/m², |MBE|<6.0W/m²), putting them in the same range of daily clear sky shortwave estimates (RMSE<13W/m², |MBE|<8.0W/m²). However, the variance in $R_{S\downarrow clear}$ is explained much better than in the $R_{L\downarrow}$ (R^2>0.98 and R^2>0.90, respectively).

Due to the smaller pixel size, the albedo product of MODIS was more related to the ground measurements than the one of CERES (MAE=0.02 *versus* MAE=0.05W/m²). Because of intermittent snow, linear interpolating the missing MODIS data resulted in errors in the $R_{S\uparrow}$ component for the winter season.

Apart from stations located in desert or gravel areas, CERES $R_{L\uparrow}$ products performed no better than a simple application of the Stefan Boltzmann law assuming emissivity equal to unity and the same value of ground and air temperatures (RMSE=12.6W/m², MBE=-2.8W/m², R^2=0.96). An attempt to downscale the CERES product using an air temperature ratio improved its accuracy. Similar downscaling procedures could be applied to the downwelling component as, despite its pixel size, the $R_{L\downarrow}$ products were quite accurate.

The change in the input source from locally measured variables to modelled generally decreased the performance of the longwave downwelling radiation methods. Particularly, the inaccuracies of the all-sky $R_{L\downarrow}$ models using GEOS data for the station in Namibia was linked to the poor quality of the total column atmospheric water vapour of this dataset for that region, which also justifies the worse performance of CERES $R_{L\downarrow}$ products in this station.

An analysis of the same type could not be performed for changes in the aerosol content, the leading cause of errors in the $R_{S\downarrow clear}$, as no local aerosol measurements were downloaded. However, this could be addressed in further studies. For this component, the inaccuracies were also linked to low solar elevation angles. In the longwave estimates, it's more complicated to pinpoint the circumstances that lead to higher errors as they diverge for each model. It might be interesting to do a separate analysis of daytime and night-time estimates to further investigate the effects of surface inversions and cloud modification factor interpolations.

LIST OF REFERENCES

Abramowitz, G., Pouyanné, L., & Ajami, H. (2012). On the information content of surface meteorology for downward atmospheric long-wave radiation synthesis. *Geophysical Research Letters*, *39*(4), 1–5. https://doi.org/10.1029/2011GL050726

Alados, I., Foyo-Moreno, I., & Alados-Arboledas, L. (2012). Estimation of downwelling longwave irradiance under all-sky conditions. *International Journal of Climatology*, *32*(5), 781–793. https://doi.org/10.1002/joc.2307

Allen, R. G., Masahiro, T., & Trezza, R. (2007). Based Energy Balance for Mapping Evapotranspiration with Internalized Calibration (METRIC)— Model. *Journal of Irrigation and Drainage Engineering*, *133*(4), 380–394. https://doi.org/10.1061/(ASCE)0733-9437(2007)133

Allen, R. G., Pereira, L. S., Raes, D., & Smith, M. (1998). Meteorological data. In *Crop evapotranspiration: Guidelines for computing crop requirements. Irrigation and Drainage Paper No. 56* (p. 300). Rome, Italy: FAO.

Ångström, A. K. (1915). *A study of the radiation of the atmosphere: based upon observations of the nocturnal radiation during expeditions to Algeria and to California (Vol. 65)*. Washington: Smithsonian Institution.

Augustine, J. A., DeLuisi, J. J., & Long, C. N. (2000). SURFRAD—A National Surface Radiation Budget Network for Atmospheric Research. *Bulletin of the American Meteorological Society*, *81*(10), 2341–2357. https://doi.org/10.1175/1520-0477(2000)081<2341:SANSRB>2.3.CO;2

Augustine, J. A., Hodges, G. B., Cornwall, C. R., Michalsky, J. J., & Medina, C. I. (2005). An Update on SURFRAD—The GCOS Surface Radiation Budget Network for the Continental United States. *Journal of Atmospheric and Oceanic Technology*, *22*(10), 1460–1472. https://doi.org/10.1175/JTECH1806.1

Bastiaanssen, W. G. M., Pelgrum, H., Wang, J., Ma, Y., Moreno, J. F., Roerink, G. J., & Van Der Wal, T. (1998). A remote sensing surface energy balance algorithm for land (SEBAL): 2. Validation. *Journal of Hydrology*, *212–213*(1–4), 213–229. https://doi.org/10.1016/S0022-1694(98)00254-6

Bilbao, J., & de Miguel, A. H. (2007). Estimation of daylight downward longwave atmospheric irradiance under clear-sky and all-sky conditions. *Journal of Applied Meteorology and Climatology*, *46*(6), 878–889. https://doi.org/10.1175/JAM2503.1

Bird, R. E., & Hulstrom, R. L. (1981a). A simplified clear sky model for direct and diffuse insolation on horizontal surfaces. *Solar Energy Research Institute, Golden, CO, SERI/TR*.

Bird, R. E., & Hulstrom, R. L. (1981b). Review, Evaluation, and Improvement of Direct Irradiance Models. *Journal of Solar Energy Engineering*, *103*, 182–192. https://doi.org/10.1115/1.3266239

Brunt, D. (1932). Notes on radiation in the atmosphere. I. *Quarterly Journal of the Royal Meteorological Society*, *58*(247), 389–420.

Brutsaert, W. (1975). On a derivable formula for long-wave radiation from clear skies. *Water Resources Research*, *11*(5), 742–744. https://doi.org/10.1029/WR011i005p00742

Carmona, F., Rivas, R., & Caselles, V. (2014). Estimation of daytime downward longwave radiation under clear and cloudy skies conditions over a sub-humid region. *Theoretical and Applied Climatology*, *115*(1–2), 281–295. https://doi.org/10.1007/s00704-013-0891-3

Cheng, J., Liang, S., Wang, W., & Guo, Y. (2017). An efficient hybrid method for estimating clear-sky surface downward longwave radiation from MODIS data. *Journal of Geophysical Research*, *122*(5), 2616–2630. https://doi.org/10.1002/2016JD026250

Choi, M. (2013). Parameterizing daytime downward longwave radiation in two Korean regional flux monitoring network sites. *Journal of Hydrology*, *476*, 257–264. https://doi.org/10.1016/j.jhydrol.2012.10.041

Choi, M., Jacobs, J. M., & Kustas, W. P. (2008). Assessment of clear and cloudy sky parameterizations for daily downwelling longwave radiation over different land surfaces in Florida, USA. *Geophysical Research Letters*, *35*(20). https://doi.org/10.1029/2008GL035731

Choudhury, B. (1982). A parameterized model for global insolation under partially cloudy skies. *Solar Energy*, *29*(6), 479–486.

Crawford, T. M., & Duchon, C. E. (1999). An Improved Parameterization for Estimating Effective Atmospheric Emissivity for Use in Calculating Daytime Downwelling Longwave Radiation. *Journal of Applied Meteorology*, *38*(4), 474–480. https://doi.org/10.1175/1520-0450(1999)038<0474:AIPFEE>2.0.CO;2

Dai, Q., & Fang, X. (2014). A simple model to predict solar radiation under clear sky conditions. *Advances in Space Research*, *53*(8), 1239–1245. https://doi.org/10.1016/j.asr.2014.01.025

Davies, J. A., & McKay, D. C. (1982). Estimating solar irradiance and components. *Solar Energy*, *29*(1), 55–

64. https://doi.org/10.1016/0038-092X(82)90280-8
Davies, J. A., Schertzer, W., & Nunez, M. (1975). Estimating global solar radiation. *Boundary-Layer Meteorology*, *9*(1), 33–52. https://doi.org/10.1007/BF00232252
Davies, R., Randall, D. A., & Corsetti, T. G. (1987). A fast radiation parameterization for atmospheric circulation models. *Journal of Geophysical Research*, *92*(D1), 1009–1016.
Dedieu, G., Deschamps, P. Y., & Kerr, Y. H. (1987). Satellite estimation of solar irradiance at the surface of the Earth and of surface albedousing a physical model applied to meteosat data. *Journal of Climate and Applied Meteorology*, *26*(1), 79–87.
Diak, G. R., Bland, W. L., Mecikalski, J. R., & Anderson, M. C. (2000). Satellite-based estimates of longwave radiation for agricultural applications. *Agricultural and Forest Meteorology*, *103*(4), 349–355. https://doi.org/10.1016/S0168-1923(00)00141-6
Dilley, A. C., & O'Brien, D. M. (1998). Estimating downward clear sky long-wave irradiance at the surface from screen temperature and precipitable water. *Quarterly Journal of the Royal Meteorological Society*, *124*(549), 1391–1401. https://doi.org/10.1256/smsqj.54902
Dobos, E. (2006). Albedo. In R. Lal (Ed.), *Encyclopedia of Soil Science* (p. 1924). CRC Press. https://doi.org/10.1081/E-ESS
Driemel, A., Augustine, J., Behrens, K., Colle, S., Cox, C., Cuevas-Agulló, E., … König-Langlo, G. (2018). Baseline Surface Radiation Network (BSRN): structure and data description (1992–2017). *Earth System Science Data Discussions*, *10*, 1491–1501. https://doi.org/10.5194/essd-2018-8
Duarte, H. F., Dias, N. L., & Maggiotto, S. R. (2006). Assessing daytime downward longwave radiation estimates for clear and cloudy skies in Southern Brazil. *Agricultural and Forest Meteorology*, *139*(3–4), 171–181. https://doi.org/10.1016/j.agrformet.2006.06.008
Duguay, C. R. (1995). An approach to the estimation of surface net radiation in mountain areas using remote sensing and digital terrain data. *Theoretical and Applied Climatology*, *52*, 55–68. https://doi.org/https://doi.org/10.1007/BF00865507
EUMETSAT Satellite Application Facility on Land Surface Analysis [LSA SAF]. (2011). Product User Manual Down-welling Surface Shortwave Flux (DSSF).
Finch, J. W., & Best, M. J. (2004). The accuracy of downward short- and long-wave radiation at the earth's surface calculated using simple models. *Meteorological Applications*, *11*(1), 33–39. https://doi.org/10.1017/S1350482703001154
Flerchinger, G. N., Xaio, W., Marks, D., Sauer, T. J., & Yu, Q. (2009). Comparison of algorithms for incoming atmospheric long-wave radiation. *Water Resources Research*, *45*(3), 1–14. https://doi.org/10.1029/2008WR007394
Fu, Q., Liou, K. N., Cribb, M. C., Charlock, T. P., & Grossman, A. (1997). Multiple Scattering Parameterization in Thermal Infrared Radiative Transfer. *Journal of the Atmospheric Sciences*, *54*, 2799–2812.
Garratt, J. R. (1992). Extreme Maximum Land Surface Temperatures. *Journal of Applied Meteorology*, *31*(9), 1096–1105. https://doi.org/10.1175/1520-0450(1992)031<1096:EMLST>2.0.CO;2
Gillespie, A. (2014). Land Surface Emissivity. In E. G. Njoku (Ed.), *Encyclopedia of Remote Sensing* (New York, pp. 303–311). Springer New York. https://doi.org/10.1007/978-0-387-36699-9_77
Gubler, S., Gruber, S., & Purves, R. S. (2012). Uncertainties of parameterized surface downward clear-sky shortwave and all-sky longwave radiation. *Atmospheric Chemistry and Physics*, *12*(11), 5077–5098. https://doi.org/10.5194/acp-12-5077-2012
Gueymard, C. A. (2003). Direct solar transmittance and irradiance with broadband models. Part I: detailed theoretical performance assessment. *Solar Energy*, *74*, 355–379. https://doi.org/10.1016/j.solener.2003.11.002
Gueymard, C. A. (2008). REST2: High-performance solar radiation model for cloudless-sky irradiance, illuminance, and photosynthetically active radiation - Validation with a benchmark dataset. *Solar Energy*, *82*(3), 272–285. https://doi.org/10.1016/j.solener.2007.04.008
Gueymard, C. A. (2012). Clear-sky irradiance predictions for solar resource mapping and large-scale applications: Improved validation methodology and detailed performance analysis of 18 broadband radiative models. *Solar Energy*, *86*(8), 2145–2169. https://doi.org/10.1016/j.solener.2011.11.011
Gui, S., Liang, S., & Li, L. (2010). Evaluation of satellite-estimated surface longwave radiation using ground-based observations. *Journal of Geophysical Research*, *115*(D18), D18214. https://doi.org/10.1029/2009JD013635
Gupta, S. K., Kratz, D. P., Stackhouse, P. W., & Wilber, A. C. (2001). The Langley Parameterized Shortwave Algorithm (LPSA) for Surface Radiation Budget Studies.

Hunt, L. A., Kuchar, L., & Swanton, C. J. (1998). Estimation of solar radiation for use in crop modelling. *Agricultural and Forest Meteorology*, *91*(3), 293–300. https://doi.org/https://doi.org/10.1016/S0168-1923(98)00055-0

Idso, S. B. (1981). A set of equations for full spectrum and 8- to 14-μm and 10.5- to 12.5-μm thermal radiation from cloudless skies. *Water Resources Research*, *17*(2), 295–304. https://doi.org/10.1029/WR017i002p00295

Idso, S. B., & Jackson, R. D. (1969). Thermal radiation from the atmosphere. *Journal of Geophysical Research*, *74*(23), 5397–5403. https://doi.org/10.1029/JC074i023p05397

Ineichen, P. (2008a). A broadband simplified version of the Solis clear sky model. *Solar Energy*, *82*(8), 758–762. https://doi.org/10.1016/j.solener.2008.02.009

Ineichen, P. (2008b). Conversion function between the Linke turbidity and the atmospheric water vapor and aerosol content. *Solar Energy*, *82*(11), 1095–1097. https://doi.org/10.1016/j.solener.2008.04.010

Iqbal, M. (1983). *An Introduction to Solar Radiation*. Academic Press.

Iziomon, M. G., Mayer, H., & Matzarakis, A. (2003). Downward atmospheric longwave irradiance under clear and cloudy skies: Measurement and parameterization. *Journal of Atmospheric and Solar-Terrestrial Physics*, *65*(10), 1107–1116. https://doi.org/10.1016/j.jastp.2003.07.007

Jacobs, J. D. (1978). Radiation climate of Broughton Island. In R. G. Barry & J. D. Jacobs (Eds.), *Energy Budget Studies in Relation to Fast-ice Breakup Processes in Davis Strait* (Paper No., pp. 105–120). Boulder: Institiute of Arctic and Alpine Research, University of Colorado.

Jia, A., Jiang, B., Liang, S., Zhang, X., & Ma, H. (2016). Validation and spatiotemporal analysis of CERES surface net radiation product. *Remote Sensing*, *8*(2), 1–19. https://doi.org/10.3390/rs8020090

Jiang, B., Liang, S., Ma, H., Zhang, X., Xiao, Z., Zhao, X., … Jia, A. (2016). GLASS daytime all-wave net radiation product: Algorithm development and preliminary validation. *Remote Sensing*, *8*(3). https://doi.org/10.3390/rs8030222

Jiang, B., Zhang, Y., Liang, S., Wohlfahrt, G., Arain, A., Cescatti, A., … Zhang, X. (2015). Empirical estimation of daytime net radiation from shortwave radiation and ancillary information. *Agricultural and Forest Meteorology*, *211–212*, 23–36. https://doi.org/10.1016/j.agrformet.2015.05.003

Kalisch, J., & MacKe, A. (2012). Radiative budget and cloud radiative effect over the Atlantic from ship-based observations. *Atmospheric Measurement Techniques*, *5*(10), 2391–2401. https://doi.org/10.5194/amt-5-2391-2012

Kasten, F., & Young, A. T. (1989). Revised optical air mass tables and approximation formula. *Applied Optics*, *28*(22), 4735–4738.

Kato, S., Rose, F. G., Sun-Mack, S., Miller, W. F., Chen, Y., Rutan, D. A., … Collins, W. D. (2011). Improvements of top-of-atmosphere and surface irradiance computations with CALIPSO-, CloudSat-, and MODIS-derived cloud and aerosol properties. *Journal of Geophysical Research*, *116*, D19209. https://doi.org/10.1029/2011JD016050

Kim, H. Y., & Liang, S. (2010). Development of a hybrid method for estimating land surface shortwave net radiation from MODIS data. *Remote Sensing of Environment*, *114*(11), 2393–2402. https://doi.org/10.1016/j.rse.2010.05.012

Kimball, B. A., Idso, S. B., & Aase, J. K. (1982). A model of thermal radiation from partly cloudy and overcast skies. *Water Resources Research*, *18*(4), 931–936. https://doi.org/10.1029/WR018i004p00931

Kjaersgaard, J. H., Plauborg, F. L., & Hansen, S. (2007). Comparison of models for calculating daytime long-wave irradiance using long term data set. *Agricultural and Forest Meteorology*, *143*(1–2), 49–63. https://doi.org/10.1016/j.agrformet.2006.11.007

Li, M., Jiang, Y., & Coimbra, C. F. M. (2017). On the determination of atmospheric longwave irradiance under all-sky conditions. *Solar Energy*, *144*, 40–48. https://doi.org/10.1016/j.solener.2017.01.006

Liang, S. (2018). Volume 5 Overview: Recent progress in Remote Sensing of Earth's Energy Budget. *Comprehensive Remote Sensing*, 1–31. https://doi.org/10.1016/B978-0-12-409548-9.10365-3

Liang, S., Zhang, X., He, T., Cheng, J., & Wang, D. (2013). Remote Sensing of the Land Surface Radiation Budget. In G. P. Petropoulos (Ed.), *Remote Sensing of Energy Fluxes and Soil Moisture Content* (pp. 121–162). CRC Press. https://doi.org/doi:10.1201/b15610-7\r10.1201/b15610-7

Long, C. N., & Dutton, E. G. (2010). BSRN Global Network recommended QC tests, V2. Bremerhaven: PANGEA. Retrieved from https://epic.awi.de/id/eprint/30083/1/BSRN_recommended_QC_tests_V2.pdf

Marthews, T. R., Malhi, Y., & Iwata, H. (2012). Calculating downward longwave radiation under clear and cloudy conditions over a tropical lowland forest site: An evaluation of model schemes for hourly data. *Theoretical and Applied Climatology*, *107*(3–4), 461–477. https://doi.org/10.1007/s00704-011-0486-9

Maykut, G. A., & Church, P. E. (1973). Radiation Climate of Barrow, Alaska, 1962-66. *Journal of Applied Meteorology*, *12*, 620–628. https://doi.org/10.1175/1520-0450(1973)012<0620:RCOBA>2.0.CO;2

Milan, A. (2011). GOES Surface and Insolation Products. Retrieved January 29, 2019, from https://www.bou.class.noaa.gov/saa/products/nmmr/xml-to-text-ISO/GSIP

Montieth, J. L., & Unsworth, M. H. (1990). *Principles of Environmental Physics* (2nd ed.). New York, NY: Arnold.

NASA. (2015). GEOS-5 FP Product Details. Retrieved January 26, 2019, from https://gmao.gsfc.nasa.gov/products/GEOS-5_FP_details.php

NASA. (2018). CERES Computed Fluxes for Consistent Clouds. Retrieved January 26, 2019, from https://ceres.larc.nasa.gov/science_information.php?page=CeresComputeFlux

Niemelä, S., Räisänen, P., & Savijärvi, H. (2001). Comparison of surface radiative flux parameterizations part I: Longwave radiation. *Atmospheric Research*, *58*(1), 1–18. https://doi.org/10.1016/S0169-8095(01)00084-9

Pérez-García, M. (2004). Simplified modelling of the nocturnal clear sky atmospheric radiation for environmental applications. *Ecological Modelling*, *180*(2–3), 395–406. https://doi.org/10.1016/j.ecolmodel.2004.04.027

Prata, A. J. (1996). A new long-wave formula for estimating downward clear-sky radiation at the surface. *Quarterly Journal of the Royal Meteorological Society*, *122*(533), 1127–1151. https://doi.org/10.1256/smsqj.53305

Remund, J., Wald, L., Lefevre, M., Ranchin, T., & Page, J. (2003). Worldwide Linke turbidity information. In *ISES Solar World Congress*.

Rienecker, M. M., Suarez, M. J., Todling, R., Bacmeister, J., Takacs, L., Liu, H.-C., … Nielsen, J. E. (2008). *The GEOS-5 Data Assimilation System – Documentation of Versions 5.0.1, 5.1.0, and 5.2.0* (Vol. 27).

Rigollier, C., Bauer, O., & Wald, L. (2000). On the clear sky model of ESRA - European Solar Radiation Atlas - with respect to the Heliosat method, *68*(1), 33–48.

Roesch, A., Wild, M., Ohmura, A., Dutton, E. G., Long, C. N., & Zhang, T. (2011). Corrigendum to "Assessment of BSRN radiation records for the computation of monthly means" published in Atmos. Meas. Tech., 4, 339–354, 2011. *Atmospheric Measurement Techniques*, *4*, 973–973. https://doi.org/10.5194/amt-4-973-2011

Ruiz-Arias, J. A., & Gueymard, C. A. (2018). Worldwide inter-comparison of clear-sky solar radiation models: Consensus-based review of direct and global irradiance components simulated at the earth surface. *Solar Energy*, *168*(February), 10–29. https://doi.org/10.1016/j.solener.2018.02.008

Santos, C. A. C. dos, Da Silva, B. B., Rao, T. V. R., Satyamurty, P., & Manzi, A. O. (2011). Downward longwave radiation estimates for clear-sky conditions over northeast Brazil. *Revista Brasileira de Meteorologia*, *26*(3), 443–450. https://doi.org/10.1590/S0102-77862011000300010

Satterlund, D. R. (1979). An improved equation for estimating long-wave radiation from the atmosphere. *Water Resources Research*, *15*(6), 1649–1650. https://doi.org/10.1029/WR015i006p01649.

Schaaf, C., & Wang, Z. (2015). MCD43A3 MODIS/Terra+Aqua BRDF/Albedo Daily L3 Global - 500m V006 [Data set]. *NASA EOSDIS Land Processes DAAC*. https://doi.org/10.5067/MODIS/MCD43A3.006

Schmetz, J. (1989). Towards a surface radiation climatology: Retrieval of downward irradiances from satellites. *Atmospheric Research*, *23*(3–4), 287–321. https://doi.org/10.1016/0169-8095(89)90023-9

Schmetz, P., Schmetz, J., & Raschke, E. (1986). Estimation of daytime downward longwave radiation at the surface from satellite and grid point data. *Theoretical and Applied Climatology*, *37*(3), 136–149. https://doi.org/10.1007/BF00867847

Sellers, W. D. (1965). *Physical Climatology*. Chicago: University of Chicago Press.

Sicart, J. E., Essery, R. L., Pomeroy, J. W., Hardy, J., Link, T., & Marks, D. (2004). A sensitivity study of daytime net radiation during snowmelt to forest canopy and atmospheric conditions. *Journal of Hydrometeorology*, *5*(5), 774–784. https://doi.org/https://doi.org/10.1175/1525-7541(2004)005<0774:ASSODN>2.0.CO;2

Sicart, J. E., Pomeroy, J. W., Essery, R. L. H., & Bewley, D. (2006). Incoming longwave radiation to melting snow: observations, sensitivity and estimation in northern environments. *Hydrological Processes*, *20*, 3697–3708. https://doi.org/10.1002/hyp.6383

Stephens, G. L., Li, J., Wild, M., Clayson, C. A., Loeb, N., Kato, S., … Andrews, T. (2012). An update on Earth's energy balance in light of the latest global observations. *Nature Geoscience*, *5*(10), 691–696. https://doi.org/10.1038/ngeo1580

Strahler, A. H., Lucht, W., Schaaf, C. B., Tsang, T., Gao, F., Li, X., … Barnsley, M. J. (1999). *MODIS BRDF*

/ albedo product: algorithm theoretical basis document version 5.0. Retrieved from https://lpdaac.usgs.gov/sites/default/files/public/product_documentation/atbd_mod09_v5.pdf

Su, Z. (2002). The Surface Energy Balance System (SEBS) for estimation of turbulent heat fluxes. *Hydrology and Earth System Sciences*, *6*(1), 85–100. https://doi.org/10.5194/hess-6-85-2002

Suttles, J. T., & Ohring, G. (Eds.). (1986). *Surface Radiation Budget for Climate Applications*. Washington D.C. Retrieved from https://ntrs.nasa.gov/archive/nasa/casi.ntrs.nasa.gov/19860019102.pdf

Swinbank, W. C. (1963). Longwave radiation from clear skies. *Quarterly Journal of the Royal Meteorological Society*, *89*, 339–348.

Trigo, I. F., Dacamara, C. C., Viterbo, P., Roujean, J.-L., Olesen, F., Barroso, C., … Arboleda, A. (2011). The Satellite Application Facility for Land Surface Analysis. *International Journal of Remote Sensing*, *32*(10), 2725–2744. https://doi.org/10.1080/01431161003743199

Unsworth, M. H., & Monteith, J. L. (1975). Long-wave radiation at the ground. *Quarterly Journal of the Royal Meteorological Society*, *101*, 13–24.

Wang, K., & Dickinson, R. E. (2013). Global atmospheric downward longwave radiation at the surface from ground-based observations, satellite retrievals, and reanalyses. *Reviews of Geophysics*, *51*(3), 150–185. https://doi.org/10.1002/rog.20009

Wang, K., & Liang, S. (2009). Global atmospheric downward longwave radiation over land surface under all-sky conditions from 1973 to 2008. *Journal of Geophysical Research Atmospheres*, *114*(19). https://doi.org/10.1029/2009JDO11800

Wu, H., Zhang, X., Liang, S., Yang, H., & Zhou, G. (2012). Estimation of clear-sky land surface longwave radiation from MODIS data products by merging multiple models. *Journal of Geophysical Research Atmospheres*, *117*(22), 1–15. https://doi.org/10.1029/2012JD017567

Yu, S., Xin, X., Liu, Q., Zhang, H., & Li, L. (2018). Comparison of Cloudy-Sky Downward Longwave Radiation Algorithms Using Synthetic Data, Ground-Based Data, and Satellite Data. *Journal of Geophysical Research: Atmospheres*, *123*(10), 5397–5415. https://doi.org/10.1029/2017JD028234

Zheng, C., Wang, Q., & Li, P. (2016). Coupling SEBAL with a new radiation module and MODIS products for better estimation of evapotranspiration. *Hydrological Sciences Journal*, *61*(8), 1535–1547. https://doi.org/10.1080/02626667.2015.1031762

Zhou, Y., & Cess, R. D. (2001). Algorithm development strategies for retrieving the downwelling longwave flux at the Earth's surface. *Journal of Geophysical Research Atmospheres*, *106*(D12), 12477–12488. https://doi.org/10.1029/2001JD900144

Zhou, Y., Kratz, D. P., Wilber, A. C., Gupta, S. K., & Cess, R. D. (2007). An improved algorithm for retrieving surface downwelling longwave radiation from satellite measurements. *Journal of Geophysical Research*, *112*(D15), D15102. https://doi.org/10.1029/2006JD008159

Zhou, Y., Yan, G., Zhao, J., Chu, Q., Liu, Y., Yan, K., … Zhang, W. (2018). Estimation of daily average downward shortwave radiation over Antarctica. *Remote Sensing*, *10*(3). https://doi.org/10.3390/rs10030422

Zhu, M., Yao, T., Yang, W., Xu, B., & Wang, X. (2017). Evaluation of parameterizations of incoming longwave radiation in the high-mountain region of the Tibetan Plateau. *Journal of Applied Meteorology and Climatology*, *56*(4), 833–848. https://doi.org/10.1175/JAMC-D-16-0189.1

APPENDICES

Appendix A: formulas

Common formulation

$$e_{s_{min}} = \frac{0.6108\exp\left(17.27T_{a_{min}} - 273.15\right)}{T_{a_{min}} + 0.15}$$

$$e_{s_{max}} = \frac{0.6108\exp\left(17.27T_{a_{min}} - 273.15\right)}{T_{a_{max}} + 0.15}$$

$$e_0 = 10\frac{e_{s_{min}}{}^{RH_{max}}/_{100} + e_{s_{max}}{}^{RH_{min}}/_{100}}{2}$$

$$j' = \frac{2\,\pi\,(doy - 1)}{365.25}$$

$$b = \frac{2\,\pi\,(doy - 81)}{364}$$

$$sc = 0.1645\sin 2b - 0.1255\cos b - 0.025\ \sin b$$

$$d_{time} = h_{local} + \frac{min_{local} - lon_{cor}}{60}$$

$$lon_{cor} = 4(lon - lon_{ref})$$

$$h_a = \frac{\pi}{12}(d_{time} + sc - 12\ )$$

$$decl = \sin^{-1}(0.3978 + \sin(j' - 1.4 + 0.0355\sin(j' - 0.0489)))$$

$$\sin h_0 = \cos(lat)\cos(decl)\cos(h_a) + \sin(lat)\sin(decl)$$

$$\varepsilon = 1.00011 + 0.034221\cos(j') + 0.00128\sin(j')\ + 0.000719\cos(2j') + 0.000077\sin(2j')$$

$$w = 46.5\frac{e_0}{T_a}$$

BH81

$$X_O = O_3\,m$$

$$X_w = w\,m$$

$$\tau_A = 0.2758\tau_{380} + 0.35\tau_{500}$$

$$T_R = \exp\left(-0.0903m'^{0.84}(1 + m' - m'^{1.01})\right)$$

$$T_{UM} = \exp\left(-0.0127m'^{0.26}\right)$$

$$T_O = 1 - 0.1611X_O(1 + 139.48X_O)^{-0.3035} - 0.002715X_O\left(1 + 0.044X_O + 0.0003{X_O}^2\right)^{-1}$$

$$T_w = 1 - 2.4959X_w((1 + 79.034X_w)^{0.6828} + 6.385X_w)^{-1}$$

$$T_A = \exp(-{\tau_A}^{0.873}(1 + \tau_A - {\tau_A}^{0.7088})m^{0.9108})$$

$$T_{AA} = 1 - k_1(1 - m + m^{1.06})(1 - T_A)$$

$$T_{AS} = {T_A}/{T_{AS}}$$

$$\rho_s = 0.0685 + (1 - B_a)(1 - T_{AS})$$

IQ83

$$T_A = (0.12445\alpha - 0.0162) + (1.003 - 0.125\alpha)\exp\left(-m'\beta(1.089\alpha + 0.5123)\right)$$

MAC87

$$X_O = {}^{O_3}/_{10}\ m$$

$$X_w = w\ m$$

$$\tau_A = 0.35\tau_{550}(0.7368(1.447)^{\alpha} + 1.1^{\alpha})$$

$$T_O = 1 - \frac{0.1082X_O}{(1 + 13.86X_O)} + \frac{0.00658X_O}{1 + (10.36X_O)^3} + \frac{0.002118X_O}{1 + 0.0042X_O + 0.00000323{X_O}^2}$$

$$a_w = \frac{0.29X_w}{(1 + 14.15X_w)^{0.635} + 0.5925X_w}$$

$$T_R = \frac{8.688237m^{0.0279286 \ln m - 0806955}}{1 + 8.688237m^{0.0279286 \ln m - 0806955}}$$

$$T_A = \exp(m'\tau_A)$$

$$\rho_s = 0.0685 - 0.151\omega_0(1 - B_a)$$

EI00 and ER00

$$\Delta h_0 = \left(0.061359\frac{0.1594 + 1.123h_{0_{rad}} + 0.065656{h_{0_{rad}}}^2}{1 + 28.9344h_{0_{rad}} + 277.3971{h_{0_{rad}}}^2}\right){}^{180}/_{\pi}$$

$$h_{0_{ref}} = h_0 + \Delta h_0$$

$$\delta_R(m') = \begin{cases} (6.6296 + 1.7513m' - 0.1202m'^2 + 0.0065m'^3 - 0.00013m'^4)^{-1}, & m' \le 20 \\ (10.4 + 0.718\mathrm{m}')^{-1}, & m' > 20 \end{cases}$$

$$T_{RD} = -0.015843 + 0.030543T_{LK} + 0.0003797{T_{LK}}^2$$

$$A_0' = 0.26463 - 0.061581T_{LK} + 0.00314087{T_{LK}}^2$$

$$A_0(A_0', T_{RD}) = \begin{cases} {0.002}/{T_{RD}}, & A_0'T_{RD} < 0.002 \\ A_0', & A_0'T_{RD} \ge 0.002 \end{cases}$$

$$A_1 = 2.04020 + 0.018945T_{LK} - 0.011161{T_{LK}}^2$$

$$A_2 = -1.3025 + 0.039231T_{LK} + 0.0085079{T_{LK}}^2$$

$$F_D = A_0 + A_1 \sin h_0 + A_2 \sin^2 h_0$$

$$T_{LK2} = 3.91\tau_{550}\exp\left(0.689\,{p_{sl}}/{p}\right) + 0.376\ln w + 2 + 0.54\,{p_{sl}}/{p} - 0.5\left({p_{sl}}/{p}\right)^2 + 0.16\left({p_{sl}}/{p}\right)^3$$

$$T_{LK2} = 1.8494 + 0.2425w - 0.0203w^2 + \beta(15.427 + 0.3153w - 0.0254w^2)$$

IN08

$$T_C = 0.12w^{0.56}{\tau_{700}}^2 + 0.97w^{0.032}\tau_{700} + 1.08w^{0.0051} + 0.071\ln {}^{p}/_{p_{sl}}$$

$$\tau_{DIR} = tr_1\tau_{700} + tr_0 + tr_p \ln {}^{p}/_{p_{sl}}$$

$$\tau_{DIF} = tf_4{\tau_{700}}^4 + tf_3{\tau_{700}}^3 + tf_2{\tau_{700}}^2 + tf_1\tau_{700} + tf_0 + tf_p \ln {}^{p}/_{p_{sl}}$$

$$\tau_{S\downarrow} = ts_1\tau_{700} + ts_0 + ts_p \ln {}^{p}/_{p_{sl}}$$

$$r = r_1 \ln w + r_0$$

$$r_0 = -0.7565{\tau_{700}}^2 + 0.5057\tau_{700} + 0.4557$$

$$r_1 = 0.00925{\tau_{700}}^2 + 0.0148\tau_{700} - 0.0172$$

$$tr_0 = 0.33 + 0.045 \ln w + 0.0096 \ln^2 w$$

$$tr_1 = 1.82 + 0.056 \ln w + 0.0071 \ln^2 w$$

$$tr_p = 0.0089\mathrm{w} + 0.13$$

$$f_p = (18 + 152\tau_{700})^{-1}$$

$$f = \left(-0.337{\tau_{700}}^2 + 0.63\tau_{700} + 0.116 + f_p \ln {}^{p}/_{p_{sl}}\right)^{-1}$$

$$tf_0 = \begin{cases} 0.0057w + 2.94, & \tau_{700} \geq 0.05 \\ 0.0042w + 3.12, & \tau_{700} < 0.05 \end{cases}$$

$$tf_1 = \begin{cases} 0.0554w - 5.71, & \tau_{700} \geq 0.05 \\ 0.092w - 8.86, & \tau_{700} < 0.05 \end{cases}$$

$$tf_2 = \begin{cases} -0.134w + 15.5, & \tau_{700} \geq 0.05 \\ -0.23w + 74.8, & \tau_{700} < 0.05 \end{cases}$$

$$tf_3 = \begin{cases} 0.27w - 20.7, & \tau_{700} \geq 0.05 \\ -3.11w + 79.4, & \tau_{700} < 0.05 \end{cases}$$

$$tf_4 = \begin{cases} -0.21w + 11.6, & \tau_{700} \geq 0.05 \\ 86w - 13800, & \tau_{700} < 0.05 \end{cases}$$

$$tf_p = \begin{cases} -0.71(1 + \tau_{700})^{-15}, & \tau_{700} \geq 0.05 \\ -0.83(1 + \tau_{700})^{-17.2}, & \tau_{700} < 0.05 \end{cases}$$

$$s = -0.0147 \ln w - 0.3079{\tau_{700}}^2 + 0.2846\tau_{700} + 0.3798$$

$$ts_0 = 0.27 + 0.043 \ln w + 0.009 \ln^2 w$$

$$ts_1 = 1.24 + 0.047 \ln w + 0.0061 \ln^2 w$$

$$ts_p = 0.0079w + 0.1$$

$$T_{R_1} = \frac{1 + 1.8169m_R' - 0.033454{m_R}'^2}{1 + 2.063m_R' + 0.31978{m_R}'^2}$$

$$T_{R_2} = \frac{1 - 0.010394m_R'}{1 - 0.00011042{m_R}'^2}$$

$$T_{UM_1} = \frac{1 + 0.95885m_R' + 0.012871{m_R}'^2}{1 + 0.96321m_R' + 0.015455{m_R}'^2}$$

$$T_{UM_2} = \frac{1 + 0.27284m_R' - 0.00063699{m_R}'^2}{1 + 0.30306m_R'}$$

$$T_{O_1} = \frac{1 + f_1 m_O + f_2 {m_O}^2}{1 + f_3 m_O}$$

$$T_{O_2} = 1$$

$$T_{N_1} = \min\left(1, \frac{1 + g_1 m_w + g_2 {m_w}^2}{1 + g_3 m_w}\right)$$

$$T_{N_2} = 1$$

$$T'_{N_1} = \min\left(1, \frac{1 + 1.66g_1 + 2.7556g_2}{1 + 1.66g_3}\right)$$

$$T'_{N_2} = 1$$

$$T_{w_1} = \frac{1 + h_1 m_w}{1 + h_2 m_w}$$

$$T_{w_2} = \frac{1 + c_1 m_w + c_2 {m_w}^2}{1 + c_3 m_w + c_4 {m_w}^2}$$

$$T'_{w_1} = \frac{1 + 1.66h_1}{1 + 1.66h_2}$$

$$T'_{w_2} = \frac{1 + 1.66c_1 + 2.7556c_2}{1 + 1.66c_3 + 2.7556c_4}$$

$$T_{A_1} = \exp\left(m_A \tau_{A_1}\right)$$

$$T_{A_2} = \exp\left(m_A \tau_{A_2}\right)$$

$$T_{AS_1} = \exp\left(m_A \omega_{0_1} \tau_{A_1}\right)$$

$$T_{AS_2} = \exp\left(m_A \omega_{0_2} \tau_{A_2}\right)$$

$$B_{R_1} = 0.5\left(0.89013 - 0.0049558m_R + 0.000045721{m_R}^2\right)$$

$$B_{R_2} = 0.5$$

$$B_a = 1 - \exp(-0.6931 - 1.8326\cos z_0)$$

$$F_1 = \frac{p_0 + p_1 \tau_{A_1}}{1 + p_2 \tau_{A_1}}$$

$$F_2 = \frac{q_0 + q_1 \tau_{A_2}}{1 + q_2 \tau_{A_2}}$$

$$\rho_{s_1} = \frac{0.13363 + 0.00077358\alpha_1 + \beta_1\left(\frac{0.37567 + 0.22946\alpha_1}{1 - 0.10832\alpha_1}\right)}{1 + \beta_1\left(\frac{0.84057 + 0.68683\alpha_1}{1 - 0.08158\alpha_1}\right)}$$

$$\rho_{s_2} = \frac{0.010191 + 0.00085547\alpha_2 + \beta_2\left(\frac{0.14618 + 0.062758\alpha_2}{1 - 0.19402\alpha_2}\right)}{1 + \beta_2\left(\frac{0.58101 + 0.17426\alpha_2}{1 - 0.17586\alpha_2}\right)}$$

$$m_R{}' = \left({}^{p}/_{p_{sl}}\right)\left(\cos z_0 + \frac{0.48353{z_0}^{0.095846}}{(96.741 - z_0)^{1.754}}\right)^{-1}$$

$$m_O = \left(\cos z_0 + \frac{1.0651{z_0}^{0.6379}}{(101.8 - z_0)^{2.2694}}\right)^{-1}$$

$$m_w = \left(\cos z_0 + \frac{0.10648{z_0}^{0.11423}}{(93.781 - z_0)^{1.9203}}\right)^{-1}$$

$$m_A = \left(\cos z_0 + \frac{0.16851{z_0}^{0.18198}}{(95.318 - z_0)^{1.9542}}\right)^{-1}$$

$$\tau_{A_1} = \beta_1{\lambda_{e_1}}^{-\alpha_1}$$

$$\tau_{A_1} = \beta_2{\lambda_{e_2}}^{-\alpha_2}$$

$$\lambda_{e_1} = \frac{d_0 + d_1u_a + d_2{u_a}^2}{1 + d_3{u_a}^2}$$

$$\lambda_{e_2} = \frac{e_0 + e_1u_a + e_2{u_a}^2}{1 + e_3u_a}$$

$$c_1 = \frac{w(19.566 - 1.6506w + 1.0672w^2)}{1 + 5.4248w + 1.6005w^2}$$

$$c_2 = \frac{w(0.50158 - 0.14732w + 0.047584w^2)}{1 + 1.811w + 1.0699w^2}$$

$$c_3 = \frac{w(21.286 - 0.39232w + 1.2692w^2)}{1 + 4.8318w + 1.412w^2}$$

$$c_4 = \frac{w(0.70992 - 0.23155w + 0.096514w^2)}{1 + 0.44907w + 0.75425w^2}$$

$$d_0 = 057664 - 0.024743\alpha_1$$

$$d_1 = \frac{0.093942 - 0.2269\alpha_1 + 0.12848{\alpha_1}^2}{1 + 0.6418\alpha_1}$$

$$d_2 = \frac{-0.093819 + 0.36668\alpha_1 - 0.12775{\alpha_1}^2}{1 - 0.11651\alpha_1}$$

$$d_3 = \frac{\alpha_1\left(0.15232 - 0.087214\alpha_1 + 0.012664{\alpha_1}^2\right)}{1 - 0.90454\alpha_1 + 0.26167{\alpha_1}^2}$$

$$e_0 = \frac{1.183 - 0.022989\alpha_2 + 0.020829{\alpha_2}^2}{1 + 0.11133\alpha_2}$$

$$e_1 = \frac{-0.50003 - 0.18329\alpha_2 + 0.23835{\alpha_2}^2}{1 + 1.6756\alpha_2}$$

$$e_2 = \frac{-0.50001 + 1.1414\alpha_2 + 0.0083589{\alpha_2}^2}{1 + 11.168\alpha_2}$$

$$e_3 = \frac{-0.70003 - 0.73587\alpha_2 + 0.51509{\alpha_2}^2}{1 + 4.7665\alpha_2}$$

$$f_1 = \frac{O_3(10.979 - 8.5421O_3)}{1 + 2.0115O_3 + 40.189{O_3}^2}$$

$$f_2 = \frac{O_3(-0.027589 - 0.005138O_3)}{1 - 2.4857O_3 + 13.942{O_3}^2}$$

$$f_3 = \frac{O_3(10.995 - 5.5001O_3)}{1 + 1.6784O_3 + 42.406{O_3}^2}$$

$$g_1 = \frac{0.17499 + 41.654NO_2 - 2146.4{NO_2}^2}{1 + 22295.0{NO_2}^2}$$

$$g_2 = \frac{NO_2(-1.2134 + 59.324NO_2)}{1 + 8847.8{NO_2}^2}$$

$$g_3 = \frac{0.17499 + 61.658NO_2 + 9196.4{NO_2}^2}{1 + 74109.0{NO_2}^2}$$

$$h_1 = \frac{w(0.065445 + 0.00029901w)}{1 + 1.2728w}$$

$$h_2 = \frac{w(0.065687 + 0.0013218w)}{1 + 1.2008w}$$

$$p_0 = \frac{3.715 + 0.368m_A + 0.036294{m_A}^2}{1 + 0.0009291{m_A}^2}$$

$$p_1 = \frac{-0.164 - 0.72567m_A + 0.20701{m_A}^2}{1 + 0.0019012{m_A}^2}$$

$$p_2 = \frac{-0.052288 + 0.31902m_A + 0.17871{m_A}^2}{1 + 0.0069592{m_A}^2}$$

$$q_0 = \frac{3.4352 + 0.65267m_A + 0.00034328{m_A}^2}{1 + 0.034388{m_A}^{1.5}}$$

$$q_1 = \frac{1.231 - 1.63853m_A + 0.20667{m_A}^2}{1 + 0.1451{m_A}^{1.5}}$$

$$q_2 = \frac{0.8889 - 0.55063m_A + 0.50152{m_A}^2}{1 + 0.14865{m_A}^{1.5}}$$

$$u_a = \ln(1 + \beta m_A)$$

DF14

$$T_R = \exp(-0.103{m'}^{0.571})$$

$$T_w = \exp(-0.081w^{0.213}m^{0.213})$$

$$T_A = \exp(-{\tau_A}^{0.91}m^{0.87})$$

$$T_{DIF} = 0.143 + 0.113\sin h_0 - 0.0485w + \tau_A$$

$$\tau_A = 0.744\tau_{500}$$